MICROSTRUCTURE EVOLUTION AND MECHANICAL RESPONSE OF MATERIAL

BY FRICTION STIR PROCESSING AND MODELING

Sanya Gupta, B.Tech.

Dissertation Prepared for the Degree of

DOCTOR OF PHILOSOPHY

UNIVERSITY OF NORTH TEXAS

August 2022

APPROVED:

Rajiv S. Mishra, Committee Chair
Kevin J. Doherty, Committee Member
Rajarshi Banerjee, Committee Member
Sundeep Mukherjee, Committee Member
Jincheng Du, Committee Member
Vijay Vasudevan, Chair of the Department of
    Materials Science and Engineering
Shengli Fu, Interim Dean of the College of
    Engineering
Victor Prybutok, Dean of the Toulouse Graduate
    School

Gupta, Sanya. *Microstructure Evolution and Mechanical Response of Material by Friction Stir Processing and Modeling*. Doctor of Philosophy (Material Science and Engineering), August 2022, 104 pp., 17 tables, 36 figures, numbered chapter references.

In this study, we have investigated the relationship between the process-microstructure to predict and modify the material's properties. Understanding these relationships allows the identification and correction of processing deficiencies when the desired properties are not achieved, depending on the microstructure. Hence, the co-relation between process-microstructure-properties helped reduce the number of experiments, materials & tool costs and saved much time. In the case of high entropy alloys, friction stir welding (FSW) causes improved strength due to the formation of fine grain structure and phase transformation from f.c.c to h.c.p. The phase transformation is temperature sensitive and is studied with the help of differential scanning calorimetry (DSC) to calculate the enthalpy experimentally to obtain $\Delta G\gamma{\rightarrow}\varepsilon$. The second process discussed is heat treatment causing precipitation evolution. Fundamental investigations aided in understanding the influence of strengthening precipitates on mechanical properties due to the aging kinetics – solid solution and variable artificial aging temperature and time. Finally, in the third case, the effect of FSW parameters causes the thermal profile to be generated, which significantly influences the final microstructure and weld properties. Therefore, a computational model using COMSOL Multiphysics and TC-Prisma is developed to generate the thermal profile for different weld parameters to understand its effect on the microstructure, which would eventually affect and predict the final properties of the weld. The model's validation is done via DSC, TEM, and mechanical testing.

ACKNOWLEDGMENTS

I want to express my heartfelt gratitude to Prof. Rajiv S. Mishra for allowing me to work with him and guiding me throughout my Ph.D. In addition, I am greatly indebted to him for the freedom that I have received in researching various topics of my interest.

I want to extend my sincere gratitude to Dr. Kevin J Doherty for his invaluable support and suggestions. I would also like to thank the Center of Friction Stir Processing (CFSP) and The Army Research Lab (ARL) for funding support for most of my Ph.D.

Thanks to my committee members, Dr. Rajarshi Banerjee, Dr. Sundeep Mukherjee, and Dr. Jincheng Du, for their valuable comments and suggestions in improving the quality of my dissertation for their agreeing to serve on my Ph.D. committee.

I would also like to thank all the CART employees for their help learning instruments and assistance when needed. Finally, I would like to acknowledge the MTSE and UNT staff for their support. I would also like to thank all my lab mates for their assistance in learning various equipment and tools.

I would like to thank all my friends for their everlasting and loving support, without which I would not have come so far in my life. And last but not least, I am immensely thankful to my parents and my brother & sister for their constant support, love, and encouragement in all my endeavors. I am always grateful for the precious life values and accomplishment they taught me.

TABLE OF CONTENTS

LIST OF TABLES

LIST OF FIGURES

x

CHAPTER 1

INTRODUCTION

1.1   Motivation and Objectives

1.1.1   Motivation

FSW has emerged as a revolutionary joining process in the past three decades. Compared to other thermomechanical processes, FSW is a relatively recent process and has not been fully explored. Nevertheless, its various advantages have already replaced conventional welding in the industry for Al and HEA alloys. However, much of the friction stir process relies on empirical knowledge and prior expertise to produce a defect-free weld with desired microstructure and strength, fatigue, creep, and corrosion resistance properties [1]. To obtain a good combination of final properties of the weld, prior knowledge of the effect of the various process control variables like rotational speed, welding speed/traverse speed, tool geometry, material properties, and a backing plate and ambient conditions are needed [2,3]. These process control variables result in the process response variables of peak temperature. Midling and Grong et al. [4] suggested that the thermal cycle experienced by the heat and material flow model results were used for HAZ sub-grain prediction and associate change in strength after welding. Many such attempts were made following this, but not all were complete process integration models. In addition, there are multiple literatures [5–11] on thermal and flow models of the process of FSW both through analytical and numerical means. While some were fully coupled thermo-mechanical models, others have just studied the effect of heat.

The prime task is to produce a defect-free weld and optimize the final properties with a minimum number of trails. This would thus mean a detailed microstructural characterization of each weld; however, this is both an experiment and a time-intensive process. Given the present-

day advent of well-established modeling tools of thermodynamic, kinetic, and strengthening theories, the relation of the thermal model to weld microstructure and strength is deemed possible. Inspired by the availability of inadequate process-microstructure-property relationship models of AA 7017 and Cu-HEA alloy, the current topic is undertaken.

1.1.2 Objective

This work thus seeks to understand and develop processes (FSW & heat treatment) and microstructure to predict properties through careful experiments and modeling.

The broad objectives are:

1. Enable a science-driven approach and provide a greater understanding of the FSW process and the parameters affecting the microstructure and property

2. Increase productivity and faster process development.

3. Process and performance optimization by using an analytical and computational methodology.

1.2 Layout of the Dissertation

The principal objective of this work is to elucidate the effect of friction stir welding (FSW) and processing on microstructural evolution and mechanical response on HEAs and Al alloys. In this study, we seek to understand the thermal effects of the process of FSW on the weld microstructure and final weld properties through a series of careful experiments and modeling. The first alloy system is a new class of material known as complex, concentrated alloys, particularly high entropy alloys, $Fe_{38.5}Cr_{20}Mn_{20}Co_{15}Si_5Cu_{1.5}$ (Cu-HEA), the second is a simple and conventional Al-Cu-Li (2195 Al) alloy, and the final system is Al-Zn-Mg (7017 Al) alloy.

Chapter 2 introduces the background and current research on the three alloy systems in separate sections. The first section presents Cu-HEAs, followed by 2195 Al and 7017 Al alloys. The scope and possible contribution of this study are presented at the end of each section.

Chapter 3 discusses the different zones of friction stir welded γ-fcc dominated metastable high entropy alloy, consisting of mechanical testing, microstructural characterization, and differential scanning calorimetry (DSC). The aim was to understand the different weld zones' metastability and transformation-induced plasticity (TRIP) effect due to thermal and strain cycles during welding. Exciting results were observed as the conventionally weaker heat-affected zone (HAZ) was absent, i.e., the HAZ had higher strength and ductility than the base metal. Furthermore, the stirred region exhibited high strength due to a higher initial γ-fcc phase fraction and refined equiaxed microstructure. In addition, DSC was introduced as a tool to understand metastability and TRIP effect of the different weld zones via enthalpy calculations.

Chapter 4 core objectives were two-fold: a) building a relationship model between the aging time and temperature to obtain the highest strength possible using post-weld + formed heat treatment, and b) fundamental investigations to validate the influence of strengthening precipitates on mechanical properties due to the aging kinetics. The experiments involved heat treatments for two different temperatures and hold time to evaluate the microstructural evolution of the strengthening phase to achieve maximum strength. Based on the precipitation kinetics and aging kinetics, a relationship between the UTS due to the formation of the T_1 phase and aging duration was established, which is in good agreement with the experimental data. Differential scanning calorimetry (DSC) was used to determine the formation and dissolution of the precipitates, and the details were substantiated via transmission electron microscopy (TEM) and related to mechanical properties.

Chapter 5 mainly focuses on the influence of welding parameters on the weld quality using a systematic approach spanning microscopic to macroscopic length scales. Welding parameters impact the mechanical and corrosion resistance behavior due to dissolution, reprecipitation,

growth, and coarsening of precipitates validated by extensive differential scanning calorimetry (DSC) and transmission electron microscopy (TEM). A guideline in selecting parameters for friction stir welding of age hardenable high strength Al alloys to control the width of heat affected zone

Chapter 6 introduces a model for correlating the process-microstructure results to predict the properties of the friction stir welded AA 7017 alloy. This chapter highlights the effect of different process parameters. It also focuses on developing a predictive model of the precipitate distribution in nugget for two different welding parameters and their effect post-weld heat treatment.

Chapter 7 summarizes the current dissertation and puts out the possibilities that can be pursued to improve and build a predictive model for friction stir welding.

1.3   References

[1]   Y. Ma, X. Zhou, Y. Liao, Y. Yi, H. Wu, Z. Wang, W. Huang, Localised corrosion in AA 2099-T83 aluminium-lithium alloy: The role of grain orientation, Corros. Sci. 107 (2016) 41–48.

[2]   R.S. Mishra, Z.Y. Ma, Friction stir welding and processing, Mater. Sci. Eng. R Reports. 50 (2005) 1–78.

[3]   M.W. Mahoney, C.G. Rhodes, J.G. Flintoff, R.A. Spurling, W.H. Bingel, Properties of friction-stir-welded 7075 T651 aluminum, Metall. Mater. Trans. A 1998 297. 29 (1998) 1955–1964.

[4]   O.T. Midling, Grong, A process model for friction welding of AlMgSi alloys and AlSiC metal matrix composites—II. HAZ microstructure and strength evolution, Acta Metall. Mater. 42 (1994) 1611–1622.

[5]   S.C. Wang, Z. Zhu, M.J. Starink, Estimation of dislocation densities in cold rolled Al-Mg-Cu-Mn alloys by combination of yield strength data, EBSD and strength models, J. Microsc. 217 (2005) 174–178.

[6]   H.R. Shercliff, M.F. Ashby, A process model for age hardening of aluminium alloys—II. Applications of the model, Acta Metall. Mater. 38 (1990) 1803–1812. https://doi.org/10.1016/0956-7151(90)90292-O.

[7]   J.D. Robson, N. Kamp, A. Sullivan, Microstructural Modelling for Friction Stir Welding of Aluminium Alloys, Mater. Manuf. Process. 22 (2007) 450–456.

[8]   N. Kamp, A.P. Reynolds, J.D. Robson, Modelling of 7050 aluminium alloy friction stir welding, Sci. Technol. Weld. Join. 14 (2013) 589–596.

[9]   N. Kamp, A. Sullivan, R. Tomasi, J.D. Robson, Modelling of heterogeneous precipitate distribution evolution during friction stir welding process, Acta Mater. 54 (2006) 2003–2014.

[10]   A. Deschamps, Y. Brechet, Influence of predeformation and agEing of an Al–Zn–Mg alloy—II. Modeling of precipitation kinetics and yield stress, Acta Mater. 47 (1998) 293–305.

[11]   A.P. Reynolds, W. Tang, Z. Khandkar, J.A. Khan, K. Lindner, Relationships between weld parameters, hardness distribution and temperature history in alloy 7050 friction stir welds, Sci. Technol. Weld. Join. 10 (2013) 190–199.

CHAPTER 2

BACKGROUND AND LITERATURE SURVEY

2.1   Introduction

Both background information and current literature are presented in this chapter. First, high entropy alloys (HEA) are presented, which is followed by precipitation strengthened aluminum (Al) alloys along with a brief introduction to friction stir welding (FSW) and post-weld heat treatments (PWHT).

2.2   High Entropy Alloys

High entropy alloys are generally defined as a single-phase solid solution composed of five or more principal alloying elements in almost equimolar quantities (between 5% to 35% at. fraction) [1–4]. HEAs provide excellent opportunities to create unique microstructures using appropriate composition and thermomechanical treatments. Li et al. [5] introduced the concept of metastability to HEAs. They reported the first metastable HEA termed dual-phase HEA (DP-HEA) having a composition of Fe50Mn30Co10Cr10, followed by minor addition of carbon in DP-HEA to incorporate the effect of precipitation strengthening along with classical transformation-induced plasticity (TRIP) [6]. Adding the TRIP mechanism to HEAs extended the extent of the deformation mechanism in HEAs, which overcomes the conventional strength-ductility tradeoff and provides exceptional mechanical properties [7,8]. This thesis works on the design of metastable HEAs by adding Cu in FeMnCoCrSi matrix-forming Cu-HEA (Fe38.5Mn20Co20Cr15Si5Cu1.5) impacts not only the high strength-ductility combination but also increases yield strength, fatigue limit, and corrosion resistance [9]. Adding Cu, i.e., γ-f.c.c phase stabilizers, increases dislocation storage ability before it transforms to ε-h.c.p phase under stress. An increase in deformation storage ability

is linked with delaying the formation of stable intrinsic stacking fault in the γ-h.c.p phase, which later acts as the site for the ε phase nucleation.

An alloy design approach is defined as chemistry-driven metastability. In Cu-HEA, the γ-f.c.c phase transforms to the ε-h.c.p. phase upon deformation, and the stability of γ-f.c.c can be tuned through alloy chemistry. Coupling the alloy design with friction stir welding, an innovative high-temperature severe plastic deformation technique, opened up microstructural engineering pathways. The changing fraction of γ-f.c.c and ε-h.c.p phases in the starting microstructure based on welding parameters is defined as processing induced metastability [10]. The change in grain size due to deformation induced by FSW also impacts the metastability, allowing us to understand the volume change during the γ-f.c.c phase to ε-h.c.p phase transformation.

2.3   Precipitation Strengthened Aluminum Alloys

The 2XXX and 7XXX alloys form the class of precipitation strengthened Al alloys. Precipitation strengthened alloys derive their strength from the dispersion formation of fine particles, which act as obstacles to moving dislocations during deformation [11,12]. It is the most widely used method to improve strength in aluminum alloys. The primary criteria for an alloy to be classified as the precipitation strengthened alloy is a decrease in solid solubility of alloying elements with a decrease in temperature. It can be explained with the classic example of precipitation in the Al-Cu system, as shown in Figure 2.1. The thermal treatment required in this process starts with solution heat treatment by soaking the alloy at a sufficiently high temperature for long enough to form a solid solution (step 1 in Figure 2.1). It is followed by rapid quenching to room temperature to form a supersaturated solid solution (step 2 in Figure 2.1). Precipitation of secondary phases occurs at room temperature (natural aging) or elevated temperature (artificial aging, step 3 in Figure 2.1) due to the decrease in solid solubility of alloying elements at lower

temperatures. Artificial aging can be a single or multi-step thermal treatment depending upon alloy chemistry and targeted property.
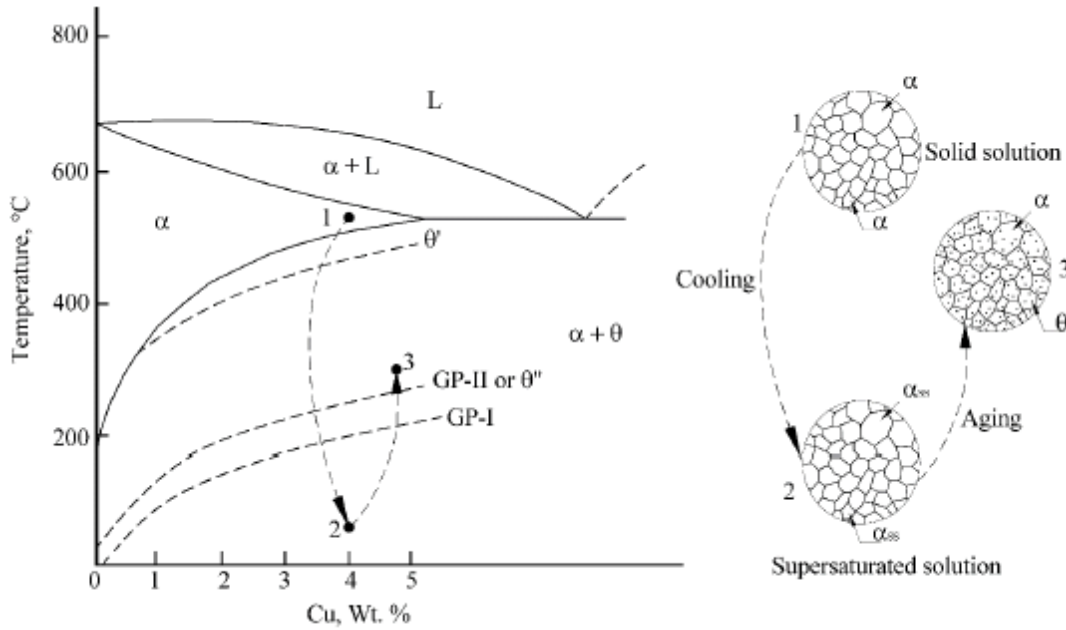
Figure 2.1: Al-rich binary phase diagram of the Al-Cu system with a schematic illustrates the steps involved in the aging treatment of precipitation-strengthened aluminum alloys [13].

2XXX series is Al-Cu-Li alloys containing all the Al-Cu and Al-Li systems phases, i.e., θ', θ (Al_2Cu), and δ' (Al_3Li). T_1 (hexagonal, Al_2CuLi) is also observed and is the primary strengthening precipitate along with θ and δ' in the Al-Cu-Li system. T_1 forms as thin and long plate type precipitate on the {111} matrix planes [14–16].

7XXX alloys are Al-Zn-Mg system-based aluminum alloys. Both Mg and Zn, the main alloying elements of 7XXX, have high solubility in aluminum at higher temperatures. After quenching from high temperatures, Mg and Zn clusters form the GP zones [17]. 7XXX alloys gain strength from the phase precipitation of the metastable coherent η' ($MgZn2$). GP zones act as the precursor to the η' phase. η' phase transforms into a stable but incoherent η phase. The precipitation sequence observed in 7XXX alloys is [17]:

$$\alpha_{supersaturated\ solid\ solution} \rightarrow GP\ Zones \rightarrow \eta' \rightarrow \eta$$

8
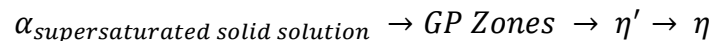
2.4   Friction Stir Welding

The invention of Friction Stir Welding (FSW) by The Welding Institute in 1991 ushered in a new era in the joining technology in general and joining of aluminum alloys in particular [18]. In this process, a non-consumable rotating tool, made of material stronger than the workpiece, with a larger diameter shoulder and a pin, plunges into the workpiece to a pre-programmed depth. Plunging the rotating tool into the workpiece produces frictional heat due to the interaction between the tool shoulder and the workpiece. Another contribution to the temperature comes from the adiabatic heat produced during plastic deformation at a high strain rate of workpiece material around the rotating tool pin. Plastic deformation at high temperatures leads to the softening of material around the pin. The softened material moves around with the rotation of the tool pin, which then traverses along a joint line and completes the weld. The larger diameter of the tool shoulder helps contain the hot material that can otherwise flow outward to form flash and may lead to loss of material and defective weld. The schematic shown in Figure 2.2 illustrates the process for welding a workpiece in a butt configuration.

During FSW, a solid-state joining process, melting does not take place. Thus, this process benefits and diminishes the possibility of common defects like segregation, dendritic structure, hot cracking, and porosity formation associated with fusion-based welding techniques [19–21]. Recently, FSW has been used in some applications in the aerospace and automobile industries for structural applications [21]. FSW is also a green process as the energy consumption is usually between 2-5% of energy consumption in laser-based welding [19]. Another benefit of this process is that the tool is non-consumable, and thus the requirement of filler material is completely avoided.

FSW results in an asymmetric weld cross-section. The side where the tangential velocity

of the tool is along the welding direction is called the advancing side (AS). The other side, where

the tangential velocity of the tool is opposite to the welding direction, is called the retreating side

(RS). FSW of an aluminum alloy results in three different microstructural zones, shown in Figure

2.2 and explained below.
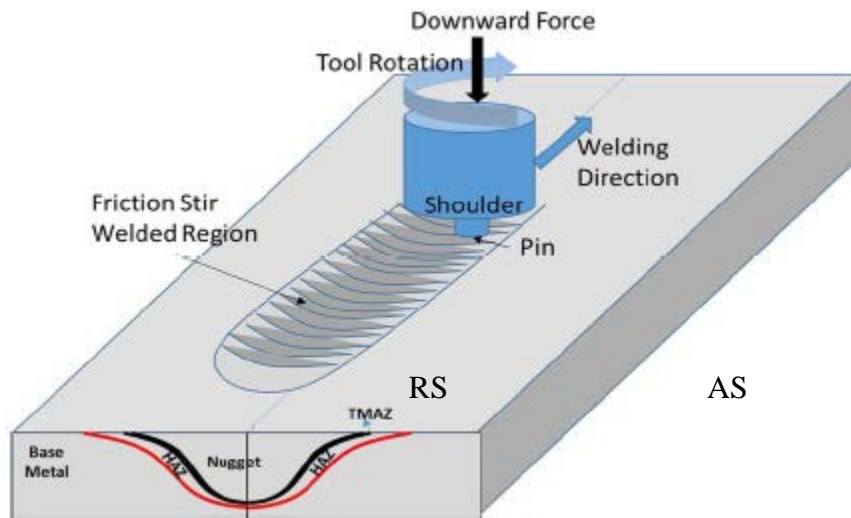
Figure 2.2: Schematic of friction stir welding process [22]

- *Weld nugget (WN)*: Plastic deformation and frictional heat generated during FSW

transform parent material into equiaxed fine-grained recrystallized microstructure in the weld

nugget. Grain size in nugget usually ranges from 2-15 μm depending on FSW parameters, tool

geometry, material composition, and external cooling [22]. In aluminum alloys, the weld nugget

experiences a peak temperature of 400-550 ℃ during FSW [22]. In precipitation strengthened

aluminum alloys, such high temperatures can lead to coarsening, dissolution, and re-precipitation

of precipitates depending on the thermal stability of precipitate, alloy chemistry, external cooling,

and peak temperature in the weld nugget [23].

- *Thermo-mechanically affected zone (TMAZ)*: The zone between the base material and

nugget having experienced both temperature and plastic deformation during FSW is the thermo-

mechanically affected zone (TMAZ) [19,21]. Partial recrystallization is generally observed in

TMAZ. Dissolution of strengthening precipitates might occur in this zone during welding. However, the extent of dissolution varies depending on the thermal cycle and the type of alloy.

- *Heat affected zone (HAZ)*: The zone separating TMAZ and base material is the heat-affected zone (HAZ). This zone does not undergo plastic deformation and only experiences a thermal cycle. For a given set of welding parameters, the formation of the HAZ depends upon the alloy being welded. Generally, HAZ is observed as an area away from the WN that experiences a temperature cycle of 250-350 °C during welding [22]. The HAZ is characterized by the coarsening of strengthening precipitates and the precipitate-free zone (PFZ) formation due to high-temperature exposure[24]. Using an external cooling medium can reduce the extent of the HAZ formation.

2.5   Post Weld Heat Treatments

During a friction stir weld, strength will be lost throughout the weld due to the dissolution of the existing precipitates in the nugget. Coarsening is believed to be the reason the HAZ experiences a drop-in strength. Post-weld heat treatment is typically carried out to form new precipitates in the nugget [23]. During artificial aging (121 °C for 24 hrs.), the diffusion kinetics of the solute accelerates. The nugget contains a large amount of solute and allows re-precipitation to occur. However, the HAZ with less solute available only coarsens the existing precipitates rather than nucleating new GP zones. On the other hand, natural aging allows the formation of GP zones in the HAZ and nugget because diffusion is slow enough to allow nucleation and growth of the GP zones.

2.6   References

[1]   B. Cantor, I.T.H. Chang, P. Knight, A.J.B. Vincent, Microstructural development in equiatomic multicomponent alloys, Mater. Sci. Eng. A. 375–377 (2004) 213–218.

[2]   J.W. Yeh, S.K. Chen, S.J. Lin, J.Y. Gan, T.S. Chin, T.T. Shun, C.H. Tsau, S.Y. Chang, Nanostructured High-Entropy Alloys with Multiple Principal Elements: Novel Alloy Design Concepts and Outcomes, Adv. Eng. Mater. 6 (2004) 299–303.

[3]   X.F. Wang, Y. Zhang, Y. Qiao, G.L. Chen, Novel microstructure and properties of multicomponent CoCrCuFeNiTix alloys, Intermetallics. 15 (2007) 357–362.

[4]   D.B. Miracle, O.N. Senkov, A critical review of high entropy alloys and related concepts, Acta Mater. 122 (2017) 448–511.

[5]   Z. Li, K.G. Pradeep, Y. Deng, D. Raabe, C.C. Tasan, Metastable high-entropy dual-phase alloys overcome the strength–ductility trade-off, Nature. 534 (2016) 227–230.

[6]   Z. Li, C.C. Tasan, H. Springer, B. Gault, D. Raabe, Interstitial atoms enable joint twinning and transformation induced plasticity in strong and ductile high-entropy alloys, Sci. Rep. 7 (2017) 1–7.

[7]   R.S. Mishra, N. Kumar, M. Komarasamy, Lattice strain framework for plastic deformation in complex concentrated alloys including high entropy alloys, Mater. Sci. Technol. 31 (2015) 1259–1263.

[8]   M.A. Hemphill, T. Yuan, G.Y. Wang, J.W. Yeh, C.W. Tsai, A. Chuang, P.K. Liaw, Fatigue behavior of Al0.5CoCrCuFeNi high entropy alloys, Acta Mater. 60 (2012) 5723–5734.

[9]   S.S. Nene, M. Frank, K. Liu, S. Sinha, R.S. Mishra, B.A. McWilliams, K.C. Cho, Corrosion-resistant high entropy alloy with high strength and ductility, Scr. Mater. 166 (2019) 168–172.

[10]   S. Gupta, P. Agrawal, S.S. Nene, R.S. Mishra, Friction stir welding of γ-fcc dominated metastable high entropy alloy: Microstructural evolution and strength, Scr. Mater. 204 (2021) 114161.

[11]   J.W. Martin, Precipitation Hardening: Theory and Applications, (1998).

[12]   R.R.-H. R. Abbaschian, Physical Metallurgy Principles, 2008.

[13]   T. Gladman, Precipitation hardening in metals, Mater. Sci. Technol. 15 (2013) 30–36.

[14]   A.K. Shukla, I.A. Baeslack, Study of process/structure/property relationships in friction stir welded thin sheet Al–Cu–Li alloy, Sci. Technol. Weld. Join. 14 (2013) 376–387.

[15]   A.K. Shukla, W.A. Baeslack, Study of microstructural evolution in friction-stir welded thin-sheet Al–Cu–Li alloy using transmission-electron microscopy, Scr. Mater. 56 (2007) 513–516.

[16]   W.A. Cassada, G.J. Shiflet, E.A. Starke, The effect of plastic deformation on Al2CuLi (T 1) precipitation, Metall. Trans. A. 22 (1991) 299–306.

[17] J. Lendvai, Precipitation and Strengthening in Aluminium Alloys, Mater. Sci. Forum. 217–222 (1996) 43–56.

[18] Wayne M. Thomas, E.D. Nicholas, J.C. Needham, M.G. Murch, P. Temple-Smith, C.J. Dawes, Friction welding, 5,460,317, 1995.

[19] R.S. Mishra, P.S. De, N. Kumar, Friction Stir Processing, Frict. Stir Weld. Process. (2014) 259–296.

[20] R.S. Mishra, M.W. Mahoney, Y. Sato, Y. Hovanski, R. Verma, Friction Stir Welding and Processing VI, 2011.

[21] P.S. De, R.S. Mishra, Friction stir welding of precipitation strengthened aluminium alloys: scope and challenges, Sci. Technol. Adv. Mater. 16 (2013) 343–347.

[22] R.S. Mishra, Z.Y. Ma, Friction stir welding and processing, Mater. Sci. Eng. R Reports. 50 (2005) 1–78.

[23] P.S. De, R.S. Mishra, Friction stir welding of precipitation strengthened aluminium alloys: scope and challenges, Sci. Technol. Weld. Join. 16 (2013) 343–347.

CHAPTER 3

FRICTION STIR WELDING OF GAMMA (F.C.C) DOMINATED METASTABLE HIGH

ENTROPY ALLOY: MICROSTRUCTURAL EVOLUTION AND STRENGTH*

3.1   Abstract

A systematic study was conducted on butt friction stir welding of a recently developed Cu-containing metastable high entropy alloy (HEA). Different weld zones were evaluated using mechanical testing, microstructural characterization, and differential scanning calorimetry (DSC). The nugget exhibited high tensile strength due to the refined equiaxed microstructure. Interestingly, the heat-affected zone, which is known to be the weakest region, exhibited an excellent combination of strength and ductility compared to the base metal. In addition, DSC was explored as a novel and quick technique to obtain enthalpy information and thus understand the TRIP effect.

3.2   Introduction

High entropy alloys are promising structural materials with equiatomic or non-equiatomic compositions because of a good combination of strength and ductility [1–3]. Further improvement in mechanical properties was reported by Li et al. [4] with the introduction of dual-phase HEA (DP-HEA). Since around 2010, HEAs have been studied widely for multifaceted properties such as strength and ductility [5,6], irradiation resistance [7], corrosion resistance [8], and high fracture toughness [9,10]. Apart from the listed properties, weldability, which is a fundamental property determining the usability of structural material, has started getting attention [11–13]. HEAs are

---

designed with the aim to obtain low stacking fault energy (SFE), thus aiding the transformation or twin-induced plasticity (TRIP or TWIP effect) that leads to improved work hardening and thus strength of the material. Recently, Nene et al. [14,15] reported the addition of Si to DP-HEA, thus introducing a new alloy composition, $Fe_{40}Mn_{20}Co_{20}Cr_{15}Si_5$ (CS-HEA), with reduced SFE of ~6.31 mJ/m^2 as reported by Frank et al. [16] via neutron diffraction.

A recent study confirmed that Cu added to CS-HEA, with the help of a novel high-throughput technique - friction stir gradient alloying (FSGA) [17,18], enhanced microstructural evolution and furthered the study of its mechanical properties. The addition of Cu resulted in stabilizing γ (f.c.c) microstructure along with concurrent grain refinement. Furthermore, Cu addition led to a decrease in metastability and delayed the onset of the TRIP effect, thus improved overall work hardening [8,17]. Friction stir processed (FSP) Cu-stabilized CS-HEA ($Fe_{38.5}Mn_{20}Co_{20}Cr_{15}Si_5Cu_{1.5}$, henceforth referred to as Cu-HEA) tested for corrosion resistance [8], and cyclic behavior [19], proved to have superior properties.

Various FSP studies have been based on the principle of friction stir welding (FSW) as a tool for microstructural modification [20–22]. FSW is a promising solid-state joining technique that introduces excellent properties like high ultimate tensile strength (UTS) and joint efficiency. High strength is due to the synergistic action of heat as well as plastic deformation on materials and thus leading to the formation of fine grain size in the nugget (stirred zone) and phase evolution during tensile deformation [23,24]. A study comparing FSW and laser welding (LW) for high entropy alloy CrMnFeCoNi showed grain size refinement by a factor of ~14% compared to the base material (BM) with superior weldability and strength; whereas LW reported fluctuations in the fusion zone [25].

In the present work, the weldability of metastable Cu-HEA γ (f.c.c) dominated alloy is

explored using FSW. A detailed study with respect to strength based on phase transformation in each of the weld zones: nugget, heat affected zone (HAZ), and base material (BM) was carried out via mechanical testing, microstructural characterization, and differential scanning calorimetry (DSC).

3.3   Material and Methods

$Fe_{38.5}Mn_{20}Co_{20}Cr_{15}Si_5Cu_{1.5}$ HEA (Cu-HEA) was prepared by casting in a vacuum induction melting furnace and subsequent rolling. The rolled sheet was homogenized at 900°C for 8 hrs followed by water quenching. For FSW, two rectangular pieces of $(160 \times 75 \times 6)$ mm^3 were cut using electric machine discharge (EDM) from the rolled plate. FSW was carried out in the air on an MTI RM-1 friction stir welding machine with tool rotation rate of 350 revolutions per minute (RPM), welding speed of 50.8 mm/min, plunge depth of 4.4 mm, and tilt angle of -2.5⁰. A W-Re tool was used with 16 mm shoulder diameter, 7.5 mm root diameter, and pin diameter and length of 5 mm and 4 mm, respectively. A Cu backing plate was used for higher heat dissipation. Figure 3.1 (a) shows the macro-image of the butt friction stir welded plates. The cross-section of the weld was cut using EDM and subsequent grinding and polishing were carried out for hardness testing and microstructural characterization. The specimen was prepared to start from 600-grade emery paper polishing followed by final polishing with 0.02 µm colloidal silica to obtain the surface with a mirror finish. Vickers microhardness along the centerline on the cross-section was measured in intervals of 0.5 mm with a load of 0.5 kg and dwell time of 10 seconds. Results from the hardness test of the weld cross-section (Figure 3.1 (b)) helped to identify all the zones observed after FSW (Figure 3.1 (c)). The microstructural studies for each zone were carried out using the FEI NOVA Nano scanning electron microscope (SEM) with electron backscattered diffraction (EBSD) measurements obtained using a Hikari Super EBSD camera. The EBSD data were analyzed using

16

TSL OIM 8 software to get an estimate of grain size and phase fraction of different zones in the microstructure. Microstructural characterization was followed by tensile tests for the identified zones. For the tensile testing, rectangular 1 mm-thick dog bone-shaped mini-tensile specimens were carefully machined using a computer numerical control (CNC) machine from 1 mm below the surface within the nugget, HAZ, and BM as shown in Figure 3.1 (b). Gauge length and width of the tensile specimens were ~5 mm and ~1.25 mm, respectively. The samples were tested at room temperature with an initial strain rate of 10^{-3} s^{-1}. The width identified for thermo-mechanically affected zone (TMAZ) was not big enough to mill a tensile sample. Differential scanning calorimetry (DSC) is traditionally used and reported to measure the melting point, nucleation of new phases, and allotropic transformation. In the current study, DSC is used as a novel approach to understand the metastability of the TRIP HEA by carrying out experiments before and after the deformation. For the DSC study, samples were extracted from the tensile tested samples for undeformed (from the grip) and deformed regions (from the gauge fractured region) for all three zones. A Netzsch 204F1 Phoenix® system was used to perform and analyze the data with a heating rate of 20°C/minute.

3.4   Result and Discussion

Figure 3.1 (b) gives hardness values across the weld cross-section. Hardness values for the nugget region and HAZ were much higher than for the BM, with not much difference in advancing and retreating sides. The average hardness values for the nugget, HAZ and BM are ~235 HV, ~205 HV, and ~195 HV, respectively. The nugget displays higher hardness due to the combination of dynamic recrystallization and work hardening as reported by Nene et al. [8] and explained by micrographs in subsequent sections. However, the improved HAZ properties are due only to microstructural evolution owing to the thermal effect it experienced during FSW.
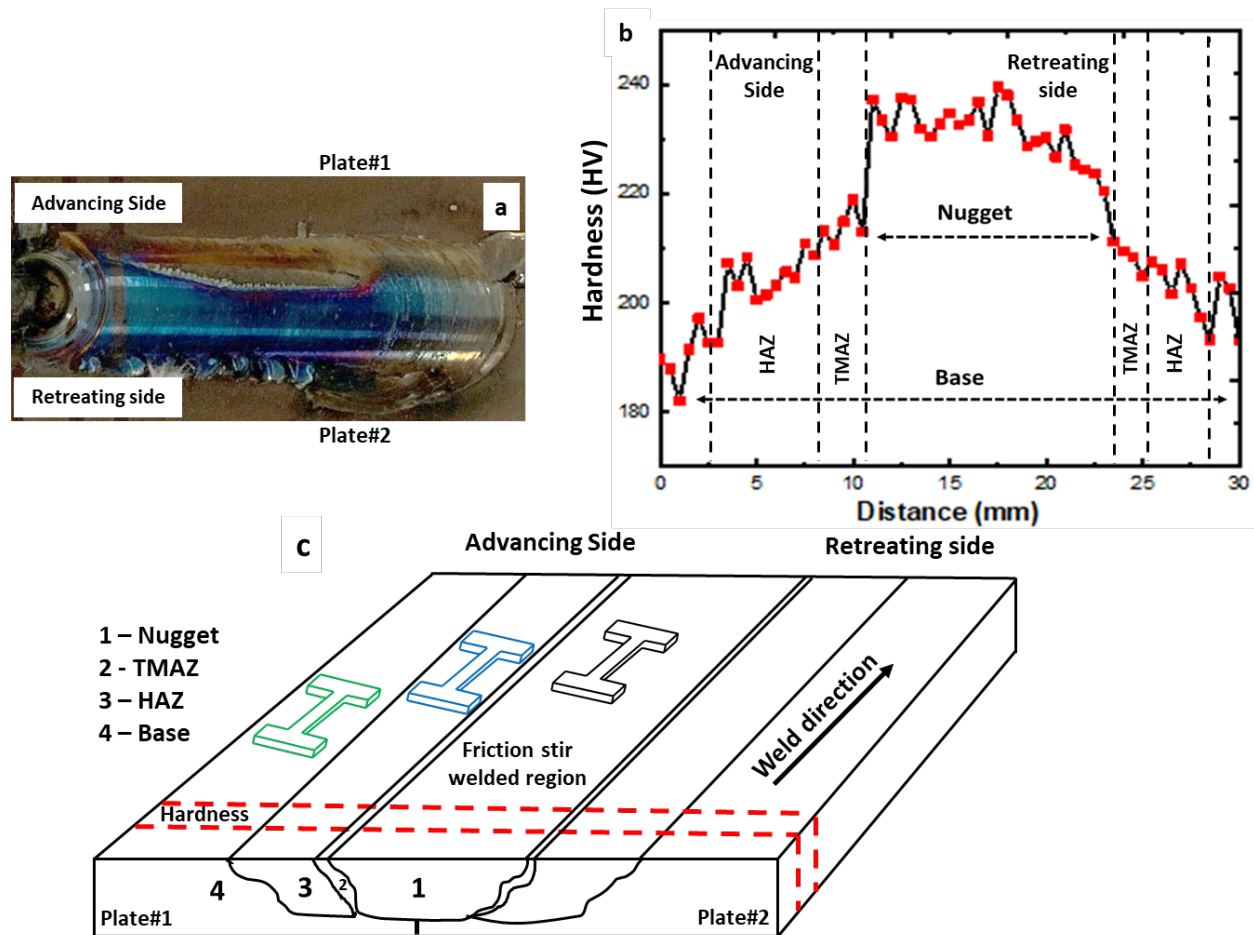
Figure 3.1: (a) Macro-image of welded block via friction stir welding (FSW), (b) hardness profile across the cross-section of FSW run, and (c) schematic of the FSW and locations marked for the tensile samples machined out.

Figure 3.2 (a) captures the phase maps via EBSD measurements of the overall FSW region along with demarcation for all zones nugget, TMAZ, HAZ, and BM. Figure 3.2 (b) shows a change in grain size in the nugget as compared to BM with the change in phase fraction. The BM depicts grain size more than 50 μm with phase distribution of γ (f.c.c) 79% and ε (h.c.p) 21%. Grain refinement (grain size less than 15 μm) in the nugget region (Figure 3.2 (b)) is attributed solely to friction stirring that leads to high temperatures and severe deformation in the stirred zone [26]. The nugget also displayed a change in phase fraction where γ (f.c.c) is 92% and ε (h.c.p) is 8%, making γ (f.c.c) more stable (Figure 3.2 (b)). The increased percentage of γ (f.c.c) in the nugget

18

compared to BM is attributed to temperature and strain [4,18–20]. Higher γ (f.c.c) in nugget can also be attributed to the dissolution of Cu in solid solution, which is observed in the EDS maps as shown in Figure 3.2 (c_1-c_3). The base material had regions of higher and lower Cu concentration. In the nugget, the value of Cu in the analyzed region is close to the nominal value of 1.5%.

Elements	Nugget	Base
Fe	38.49	36.76
Mn	20.42	20.66
Co	20.67	19.90
Cr	14.44	13.98
Si	4.50	5.19
Cu	1.48	3.52
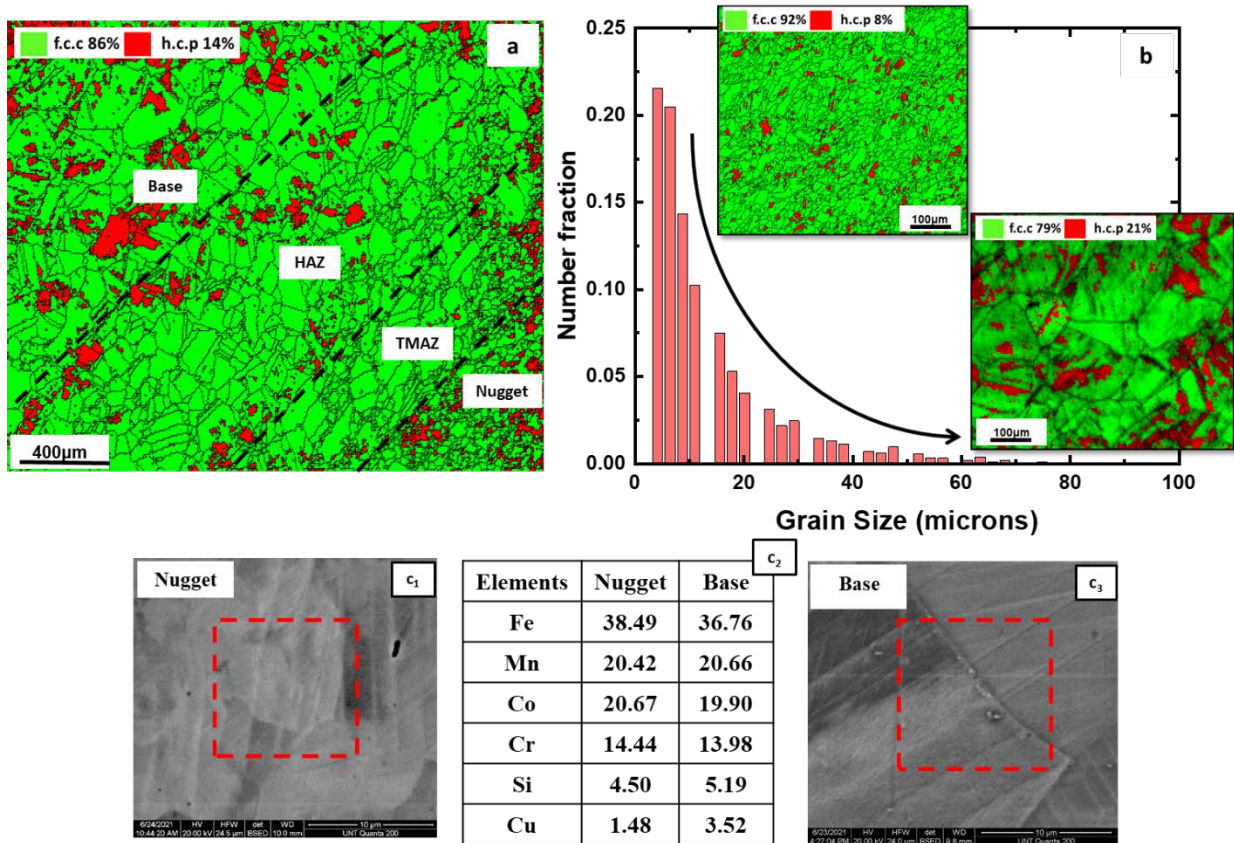
Figure 3.2: EBSD results for overall FSW region. (a) Phase maps where green color is for γ (f.c.c) phase and red is for ε (h.c.p) phase, (b) a plot representing the grain size distribution across the weld along with the phase maps for nugget and BM, and (c_1-c_3) represents the EDS results for nugget and BM

True stress-strain and work hardenability (WH) curves of all three zones are presented in Figure 3.3 (a). This comparison allows discussion of two key aspects. First, does initial phase content have significant effect on subsequent phase transformation? Second, does the grain refinement impact the overall transformation? Compared to the BM, the curves for the nugget (finer grain size and higher starting γ (f.c.c) phase fraction) and the HAZ (higher starting γ (f.c.c)

phase fraction than the BM but with pockets on fine grains) displayed higher YS and UTS. Note that while the YS depends only on the starting microstructure, the reason for the higher UTS in the nugget and specifically in the HAZ can be explained with the help of WH curves [27-29]. The increase in the YS, therefore, can be attributed to the finer overall grain size in the nugget and pocket of finer grains in the HAZ. The hump in the WH curves in Figure 3.3 (a) corresponds to the TWIP/TRIP effect, which shifts to higher stresses and lower strain levels as one travels from BM to HAZ to nugget [12,30]. Tian et al. [31] reported that the TWIP/TRIP is very sensitive to grain size where the onset shifts to lower strain with a decrease in grain size. In this study, as can be noted from Figure 3.3, the change or increase in transformed ε (h.c.p) % was quite similar for all the three zones (% transformation is 62% for nugget, 57% for HAZ and 62% for the BM). It is important to split the overall response into the onset of transformation and total extent of transformation. These two aspects impact the overall stress-strain curve in different ways. So, while the onset of TRIP/TWIP effect in nugget can be argued based on the grain size effect (comparison of Figure 3.3 (a) with (b$_1$) and (b$_2$)), the higher fraction of γ (f.c.c) phase fraction does not add additional uniform ductility as the extend of deformation induced transformation is same as the base material. Comparison of HAZ and BM provides insight on the effect of starting phase fraction with relatively similar grain size. The deformed phase map of BM (Figure 3.3 (d$_2$)) shows a higher activity of slip (or more slip lines) as compared to HAZ (Figure 3.3 (c$_2$)), leading to more transformed ε (h.c.p) % in BM. A study carried out by Sinha et al. [32] in the same alloy shows reversal of ε (h.c.p) to γ (f.c.c) on annealing (heating). The phase reversal leads to finer grains. Figure 3.3 (c2) does show that the retained or non-transformed pockets of γ (f.c.c) phase are very fine. Table 3.3 (e) summarizes the tensile properties for these three regions. The results from microscopy and mechanical testing show that FSW causes Cu-HEA to exhibit microstructural

phase evolution and exhibited a unique variation in grain size that led to a significant increase in strength. This is very encouraging as the entire joint shows properties higher than the BM.
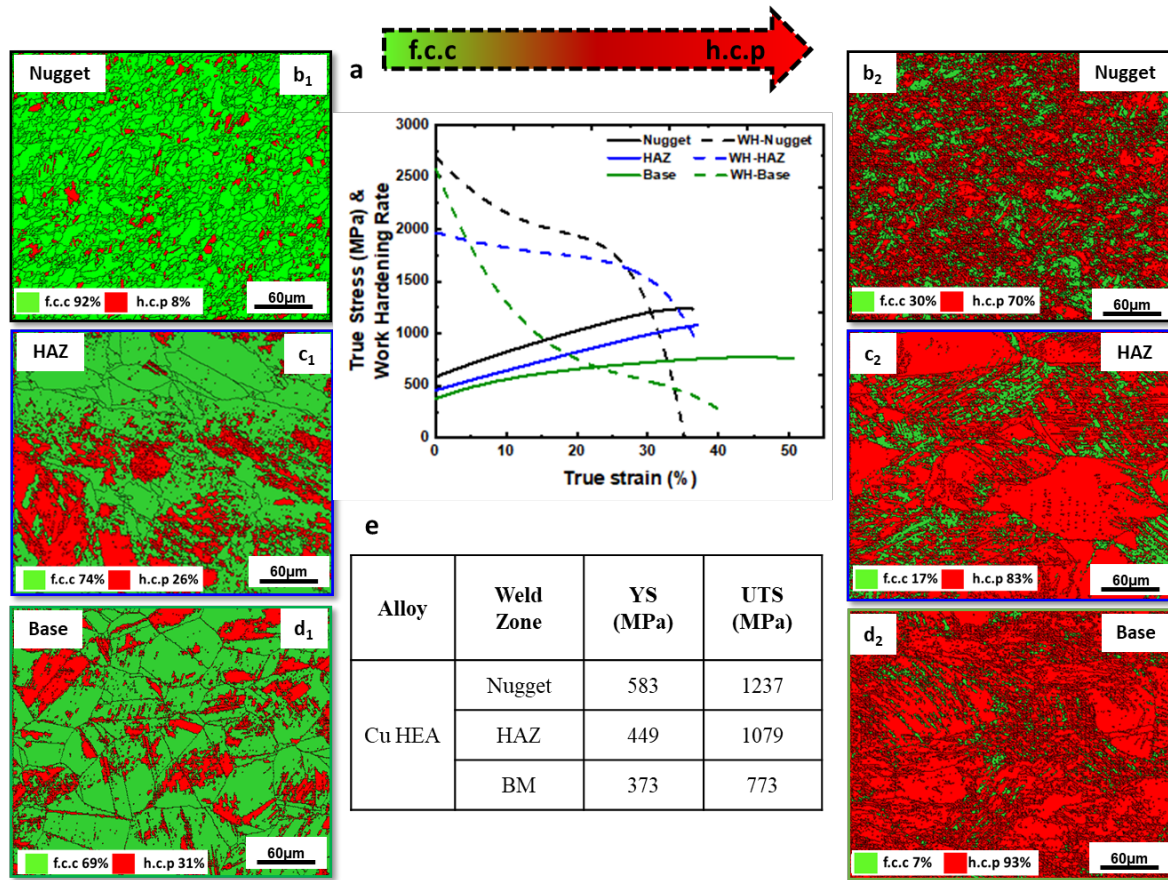
Figure 3.3: (a) True stress-strain curves along with work hardening rates for all the regions; (b1, c1, and d1) are the phase maps for the nugget, HAZ and BM, respectively, before the deformation; and (b2, c2, and d2) are the phase maps for the nugget, HAZ and BM, respectively, after deformation; and (e) tabulated tensile properties for different weld zones.

Further, DSC was carried out in an attempt to understand the metastability of HEAs instead of going through rigorous experiments to calculate the change in enthalpy, ΔH required to obtain $\Delta G^{\gamma \rightarrow \varepsilon}$. Figure 3.4 represents the DSC study of samples undeformed and deformed to understand the phase transformation. The samples are heated to 700°C to cover the transformation temperature with a heating rate of 20°C/min and cooled to room temperature as for 1.5 mole % Cu-HEA concerning phase diagram is the phase transformation range. An endothermic reaction is depicted as a hill (upward curve), while the exothermic reaction is drawn as a valley (downward curve).

The endothermic reactions are followed by phase transformation i.e. γ (f.c.c) to ε (h.c.p). The area under the peaks dictates the change in enthalpy, ΔH. Table 3.4 (b) presents the change in the microstructural phase fraction for undeformed and deformed regions for nugget, HAZ, and BM (from Figure 3.3). The DSC for undeformed and deformed regions are captured in Figure 3.4 (c) and (d), respectively. The solid line in the curve represents the heating and the dotted line as cooling curves. The onset for the endothermic reactions in the heating curve is ~ 400°C which signifies the phase transformation i.e. ε (h.c.p) is transforming to γ (f.c.c) for all the regions, as seen from Figure 3.4 (a). For Figure 3.4 (c), for samples undeformed, the peak is highest for BM and the lowest for nugget. These results when compared with tabulated phase fractions in Figure 3.4 (b), shows that the condition with more ε (h.c.p) leads to higher peak means more energy required for transformation to γ (f.c.c). Table 3.4 (e) shows the experimental change in enthalpy calculations for all zones undeformed (calculated change in enthalpy nugget ~ 1208 kJ/mol, HAZ ~ 1236 kJ/mol and BM ~1274kJ/mol) and deformed regions (calculated change in enthalpy nugget ~664kJ/mol, HAZ ~789kJ/mol and BM ~980kJ/mol), obtained by the area under the curve. The results can be explained by the temperature as the dominate factor when all the zones of weld are compared in order to understand the phase transformation. A similar argument is for independently comparing different zones for deformed samples in Figure 3.4 (d). On comparing undeformed and deformed samples (Figure 3.4 (c) and (d)), the peaks for the deformed region are shorter and broader, hinting at lower energy required for transformation in the deformed regions. The reason for the energy difference for the undeformed region and the deformed can be explained by $\Delta G^{\gamma \rightarrow \varepsilon}$ for $\gamma \rightarrow \varepsilon$ transformation [30]. As for the deformed region, the driving force will increase as the stress factor is more dominant, making γ (f.c.c) more metastable and therefore the transformation to ε (h.c.p) becomes easier in comparison to the undeformed region.
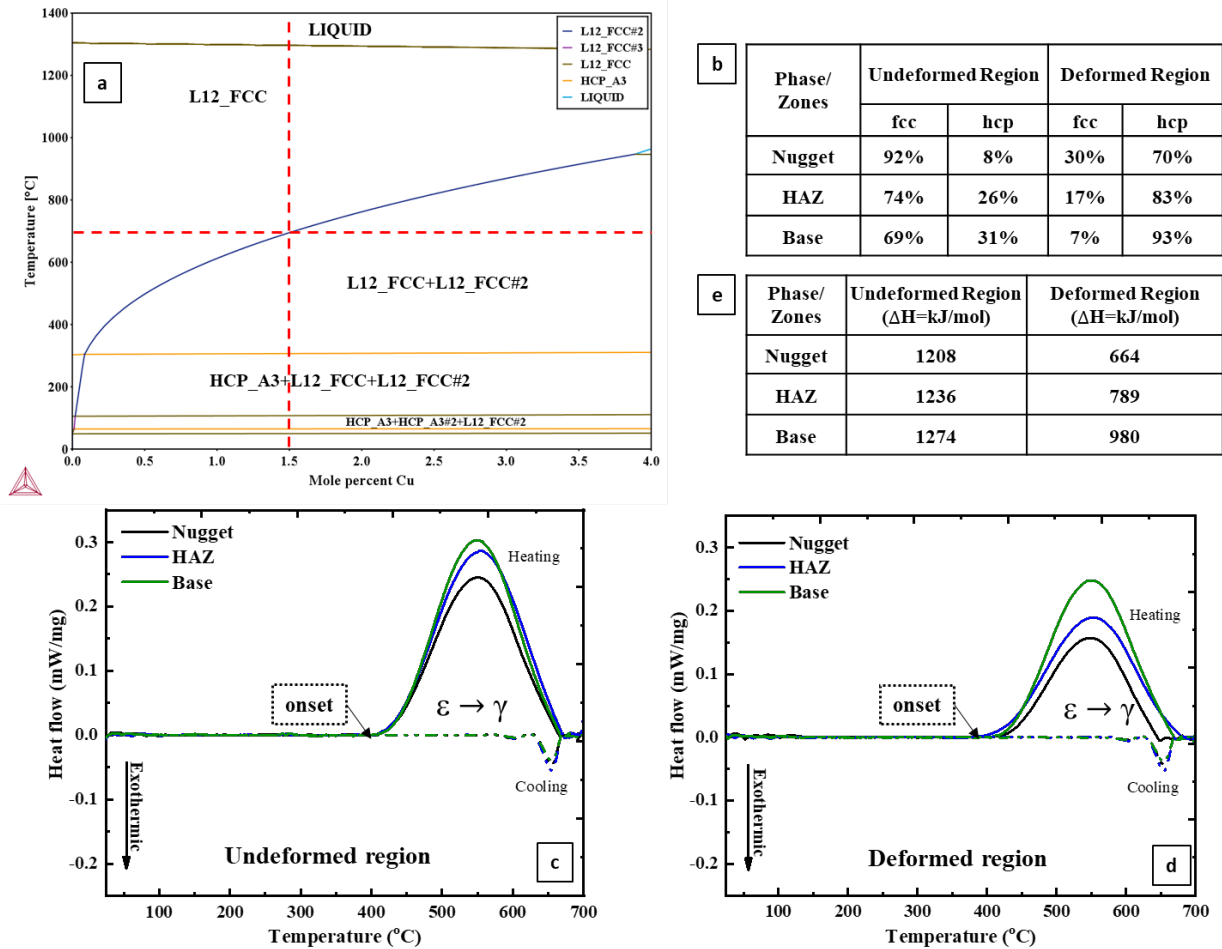
Figure 3.4: DSC study to quantify the energy change associated with deformation. (a) Cu-HEA phase diagram with TCFE9 database, (b) summary of the changes in microstructural phase fraction for undeformed and deformed regions for weld regions, (c) DSC curves for nugget, HAZ and BM for the undeformed region, and (d) DSC curves for nugget, HAZ, and BM for the deformed region, and (e) summary of experimental enthalpy calculated for undeformed and deformed regions.

3.5   Conclusion

Cu-HEA with the dominant γ (f.c.c) phase was studied for weldability via friction stir welding. The alloy exhibited good combination mechanical properties for all the zones, including enhanced properties of the weld region - nugget (i.e., weld region) and the HAZ. DSC has been introduced as a novel and hands-on technique to study the metastability and the TRIP/TWIP effect in HEAs along with the usual transformation temperature quantitatively.

3.6   References

[1]   D.B. Miracle, O.N. Senkov, Acta Mater. 122 (2017) 448–511.

[2]   B. Cantor, Entropy 16 (2014) 4749–4768.

[3]   R.S. Mishra, S.S. Nene, M. Frank, S. Sinha, K. Liu, S. Shukla, J. Alloys Compd. 842 (2020) 155625.

[4]   Z. Li, C.C. Tasan, K.G. Pradeep, D. Raabe, Acta Mater. 131 (2017) 323–335.

[5]   C. Lee, G. Song, M.C. Gao, R. Feng, P. Chen, J. Brechtl, Y. Chen, K. An, W. Guo, J.D. Poplawsky, S. Li, A.T. Samaei, W. Chen, A. Hu, H. Choo, P.K. Liaw, Acta Mater. 160 (2018) 158–172.

[6]   B. Cai, B. Liu, S. Kabra, Y. Wang, K. Yan, P.D. Lee, Y. Liu, Acta Mater. 127 (2017) 471–480.

[7]   N.A.P.K. Kumar, C. Li, K.J. Leonard, H. Bei, S.J. Zinkle, Acta Mater. 113 (2016) 230–244.

[8]   S.S. Nene, M. Frank, K. Liu, S. Sinha, R.S. Mishra, B.A. McWilliams, K.C. Cho, Scr. Mater. 166 (2019) 168–172.

[9]   J.T. Fan, L.J. Zhang, P.F. Yu, M.D. Zhang, D.J. Liu, Z. Zhou, P. Cui, M.Z. Ma, Q. Jing, G. Li, R.P. Liu, Mater. Sci. Eng. A 728 (2018) 30–39.

[10]   F. Otto, A. Dlouhý, C. Somsen, H. Bei, G. Eggeler, E.P. George, Acta Mater. 61 (2013) 5743–5755.

[11]   E.I. Galindo-Nava, P.E.J. Rivera-Díaz-del-Castillo, Acta Mater. 128 (2017) 120–134.

[12]   S. Martin, S. Wolf, U. Martin, L. Krüger, D. Rafaja, Metall. Mater. Trans. A Phys. Metall. Mater. Sci. 47 (2016) 49–58.

[13]   S. Sinha, S.S. Nene, M. Frank, K. Liu, P. Agrawal, R.S. Mishra, Sci. Rep. 9 (2019).

[14]   S.S. Nene, M. Frank, K. Liu, S. Sinha, R.S. Mishra, B. McWilliams, K.C. Cho, Scr. Mater. 154 (2018) 163–167.

[15]   S.S. Nene, M. Frank, P. Agrawal, S. Sinha, K. Liu, S. Shukla, R.S. Mishra, B.A. McWilliams, K.C. Cho, Mater. Des. 194 (2020).

[16]   M. Frank, Y. Chen, S.S. Nene, S. Sinha, K. Liu, K. An, R.S. Mishra, Mater. Today Commun. 23 (2020) 100858.

[17]   S. Shukla, T. Wang, M. Frank, P. Agrawal, S. Sinha, R.A. Mirshams, R.S. Mishra, Mater. Today Commun. 23 (2020) 100869.

[18] P. Agrawal, S. Shukla, S. Gupta, P. Agrawal, R.S. Mishra, Appl. Mater. Today 21 (2020).

[19] K. Liu, S.S. Nene, M. Frank, S. Sinha, R.S. Mishra, Appl. Mater. Today 15 (2019) 525–530.

[20] M. Komarasamy, T. Wang, K. Liu, L. Reza-Nieto, R.S. Mishra, Scr. Mater. 162 (2018) 38–43.

[21] R.S. Mishra, Z.Y. Ma, Mater. Sci. Eng. R Reports 50 (2005) 1–78.

[22] R.S. Mishra. P.S. De and N. Kumar, Friction Stir Welding and Processing: Science and Engineering, Springer, ISBN-13: 978-3-319-07043-8, August 2014, 338 pages.

[23] W.H. Liu, Y. Wu, J.Y. He, T.G. Nieh, Z.P. Lu, Scr. Mater. 68 (2013) 526–529.

[24] R.S. Mishra, M.W. Mahoney, in: Mater. Sci. Forum, Trans Tech Publications Ltd, 2001, pp. 507–514.

[25] M.G. Jo, H.J. Kim, M. Kang, P.P. Madakashira, E.S. Park, J.Y. Suh, D.I. Kim, S.T. Hong, H.N. Han, Met. Mater. Int. 24 (2018) 73–83.

[26] M. Komarasamy, R.S. Mishra, S. Mukherjee, M.L. Young, JOM 67 (2015) 2820–2827.

[27] M. Wang, Z. Li, D. Raabe, Acta Mater. 147 (2018) 236–246.

[28] S.S. Nene, K. Liu, M. Frank, R.S. Mishra, R.E. Brennan, K.C. Cho, Z. Li, D. Raabe, Sci. Rep. 7 (2017) 1–7.

[29] S.S. Nene, M. Frank, K. Liu, R.S. Mishra, B.A. McWilliams, K.C. Cho, Sci. Rep. 8 (2018) 1–8.

[30] W.S. Choi, H.S. Oh, M. Lai, N. V. Malyar, C. Kirchlechner, E.S. Park, P.P. Choi, Scr. Mater. 176 (2020) 122–125.

[31] Y.Z. Tian, L.J. Zhao, S. Chen, A. Shibata, Z.F. Zhang, N. Tsuji, Sci. Rep. 5 (2015) 1–9.

[32] S. Sinha, S.S. Nene, M. Frank, K. Liu, R.S. Mishra, B.A. McWilliams, K.C. Cho, Materialia 6 (2019) 100310.

[33] R.S. Mishra, S.S. Nene, Metall. Mater. Trans. A 52 (2021) 889–896.

[34] R.S. Mishra, R.S. Haridas, P. Agrawal, Materials Science and Engineering A 812 (2021) 141085.

CHAPTER 4

AGING KINETICS RELATED STRENGTH PREDICTION FOR 2195 ALUMINUM ALLOY

USING THE AVRAMI EQUATION

4.1   Abstract

2195 Aluminum (Al) alloy with attractive aerospace applications was studied to explore two aspects, a) fundamental investigations to understand the influence of strengthening precipitates on mechanical properties due to the aging kinetics, and b) building a relationship between the aging time and temperature to obtain the highest strength possible using Avrami equations. The experiments involved heat treatments at two different aging temperatures and multiple hold times. The volume fraction of strengthening precipitates was determined using differential scanning calorimetry (DSC) and substantiated via transmission electron microscopy (TEM). Based on the aging kinetics causing precipitation evolution, a relationship between the ultimate tensile strength (influenced by the formation of the T_1 strengthening phase) and aging time has been established, which were in good agreement with the experimental data.

4.2   Introduction

There is a high demand for lightweight structural alloys, especially in the aerospace industry. Al-Li alloys offer high strength levels comparable to 7XXX high strength aluminum alloys [1,2]. The third generation Al-Li alloys are alloyed with Cu, Mg, and Ag, and one such extensively used alloy is 2195 Al. 2195 Al alloy is used as a material for the lightweight fuel tank in the space shuttle, in the shape of a dome made from friction stir welded (FSW) blanks because of its higher specific strength [3,4]. 2195 Al alloy is a very emblematic treated strengthened alloy, of which the precipitate evolution is singularly sensitive to the heat treatment parameters. It is well documented [5,6] that the second phase's dissolution, formation, and transformation are observed

in the Al alloys during aging treatment, which substantially affects the subsequent microstructure and mechanical properties. The strengthening has been mainly attributed to the formation of metastable precipitates: δ' (Al_3Li), θ' (Al_2Cu), and T_1 (Al_2CuLi) [7,8]. Precipitation plays a crucial role in strengthening and hardening; maximum efficacy can only be attained when coherency is achieved between a precipitate and Al matrix; likewise, a decrease in strengthening is observed with an incoherent interface [4,9]. Ziqiao et al. [10] studied the relationship between microstructure and mechanical properties of 2195 Al under various aging treatments to design and develop the optimal microstructure with improved properties. Thus, suggesting aging at a lower temperature and longer incubation period would improve the combined properties of strength and ductility by enhancing the nucleation and distribution of T_1 and reducing the coarsening rate of precipitates.

Traditionally, improved mechanical properties are obtained by appropriate alloy chemistry and thermo-mechanical treatment. These treatments are carried out based on the parameters optimized by trial and error during several metallurgical experiments, which could be costly and time-consuming. An alternative way is to develop models connecting the process parameters (temperature and time of heat treatment) to mechanical properties. Shercliff and Ashby proposed a systematic approach to model the yield strength by the relating with the process parameters [11]. Lloyd et al. [12] developed a model to study the kinetics of precipitation hardening and predict the yield strength in an Al-Mg-Si-Cu alloy. These model-based approaches have proved to be a cost-effective route to improve the final properties of the 2195 Al alloy [11,13–15].

2195 Al alloy is used in the fuel tank for the space shuttle where the dome shape is made via spin forming of welded blanks, which increases the difficulty in process development due to differences in the formability of the weld [16]. Thus, their coupled influence on the mechanism

and performance of the alloy needs further exploration. Therefore, the investigation of the impact of second phase evolution on the strength under the condition of friction stir welded spin formed and subsequent aging treatment is quite important.

This study aimed to improve the strength of the friction stir welded and formed 2195 Al alloy domes provided by the Korean Aerospace Research Institute (KARI). As for the fundamental methodology, DSC was used to reveal the formation and evolution of strengthening precipitates after post-heat treatments. The validation and analysis of the type, morphology, and size of strengthening precipitates were done using TEM. The other part of the study was to establish a relationship between aging time and temperature to obtain the highest strength using the Avrami equation.

4.3   Materials and Methods

The friction stir welded (tool rotation rate of 400 revolutions per minute & traverse speed of 300 mm/min) and spinned formed dome of 2195 Al alloy were provided by KARI. Figure 4.1(a) shows the dome with the FSW path (red line), the division between the formed region (i.e., spinned region – black line), and the unformed region (i.e., no spinned region – blue line). Vickers hardness profile in Figure 4.1(b) was conducted using a 500 g load (0.5 HV) for the formed region with an average hardness of ~106 HV. Table 4.1 lists the composition of the as-received material compared with standard 2195 Al alloy. To understand the effect of heat treatments on the formed region of the dome, post-weld heat treatment (PWHT) was carried out in an oven in air at different temperatures for different holding times to achieve effective heat treatment to achieve the desired strength. DSC was performed on the as-formed and heat-treated samples using Netzsch 204F1 Phoenix® system to evaluate the kinetics and volume fraction for strengthening precipitate. Selected samples were prepared for TEM using dual-beam FEI Nova 200 Nano Lab focused ion

28

beam microscope. TEM was conducted on FEI Tecnai G2 F20 S-Twin 200 keV. For tensile behavior studies, samples were machined using a computer numerical control (CNC) machine with a gauge length and width of 5 mm and 1.25 mm, respectively. The tensile samples were tested at room temperature with an initial strain rate of 10^{-3} s^{-1}.
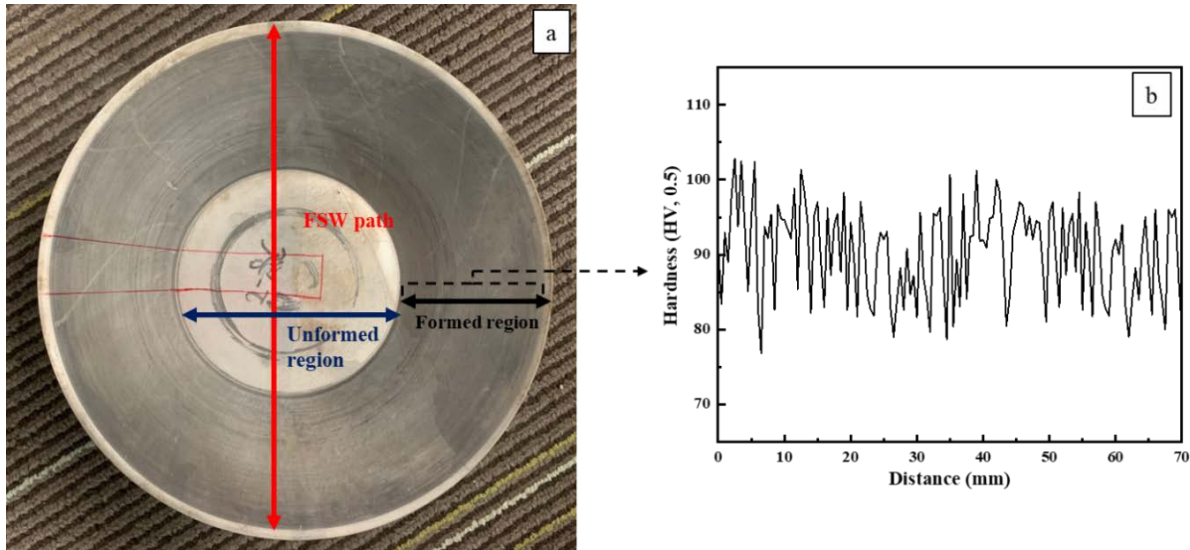
Figure 4.1: (a) Macro image for spinned dome 2195 Al, and (b) hardness profile for the formed region (inside - out).

Table 4.1: Alloy chemistry (wt %)

Alloy	Li	Cu	Mg	Mn	Ag	Zr
AA 2195	0.8-1.2	3.7-4.3	0.25-0.8	Max. 0.25	0.25-0.6	0.08-0.16
As-rec	0.95	3.97	0.31	0.06	0.25	0.14

4.4 Result and Discussion

4.4.1 Heat Treatment

The strengthening by heat treatment is essentially a three-step process. The first step is solution heat treatment, which involves soaking at a high enough temperature and sufficient time to help dissolve phases, leading to a homogenous solid solution. The second step, quenching, results in the supersaturation of the matrix, followed by the third step, i.e., aging, that enables the

formation of precipitates at elevated temperature (artificial aging), leading to the strengthening of material. The phase diagram generated using TC-Prisma in Figure 4.2 aids in deciding the solubility temperatures that lead to precipitation strengthening. The solid solubility of Cu in Al increases as temperature increases from about 0.2 wt.% at 250°C to 5.65 wt.% at the eutectic melting temperature of 548°C. Thus, the temperature for solution heat treatment should be in the range of 450°C to 550°C, and the temperature range for precipitation or aging should lie in the range of 130°C to 260°C. Table 4.2 summarizes the formation and dissolution temperatures for the precipitates in this alloy. Chen and Bhat [9] established that at temperatures below 315°C, strengthening precipitate T_1 is the only phase present.
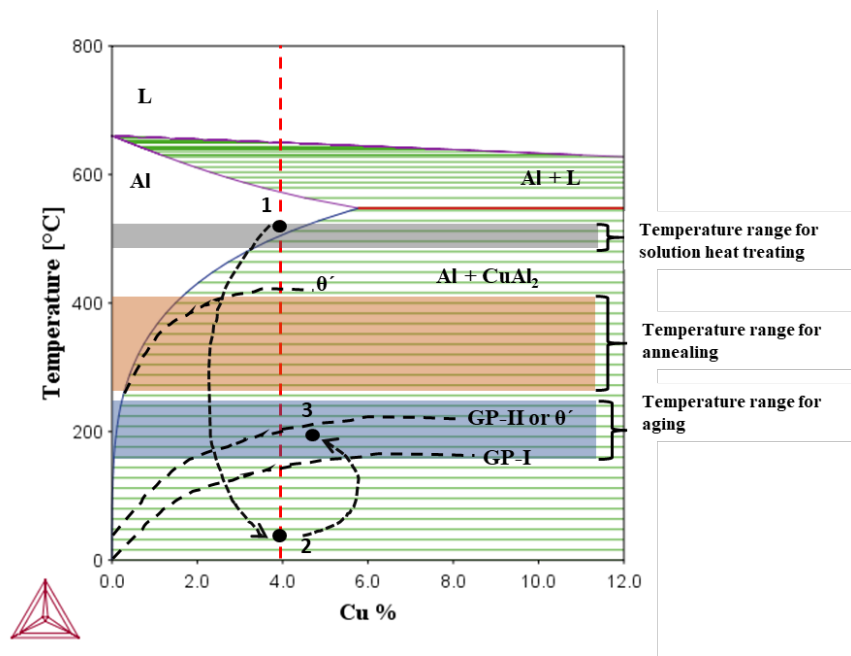
Figure 4.2: Solubility temperature relationship for Al-Cu alloys with Cu in wt%

Table 4.2: Listing the forming and dissolution temperatures for different precipitates

Precipitates	Forming Temperature (°C)	Dissolving Temperature (°C)
GP Zones, δ′	25 – 50	90 – 120
T_1	140 – 310	400 – 470
θ and θ′	320 – 370	430

Using the information about the critical temperatures in Table 4.2, the next step was to calculate the equivalent time (t_{eq}) for aging to form the maximum amount of strengthening precipitate. The peak temperature (T_f) for the formation of strengthening precipitate T1 for as-received material was obtained from the DSC data, as discussed in a later section. Using all the information, t_{eq} (sec) was then calculated for a given isothermal aging temperature by using the following relationship [17]:

$$t_{eq} \cong 0.786 \frac{T_f}{\beta} \left(\frac{RT_f}{E}\right)^{0.95} \exp\left(-\frac{E}{RT_f}\right) \left[\exp\left(-\frac{E}{RT_{iso}}\right)\right]^{-1} \qquad \text{(Eq. 4.1)}$$

where T_f = 275°C (548 K) is the peak temperature for the formation of T_1, T_{iso} is the isothermal heating temperature, E is the activation energy for interested precipitation, R = 8.314 J/mol.K is the gas constant, and β = 10 K/min is the heating rate. For the current work, the activation energy for the precipitate of interest, i.e., T_1, was calculated with the help of Kissinger's equation [18]. Table 4.3 gives the calculations for t_{eq} for different isothermal temperatures for T_1 precipitate formation.

Table 4.3: Calculated isothermal equivalent times for T_1 precipitate formation at different temperatures.

Isothermal temperature (°C)	Equivalent time (h)
140	59
160	16

Table 4.4: Heat treatment schemes for 2195 Al

No.	Heat treatment scheme
PWHT#1	480°C for 25 mins followed by quenching + 140°C aging for 59h
PWHT#2	480°C for 25 mins followed by quenching + 160°C aging for 16h

Based on the calculations, two heat treatment schemes were decided for a detailed study regarding precipitation affecting the strengthening mechanism to improve mechanical properties and help build a relationship between the heat treatment and resulting strength (see Table 4.4).

4.4.2 Mechanical Testing

The first post heat treatment step was to perform mechanical tests of the heat-treated samples and establish the effect of heat treatment on the sample compared to the as-received sample. Comparison of the tensile curves for both the heat treatments compared to the as-received formed sample are shown in Figure 4.3. PWHT# 1 samples in Figure 4.3 (a) showed the most promising results with improvement in the strength and ductility as compared to the as-received material with the highest tensile strength of ~460 MPa and ductility of ~13% when the samples were aged for 120 hours. However, the tensile strength decreased as the aging time increased beyond 120 hours, thus making 120 hours the peak aged condition for PWHT# 1. The highest tensile strength and ductility, ~414 MPa and ~ 9%, respectively, observed during the PWHT#2, were for aging conditions of 160°C for 96 hours. The drop in tensile strength is observed for PWHT#2 when the samples were aged beyond 96 hours. Table 4.5 summarizes the effect of different heat treatments on tensile properties for the peak-aged and over-aged conditions compared to as-received material.
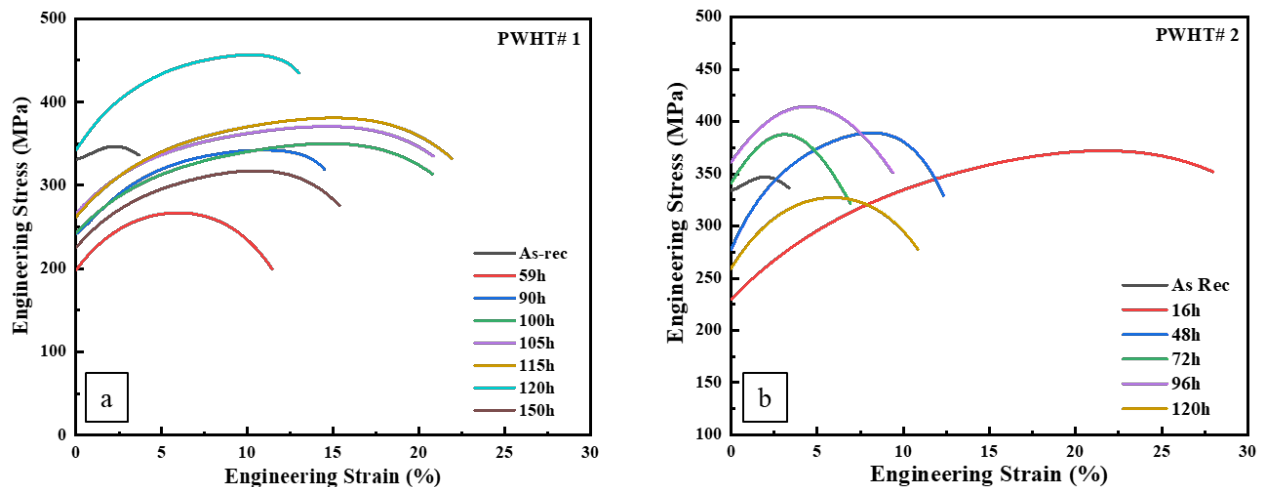
Figure 4.3: Engineering stress-strain curves for (a) PWHT# 1- 480°C for 25 mins + 140°C for minimum 59hrs and (b) PWHT# 2 - 480°C for 25 mins + 160°C for minimum 16hrs of 2195 Al aged for varying aging hours.

Table 4.5: A summary of tensile properties for different conditions.

No.	Condition	Aging time (h)	YS (MPa)	UTS (MPa)	Ductility (%)
PWHT# 1	Peak-aged	120	336 ± 2	456 ± 3	13 ± 0.5
	Over-aged	150	224 ± 1	317 ± 2	15 ± 0.3
PWHT# 2	Peak-aged	96	360 ± 0.5	414 ± 3	9 ± 0.2
	Over-aged	120	260 ± 1	327 ± 2	11 ± 0.6
Base	As- received	-	330 ± 2	346 ± 1	4 ± 0.2

4.4.3 Differential Scanning Calorimetry (DSC)

Figure 4.4 shows the DSC curves for the two heat treatments performed on the formed region of the 2195 Al dome compared to the as-received material. An exothermic reaction is seen accompanied by a precipitation phenomenon, where endothermic reactions are a dissolution reaction of precipitates into the matrix. Several endothermic and exothermic events common to the Al-Cu-Li system have been identified. The prominent exothermic peak A is due to the precipitation of the T_1 phase, whereas peak B is a large endothermic peak, the dissolution event of T_1, and other high-temperature phases formed [19,20].

The DSC curve for samples aged at 140°C for 59 hours, i.e., PWHT# 1 in Figure 4.4(a), showed a larger area under the curve for the precipitation formation (peak A) than the as-received material. The curve for 120 hours has the highest peak, i.e., the highest volume fraction of the T_1 phase, due to the dissolution of low-temperature precipitates and aiding the formation of the strengthening precipitates. The curves for longer than 120 hours show a reduction in the area under the curve, meaning the coarsening of T_1 precipitation took place with longer aging hours. The tensile test showed high strength for sample aged for 120 hours at 140°C and drop in strength was observed when sample were aged beyond 120 hours. For PWHT#2, no low-temperature precipitates are observed when subjected to heat treatment in Figure 4.4(b). Thus, high aging

temperature allows the formation of homogenized solid solution, and enough solute in the matrix was available for the formation of strengthening precipitate. However, after aging for 96 hours at 160°C, as shown in Figure 4(b), peak strengthening is observed, and aging beyond 96 hours shows flattening of the exothermic peak, suggesting that no more solute was available in the matrix to form T_1 precipitates. Thus, a drop in strength for PWHT# 2 sample aged for 120hours is observed in Figure 4.3(b). Correlating the aging kinetics occurring during heat treatment with the mechanical behavior, it was clear that 120 hours and 96 hours for PWHT#1 and PWHT#2 respectively showed the highest strength, thus marking them as peaked aged condition, whereas everything beyond peak aged condition can be considered as an over-aged condition.
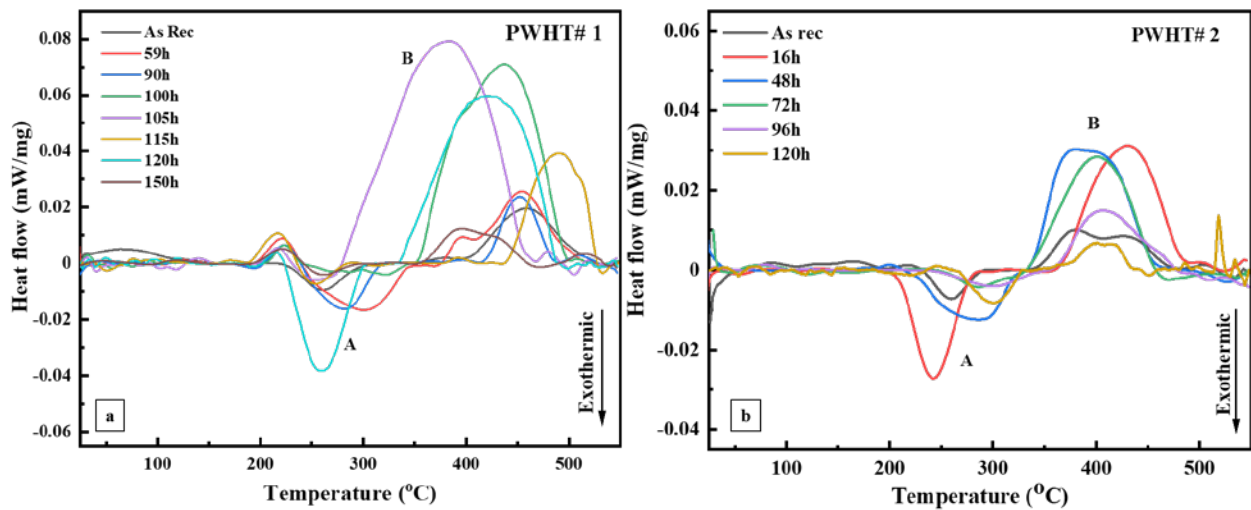
Figure 4.4: DSC results of 2195 Al aged for different times compared to as-received 2195 Al (a) PWHT#1 and (b) PWHT#2.

4.4.4 Microstructural Characterization

TEM investigation revealed the type, fraction, and distribution of precipitates formed during aging compared with the as-received material. Establishing the orientation relationship between the matrix and precipitates facilitates a deeper analysis of the precipitation kinetics leading to strengthening precipitates. A study by Na et al. [21] suggests that 2195 Al is

strengthened predominantly by uniform dispersion of T_1 plates and additionally by a small fraction of θ' plates, and cold-working prior to aging does affect the volume fraction of these strengthening precipitates, and shape and size of the grains [22]. Figure 4.5 compares as-received to peak-aged and over-aged samples from PWHT#1.
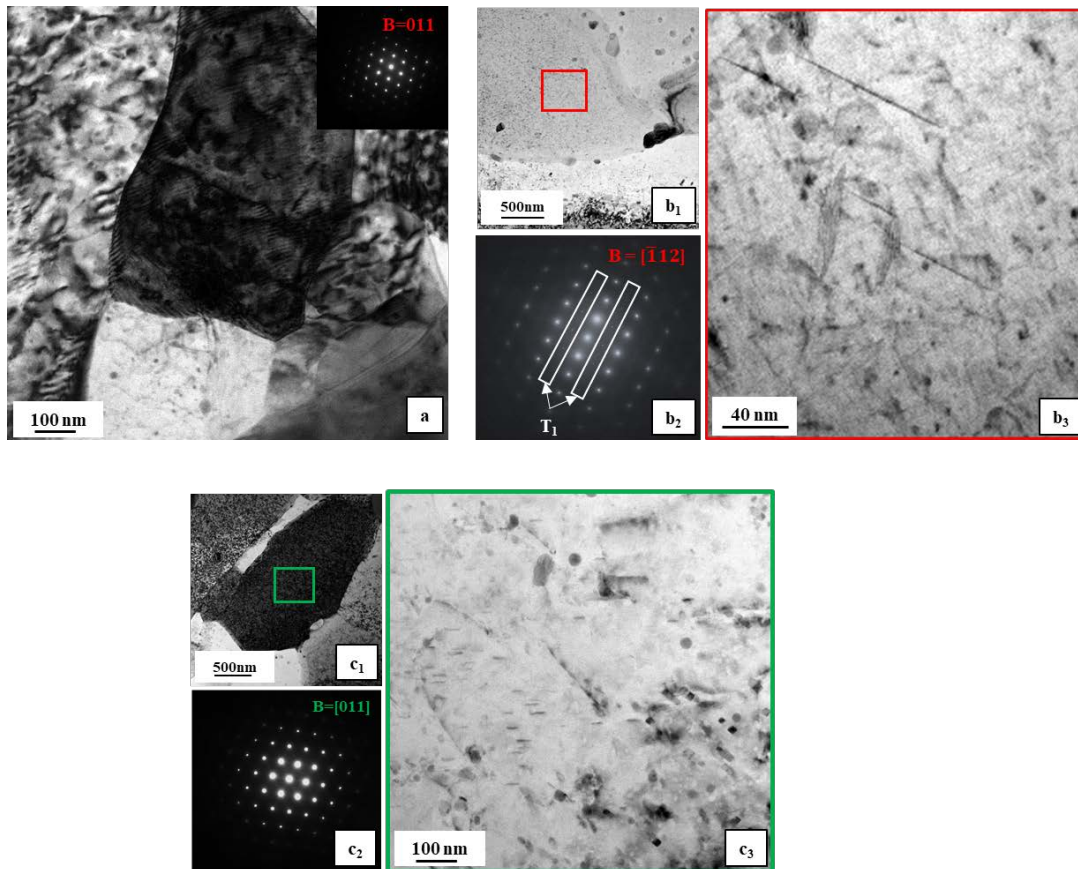
Figure 4.5: TEM images of (a) as-received, ($b_1 - b_3$) BF image of grain taken along the [112]Al diffraction pattern with the presence of T_1 precipitates for the peak-aged condition, and ($c_1 - c_3$) BF images of grain taken along [011]Al direction indicating the coarsening in T_1 precipitates for the over-aged condition.

Figure 4.5(a) for the as-received sample shows that T_1 precipitates exist scarcely in the Al matrix as the solute is dissolved in the matrix due to the spin forming step involved in forming a dome. Figure 4.5(b) shows the bright field (BF) images of the PWHT# 1 sample aged for 120 hours along with diffraction patterns. Figures 4.5(b_1 and b_3) shows the low and high magnification BF images taken along the [112]$_{Al}$ direction. The image shows the presence of large volume fraction of plate-

like T_1 precipitates, and the faint streaks marked in the white box validate the results in the diffraction pattern in Figure 4.5(b_2). The density of T_1 precipitates in the PWHT#1 for peaked condition (Figure 4.5b) is higher than the as-received material in Figure 4.5(a). These results validate the sensitivity towards temperature and time for the precipitation of strengthening phase T_1 in 2195 Al, thus providing a plausible reason for the highest tensile strength observed in the peaked aged condition. However, the TEM images in Figure 4.5(c_1, c_2) were taken along the [011]$_{Al}$ direction represent the over-aged sample of PWHT#1. It was observed that the density of the T_1 precipitates has reduced in comparison to the peak aged sample of PWHT#1. The reduced volume fraction of T_1 in Figure 4.5(c_3) proves the coarsening of precipitates due to over-aging and validates the reason for low strength, and improved ductility (as shown in Table 4.5) observed in the over-aged condition.

4.4.5   Constitutive Relationship Model Using Avrami Equation

Based on the aging kinetics and mechanical behavior, a mathematical relationship using the Avrami equation is built to calculate the aging cycle for the sample to achieve maximum strength. The total volume fraction of the T_1 phase during aging treatment follows the Avrami law [23–25] and can be given by Eq. 4.2:

$$f_v = 1 - e^{-kt^n} \tag{Eq. 4.2}$$

where f_v is the transformed volume fraction, t is the aging time, and k and n are rate constant and Avrami index, respectively.

From Equation (4.2), the volume fraction of T_1 would slowly increase with the increasing aging time and eventually reach a constant value. The volume fraction of T_1 directly impacts the final properties like maximum strength achieved by the material. Hence a constitutive relationship model is designed based on the application of Eq. 4.2 using tensile test data obtained by two heat

36

treatments in the previous section. To model the aging kinetics of 2195 Al, the Avrami equation is demonstrated in terms of time (hours), temperature (K), and UTS (MPa) [26]. In this model, f_v in Eq. 4.2 was replaced by strength (S), which is thus described as:

$$S = 1 - \exp\left(-\left(\frac{t}{t_c}\right)^n\right) \tag{Eq. 4.3}$$

where, t_c is a time-dependent constant and n is a constant related to the diffusion condition. While S and t_c can be defined as:

$$S = \frac{S_t - S_i}{S_{max} - S_i} \tag{Eq. 4.4}$$

$$t_c = t_0 \exp\left(\frac{E}{RT}\right) \tag{Eq. 4.5}$$

where S_{max} is the maximum strength and S_i and S_t are the strength of the as-received material and UTS after aging for time t, respectively. E is the activation energy, R is the universal gas constant, T is the aging temperature, and t_0 is a time-related constant.
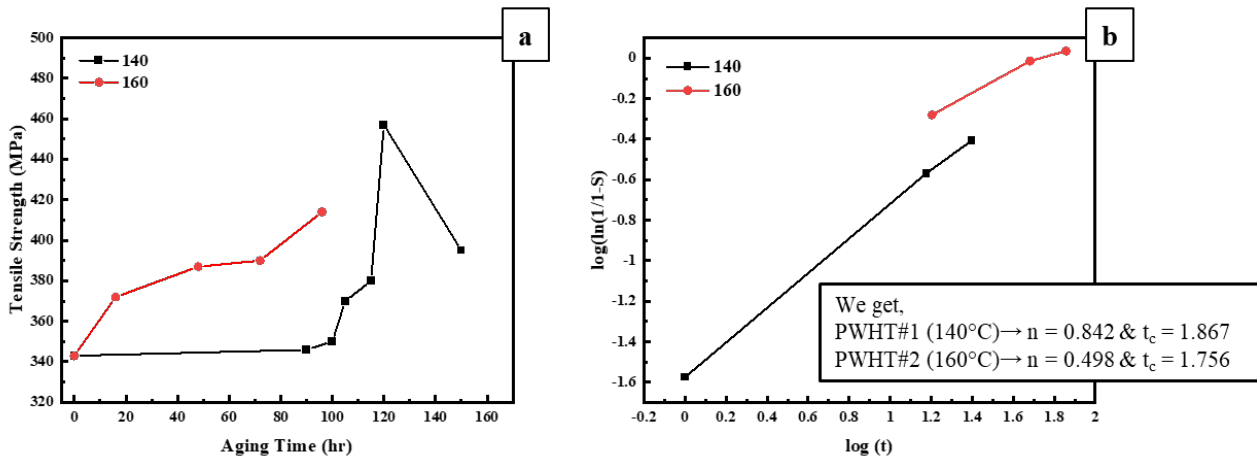
Figure 4.6: (a) UTS trend obtained from the tensile test of 2195 Al after aging at 433K, 413 K for different aging times and (b) log(ln(1/(1-S))) vs. log(t) plot showing the compliance of avrami equation to the degree of transformation.

In isothermal treatment, with increasing aging times, the strength of material increases to a maximum and, thereafter, decreases. Figure 4.6 (a) shows a similar UTS trend obtained from the tensile test after the samples are subjected to solution treatment and aging at different times and

temperatures. Figure 4.6(b) shows the graph of log(ln(1/(1-S))) versus log(t) which is plotted based

on Eq. 4.3. The values of n and t_c determined through linear fitting are shown in Figure 4.6(b). The

results show that n is 0.842 and 0.498 for PWHT#1 and PWHT#2, respectively, indicating the

nucleation rate of strengthening precipitates in 2195 Al. These are fully consistent with the

variation range of n from 0.4 to 4, depending on the nucleation rate [27].

The values obtained from Figure 4.6(b) helped to build relationships using the Arrhenius

equation between temperature (T) and n and t_c, as shown in Eq. 4.6 and 4.7, respectively.

$$n = \frac{3077}{T} - 6.61 \tag{Eq. 4.6}$$

$$t_c = \exp(\frac{5541}{RT} - 0.98) \tag{Eq. 4.7}$$

The next step is to build a relationship between the maximum strength and aging time and

temperature. As the aging temperature increases, the maximum strength drops due to insufficient

time for nucleation and growth of strengthening precipitates. Table 4.5 shows the trend between

the aging time and temperature and strength obtained at the peak-aged condition for both heat

treatments. Using the strength at peak aged condition, a relationship is established using Eq. 4.8

between maximum strength and temperature, and the aging time to reach the maximum strength

is calculated using the power law equation [28] as shown in Eq. 4.9.

$$S_{max} = S_i + S_0 \exp\left(\frac{S_1}{T}\right) \tag{Eq. 4.8}$$

$$T = T_0 (t_{max})^{t_0} \tag{Eq. 4.9}$$

where S_0 and S_1 are two material-dependent constants, the values were obtained by linear fitting

the curve using Eq. 4.8. Similarly, t_0 and T_0 were obtained by linear fitting the curve obtained using

Eq. 4.9.

The final relationship to predict maximum strength achieved by the material at any specific

temperature and time using the relationships developed above are:

$$S_t = S_i + \left(1 - \exp\left(-\left(\left(\frac{t}{\exp\left(\frac{5541}{RT}\right)-0.989}\right)^{\left(\frac{3077}{T}-6.61\right)}\right)\right)\right) * \left(0.004 \exp\left(\frac{4234}{T}\right)\right) \quad \text{(Eq. 4.10)}$$

$$T = 7.038(t_{max})^{-0.21} \quad \text{(Eq. 4.11)}$$

To validate the model, a new heat treatment plan was designed with the help of Eq. 4.10 and 4.11. The samples were heat-treated at 480°C for 25 mins, followed by water quenching, and then aged at 150°C for 107 hours. The aging time of 107 hours was calculated with the help of the relationship established in Eq. 4.11, and the calculated maximum strength of 431 MPa is calculated using Eq. 4.10. Figure 4.7 compares calculated and experimental results for aging kinetics of 2195 Al. The experimental results agree with the theoretical ones with an error of ~0.4 %, suggesting that using this model, both maximum strength and time to reach that maximum strength at different temperatures can be correctly estimated. It should be noted that the primary assumption of the Avrami equation is the formation of a strengthening single-phase from a matrix of another phase, although in the precipitation of 2195 Al, different metastable precipitates form simultaneously. Hence, using the Avrami equation for each precipitate could not match the experimental data exactly.
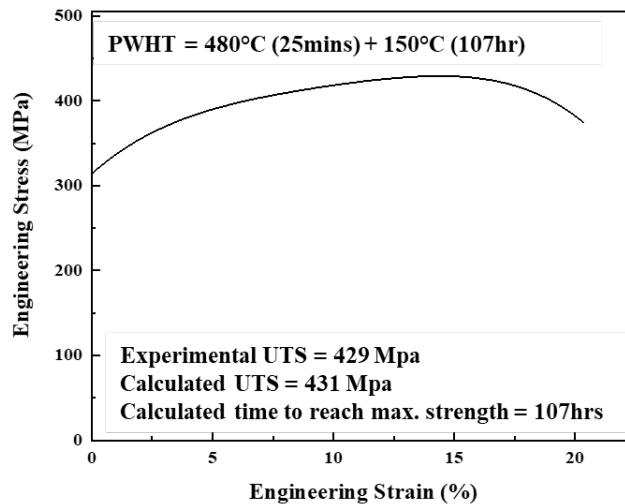
Figure 4.7: Calculated and experimental results for age hardening of 2195 Al at 150°C

4.5   Conclusions

Solid solution and variable artificial aging temperature and time were applied to the formed region of the 2195 Al dome. Different heating treatments on 2195 Al samples resulted in T_1 nucleation in the matrix, which could be dominant to sufficiently induce strengthening. The highest strength was achieved in the PWHT#1 sample aged 120 hours due to the more significant volume fraction of the T1 phase as observed in DSC results and validated by the TEM imaging. A strong correlation between the temperature and aging times using the avrami equation was established and validated with the experimental data. The Avrami equation can be used for future heat treatment design and is likely to cut down the experimental effort for strength-ductility optimization in components processed by different manufacturing methods.

4.6   References

[1]   I.N. Fridlyander, A. V. Dobromyslov, E.A. Tkachenko, O.G. Senatorova, Advanced high-strength aluminum-base materials, Met. Sci. Heat Treat. 47 (2005) 269–275.

[2]   E.A. Starke, J.T. Staley, Application of modern aluminum alloys to aircraft, Prog. Aerosp. Sci. 32 (1996) 131–172.

[3]   Z.M. Wang, R.N. Shenoy, Microstructural Characterization of Aluminum-Lithium Alloys 1460 and 2195, 1998.

[4]   L. Dong, J. Schneider, Microstructural investigation of AA 2195 T81 chips formed during a metal-cutting process, J. Mater. Sci. 43 (2008) 7445–7450.

[5]   W.J. U.G. Gang, S.H. Lee, The evolution of microstructure and mechanical properties of A 5052 aluminium alloy by the application of cryogenic rolling and warm rolling, Mater. Trans.,. 50(1) (2009) 82–86.

[6]   Z.Q. H. Li, L.H. Zhan, M.H. Huang, X. Zhao, C. Zhou, Effects of pre-strain and stress level on stress relaxation ageing behaviour of 2195 Al-Li alloy: experimental and constitutive modelling, J. Alloy. Compd.,. 851 (2021).

[7]   S. Zhang, W. Zeng, W. Yang, C. Shi, H. Wang, Ageing response of a Al-Cu-Li 2198 alloy, Mater. Des. 63 (2014) 368–374.

[8] B.P. Huang, Z.Q. Zheng, Independent and combined roles of trace Mg and Ag additions in properties precipitation process and precipitation kinetics of Al-Cu-Li-(Mg)-(Ag)-Zr-Ti alloys, Acta Mater. 46 (1998) 4381–4393.

[9] P.S.Chen, B.N.Bhat, Time-Temperature-Precipitation Behavior in AI-Li Alloy 2195, 2002.

[10] Z. Ziqiao, H. Biping, Effect of heat treatments on tensile properties and microstructure of 2195 alloy, J. Cent. South Univ. Technol. 5 (1998) 14–17.

[11] H.R. Shercliff, M.F. Ashby, A process model for age hardening of aluminium alloys—II. Applications of the model, Acta Metall. Mater. 38 (1990) 1803–1812.

[12] S. Esmaeili, D.J. Lloyd, W.J. Poole, A yield strength model for the Al-Mg-Si-Cu alloy AA6111, Acta Mater. 51 (2003) 2243–2257.

[13] D.H. Bratland, Grong, H. Shercliff, O.R. Myhr, S. Tjøtta, Modelling of precipitation reactions in industrial processing, Acta Mater. 45 (1997) 1–22.

[14] O.R. Myhr, O. Grong, S.J. Andersen, Modelling of the age hardening behaviour of Al–Mg–Si alloys, Acta Mater. 49 (2001) 65–75.

[15] A. Deschamps, Y. Brechet, Influence of predeformation and ageing of an Al–Zn–Mg alloy—II. Modeling of precipitation kinetics and yield stress, Acta Mater. 47 (1998) 293–305.

[16] J.H. Yoon, J.T. Yoo, K.J. Min, H.S. Lee, A Study on Post Weld Heat Treatment of Friction Stir Welded Al2195 Blank for Spin Forming, Adv. Mater. Res. 1125 (2015) 190–194.

[17] M.J. Starink, Analysis of aluminium based alloys by calorimetry: Quantitative analysis of reactions and reaction kinetics, Int. Mater. Rev. 49 (2004) 191–226.

[18] H.H. Jung, Y.R. Lee, K.J. Min, H.S. Lee, A Study on Precipitation Kinetics of an Al-Cu-Li Alloy, Appl. Mech. Mater. 736 (2015) 3–6.

[19] H. Sidhar, R.S. Mishra, Aging kinetics of friction stir welded Al-Cu-Li-Mg-Ag and Al-Cu-Li-Mg alloys, Mater. Des. 110 (2016) 60–71.

[20] J.H. Kim, J.H. Jeun, H.J. Chun, Y.R. Lee, J.T. Yoo, J.H. Yoon, H.S. Lee, Effect of precipitates on mechanical properties of AA2195, J. Alloys Compd. 669 (2016) 187–198.

[21] N. Jiang, X. Gao, Z.Q. Zheng, Microstructure evolution of aluminum-lithium alloy 2195 undergoing commercial production, Trans. Nonferrous Met. Soc. China (English Ed. 20 (2010) 740–745.

[22] S. Qin, S. Lee, T. Tsuchiya, K. Matsuda, Z. Horita, R. Kocisko, T. Kvackaj, Aging behavior of Al-Li-(Cu, Mg) alloys processed by different deformation methods, Mater. Des.,. 196 (2020).

[23] Y.X. Wang, G.Q. Zhao, X. Xu, X.X. Chen, C.S. Zhang, Constitutive modeling, processing map establishment and microstructure analysis of spray deposited Al-Cu-Li alloy 2195, J. Alloy. Compd. 779 (2019) 735–751.

[24] L.W. Zhong, W.L. Gao, Z.H. Deng, Z. Lu, G.L. Mao, Microstructure characteristics and constitutive modeling for elevated temperature flow behavior of Al-Cu-Li X2A66 alloy, J. Mater. Res.,. 33 (8) (2018).

[25] M.C. Weinberg, D.P. Birnie, V.A. Shneidman, Crystallization kinetics and the JMAK equation, J. Non Cryst. Solids. 219 (1997) 89–99.

[26] W. Sha, Application of simple practical models for early stage ageing precipitation kinetics and hardening in aluminium alloys, Mater. Des. 28 (2007) 528–533.

[27] J. Kohout, An alternative to the JMAK equation for a better description of phase transformation kinetics, J. Mater. Sci. 2007 434. 43 (2007) 1334–1339.

[28] A.R. Eivani, A.K. Taheri, Modeling age hardening kinetics of an Al–Mg–Si–Cu aluminum alloy, J. Mater. Process. Technol. 205 (2008) 388–393. https://doi.org/10.1016/J.JMATPROTEC.2007.11.195.

CHAPTER 5

INFLUENCE OF WELDING PARAMETERS ON MECHANICAL, MICROSTRUCTURE,

AND CORROSION BEHAVIOR OF FRICTION STIR WELDED ALUMINUM 7017

ALLOY*

5.1 Abstract

Fusion welding of age-hardenable high strength aluminum (Al) alloys can be challenging

due to the propensity of these alloys to develop solidification-related issues such as porosity and

microcracking. A solid-state welding technique, such as friction stir welding (FSW), offers an

excellent alternative to fusion welding by minimizing solidification-related defects in high strength

Al alloys. While high quality welds of high strength Al alloys are possible with FSW, the process

is highly dependent on the welding parameters. The present study attempts to correlate welding

parameters to weld quality using a systematic approach spanning microscopic to macroscopic

length scales. Mechanical and corrosion testing shows the influence of the traverse speed on the

different weld zones. Higher traverse speed shows higher yield strength and better re-passivation

corrosion resistance ~287 MPa and ~ -0.958V compared to slower traverse speed weld ~264MPa

and ~ -0.97V.   The dissolution, reprecipitation, growth, and coarsening of precipitates in the weld

zones are validated via detailed differential scanning calorimetry (DSC) and microstructural

evaluation using transmission electron microscopy (TEM), revealing the effect of welding

parameters. In addition, the mechanical and corrosion properties of the weld improved with post-

weld heat treatment, further substantiated with microscopy detailing the changes in precipitate

morphology in the weld zones. Finally, some guidelines are provided to assist in selecting

parameters for FSW of age hardenable high strength Al alloys to control the width of the HAZ.

5.2   Introduction

High-strength Al alloys such as the 7xxx and 2xxx series are primarily used in aircraft structures and have numerous aerospace industry applications [1]. Joining the 7xxx series using conventional fusion welding techniques is difficult and undesirable, as the formation of dendritic microstructure, microcracks, and porosity during fusion welding undermine the structural integrity of the weldments [2,3]. Friction stir welding (FSW), invented in 1991, is a solid-state joining method that inherently eliminates the drawbacks of fusion welding of high-strength Al alloys [2–5]. FSW of precipitation strengthened Al alloys results in the formation of distinct microstructural zones such as weld nugget (WN), thermo-mechanically affected zone (TMAZ), and heat affected zone (HAZ). WN is characterized by recrystallized grains due to frictional heating and large deformation strain, whereas TMAZ, which experiences less heat and deformation, primarily consists of deformed parent grains with high dislocation density. HAZ has been identified as the weakest zone due to coarsening of pre-existing parent material precipitates caused by the thermal cycle during welding [5].

7xxx series is a category of high-strength precipitation strengthened Al alloys with Zn, Mg, and Cu as the main alloying elements. The typical precipitation sequence in a 7xxx alloy is as follows [6–8],

$$\alpha_{supersaturated\ solid\ solution}\ \rightarrow GP\ Zones\ \rightarrow Metastable\ \eta'\ \rightarrow Stable\ \eta.$$
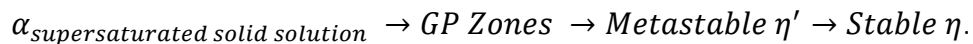
For 7xxx alloys, GP zones form at room temperature and up to 60°C and 100°C [9,10]. They tend to be spherical and are fully coherent with the Al-rich matrix. They are Zn-rich clusters, which form parallel to {111} matrix and usually are 1-2 atoms thick. GP zones are precursors to the η´ phase. The η´ phase is the semi-coherent strengthening phase and has a hexagonal crystal

44

structure with lattice parameters a= 0.496nm and c= 1.405nm [11,12]. It can either be formed from GP zones or directly at higher temperatures (120°C - 180°C). The η phase is the stable precipitate and has a hexagonal crystal structure with lattice parameters of a= 0.521nm and c= 0.86nm [11]. It forms at a temperature above 180°C or longer aging times at lower temperatures. Precipitate type and size depend mainly on aging, processing temperature, and time.

A plenitude of studies exist on FSW of 7xxx alloys [6,7,13–19]. Most of these studies focused on the evolution of microstructure and strength after FSW in as-welded (AW) and post-weld heat treatment (PWHT) conditions. Sullivan and Robinson et al. [6] studied the microstructural evolution due to the FSW of Al 7449-T7 alloy in AW and PWHT conditions. They concluded that extensive coarsening during cooling of the weld and after PWHT resulted in loss of strength in the HAZ. Reynolds et al. [13] studied the correlation between a wide range of FSW parameters and hardness evolution in the WN and HAZ of Al 7050 alloy in AW and PWHT conditions. Their results demonstrated that for all the tested parameters, hardness in the HAZ showed a negative response to PWHT. A study by Dumont et al. [20] showed that the hardness values improved in the HAZ with higher traverse speeds. A low rotational rate and a fast traverse speed led to a colder run. With a slower traverse speed, more time is spent on each weld segment; thus, more heat is dissipated throughout the workplate, resulting in a broader HAZ. A study on the microstructural variation in the HAZ and WN during FSW led to variations in hardness and corrosion resistance of Al 7075 welds, as reported by Rao et al. [21]. Softening of the HAZ is one reason why the corrosion resistance is poor. However, PWHT is used for improving the mechanical properties and corrosion resistance of the welds. Lumsden et al. [22] demonstrated that welds are more susceptible to intergranular corrosion (IGC) than the base material (BM) in chloride solution. Paglia et al. [23] observed that the HAZ of the FSW of Al 7075 exhibited the

highest susceptibility to pitting corrosion in 3.5 wt% NaCl solution, and it was correlated with the sensitization level within the grain boundaries. A comprehensive TEM analysis of FSW of Al 7050 by Su et al. [18] suggested that the WN consists of fine η precipitates and GP zones. However, the η´ precipitates in the HAZ are significantly coarser than those in the BM microstructure which has the highest density of η´ phase. Thus, making the HAZ a weaker region compared to both the WN and BM.

As the FSW process induces a dramatic change in microstructure, several attempts have been made to understand the microstructural evolution and microstructure-property relations of 7xxx alloys after FSW. However, no detailed analysis correlating the effect of traverse speed on mechanical properties and corrosion resistance of the Al 7017 alloy is available at present. Al 7017 has a significantly lower percentage of Zn and Cu alloying content compared to Al 7075 and Al 7050 alloys. Thus, the present work was mainly conducted to investigate the effect of traverse speeds on the nugget and HAZ mechanical properties and localized corrosion behavior of friction stir welded Al 7017 – T651 alloy plates; while correlating these properties with the detailed microstructural characterization via TEM and DSC analysis.

5.3   Materials and Methods

The material used for the study was Al 7017-T651 (12 mm thick) with alloy chemistry presented in Table 5.1. Figure 5.1(a) shows the schematic of the FSW of Al 7017-T651 carried out on an MTI RM-1 FSW machine with a constant tool rotational rate, two different tool traverse speeds, and a tool tilt angle of 1.5° with a Cu backing plate as given in Table 5.2 along with the macroscopic images of the runs in Figure 5.1(c). The tool used for welding consisted of a 6 mm long step-spiral conical pin and a shoulder diameter of 12 mm, shown in Figure 5.1(b). Temperature evolution at the center of the tool pin was also recorded for all the welds using a

thermocouple. PWHT was carried out in an oven in air at 121 ℃ for 24 hours for all parameters.

Table 5.1: Nominal compositional limits of alloying elements in alloy Al 7017-T651 (wt %)

Alloy	Zn	Mg	Cu	Al
7017	4.0-5.0	2.0-3.0	0.2 (max)	Bal
As rec	4.95	2.22	0.2	Bal

Table 5.2: Welding parameters used for FSW of Al 7017-T651

Weld	Rotating speed RPM	Travel speed IPM (mm/min)	Remarks
Run#1	300	2 (50.8)	Slower run
Run#2	300	6 (152.4)	Faster run

Vickers microhardness mapping across the weld cross-section was conducted using a 500 g load (HV0.5), as shown in Figure 1(a). Uniaxial tensile tests across the weld were conducted in AW and PWHT conditions using MTS 322 load frame equipped with a 500 kN load cell along with in-situ imaging using digital image correlation (DIC) for strain mapping. VIC-2D software was utilized for DIC image analysis to understand the localized strain distribution in the welds. Uniaxial tensile samples were machined with the help of a computer numerical control (CNC) machine as per ASTM standard E8 with a gauge length of 25mm. The tensile specimens were tested at room temperature with an initial strain rate of 10^{-3} s^{-1}. Electrochemical studies were conducted on AW and PWHT condition samples at room temperature in 3.5% NaCl solution at least three times to confirm the repeatability of the results. Cyclic potentiodynamic polarization scans were made with a 0.166 mV/sec scan rate. All electrochemical measurements used a saturated calomel electrode (SCE) as a reference electrode and platinum as a counter electrode. DSC was performed to understand the precipitate kinetics and evaluate volume fraction for the different zones observed during FSW, i.e., WN, HAZ, and BM of AW and PWHT conditions. A Netzsch 204F1 Phoenix® system was used to perform DSC with a heating rate of 20°C/minute.

Samples for TEM were prepared using a dual-beam FEI Nova 200 Nano Lab focused ion beam microscope. TEM was conducted on selected samples using FEI Tecnai G2 F20 S-Twin operating at 200 keV.
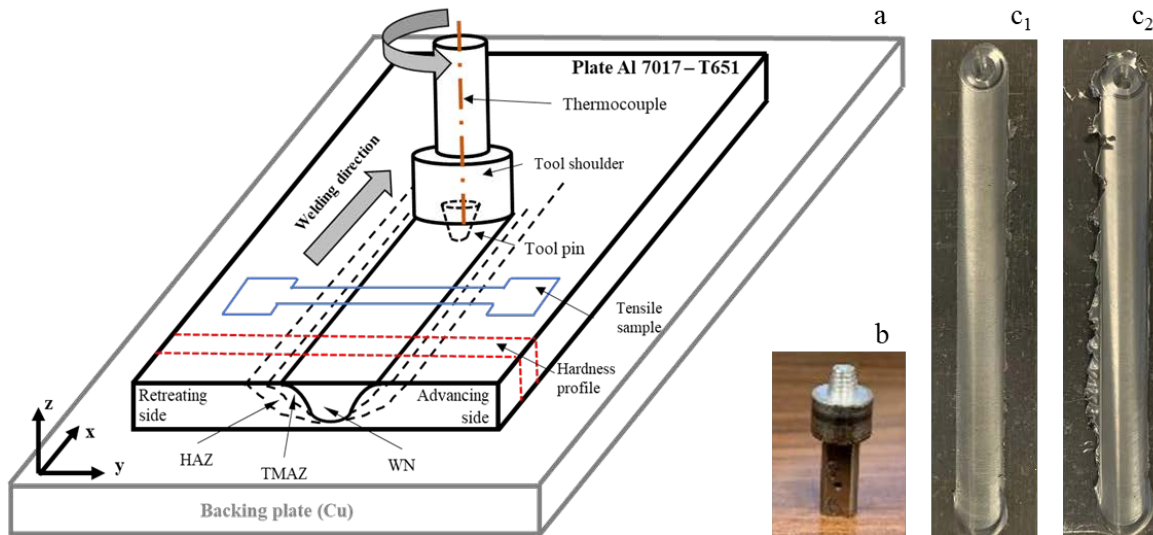
Figure.5.1: (a) Schematic of FSW with a thermocouple inserted in the tool and locations marked for hardness profile and tensile samples, (b) tool used with pin length 6mm and shoulder 12mm, and (c1-c2) macro images of the runs 300 rpm/ 2 ipm and 300 rpm/ 6ipm respectively.

5.4   Results

5.4.1   Temperature Evolution during Welding

Temperature evolution during the entire welding process is shown in Figure 5.2(a). Data were plotted to emphasize welding temperature during the tool traverse, as shown in Figure 5.2(b). The nugget temperature was measured with the help of a thermocouple inserted at the center of the tool pin, as shown in Figure 5.1(a). It is important to note that, due to different thermo-physical properties of the tool and workpiece materials, there will be a temperature difference between the tool center (where the thermocouple was placed) and the actual weld nugget. Peak temperature during FSW of the slower run (Figure 5.2a), i.e., 300 rpm/2 ipm, varied around ~371°C (Figure 5.2 b). In FSW of the faster run, i.e., 300 rpm/6 ipm, the tool spends a reduced amount of time at each point, thus the peak temperature reduced to around ~358°C (Figure 5.2b).

48
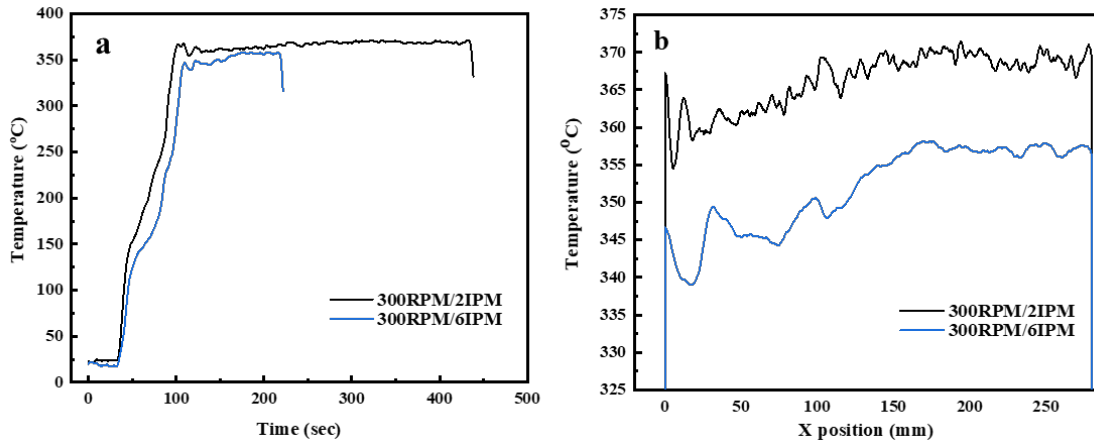
Figure 5.2: (a) Temperature evolution at the center of the tool during each case of FSW, and (b) temperature variation during tool traverse where X-position represents distance traversed by welding tool along the welding direction.

5.4.2   Mechanical Testing

Figure 5.3 shows the maps of Vickers microhardness measurements taken across the weld cross-section for all the different parameters in AW and PWHT conditions compared to the BM. The effect of traverse speed on the mechanical property is evident from the AW hardness profile across the WN, HAZ, and BM. For the 300 rpm/2 ipm run, in Figure 5.3(a), a minimum hardness of 111 ± 2 HV was recorded in the HAZ and 123 ± 3 HV in the WN. The WN for 300 rpm/6 ipm showed minor improvement in the hardness; however, the HAZ (119 ± 2 HV) region showed improved hardness compared to the slower run. The hardness knockdown in HAZ is believed to be due to dissolution and coarsening of precipitates due to heat generated during welding, a typical observation in FSW of precipitation-strengthened Al alloys [24]. Hardness results for PWHT samples are shown in Figure 5.3(b). Post weld heat treatment, hardness for 300 rpm/2 ipm run improved by 5 ± 1.5 HV in the WN and ~3 ± 1 HV in the HAZ, whereas in the 300 rpm/6 ipm run, hardness improvement is visible in the entire weld region. In the HAZ for PHWT of 300 rpm/6 ipm run, a substantial hardness improvement by 7 ± 1.5 HV was obtained, and WN improved by 5 ± 1 HV.
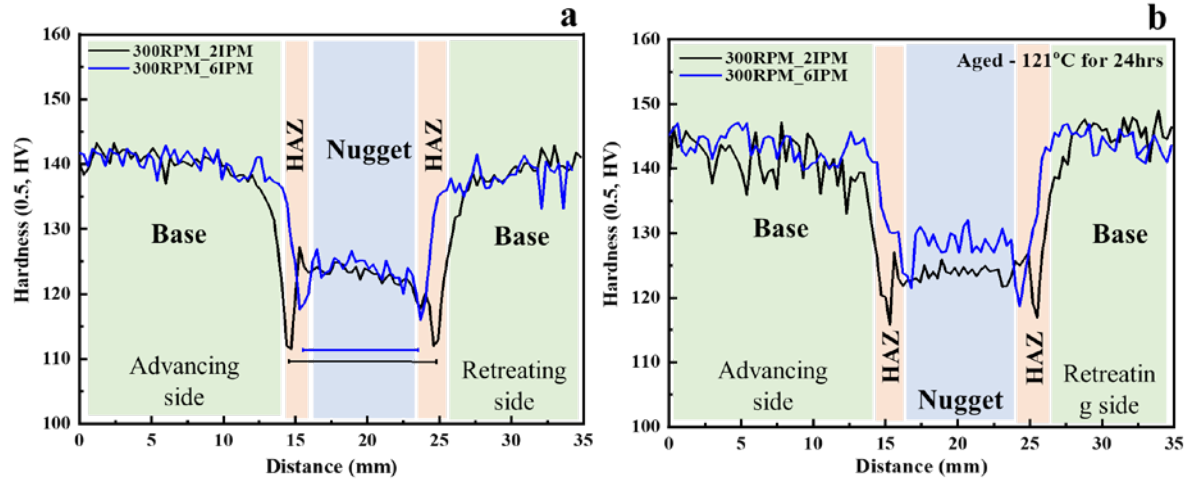
Figure 5.3: Vickers microhardness profile for (a) AW and (b) PWHT conditions for different parameters.

Uniaxial tensile testing results of samples from the welds in all conditions compared to BM are shown in Figure 5.4. The uniaxial tensile test was conducted on BM and FSW joints to quantify the mechanical response of the weld when subjected to load. The local tensile behavior of different weld zones was evaluated by calculating the local stress-strain curves from local strain fields registered using DIC techniques. Yield strength (YS), ultimate tensile strength (UTS), and elongation to failure were calculated for each condition. Joint efficiency (JE) based on YS was also calculated for specimens in each condition and was based on the following ratio,

$$JE = \frac{Weld\ strength\ (YS)}{Base\ metal\ strength\ (YS)}.$$

Point A in Figure 5.4 represents the start of plastic deformation, point B is the yield point, point C corresponds to the UTS of the specimen, and point D represents the fracture strain. The joint strength for the weld in all conditions showed trends similar to the hardness results. Reduced mechanical property degradation in 300 rpm/6 ipm for both AW and PWHT conditions is due to the higher traverse speed, resulting in a colder run. JE of 300 rpm/6 ipm (75% of base YS) was 7-8% higher than other welds in the AW condition, as shown in Table 5.3.
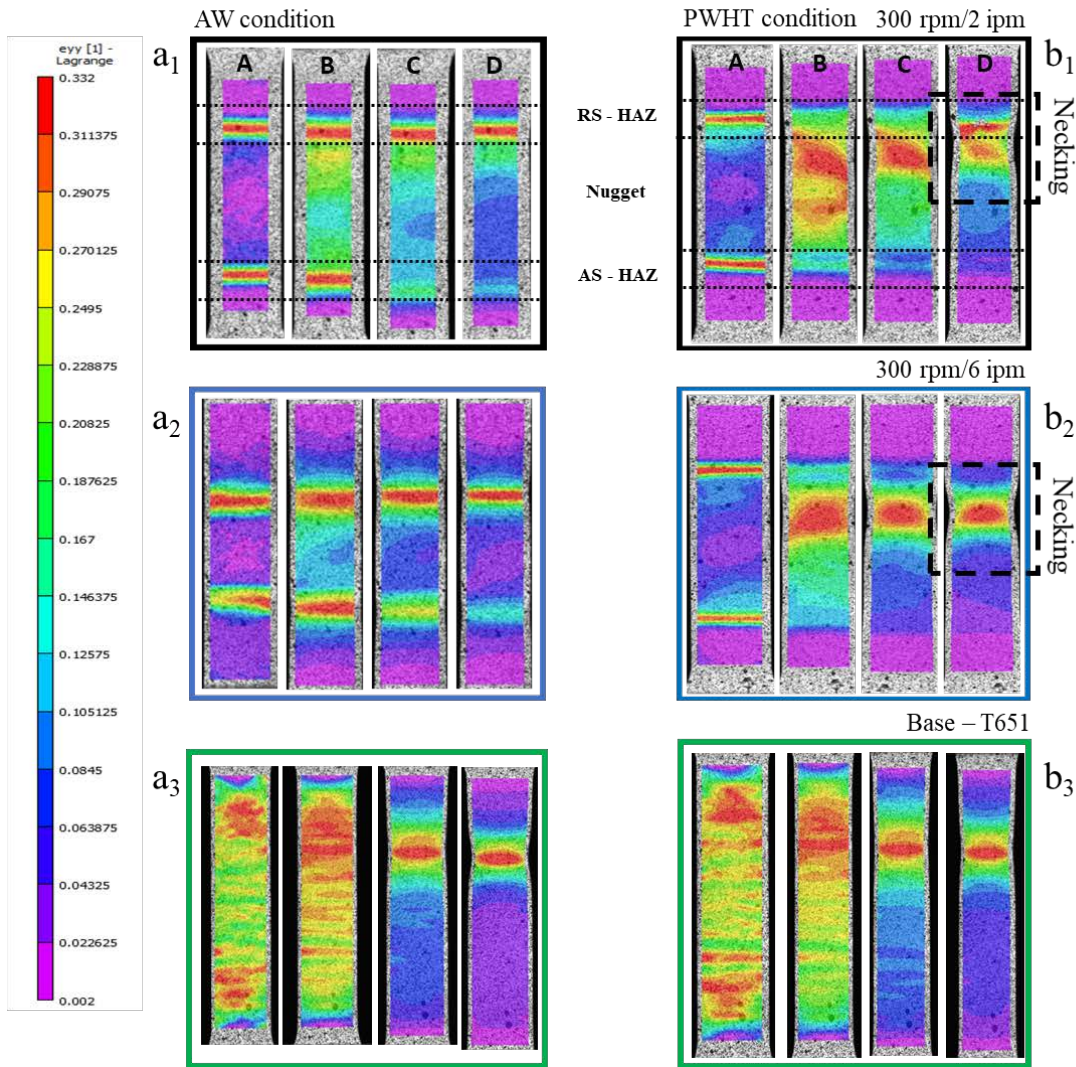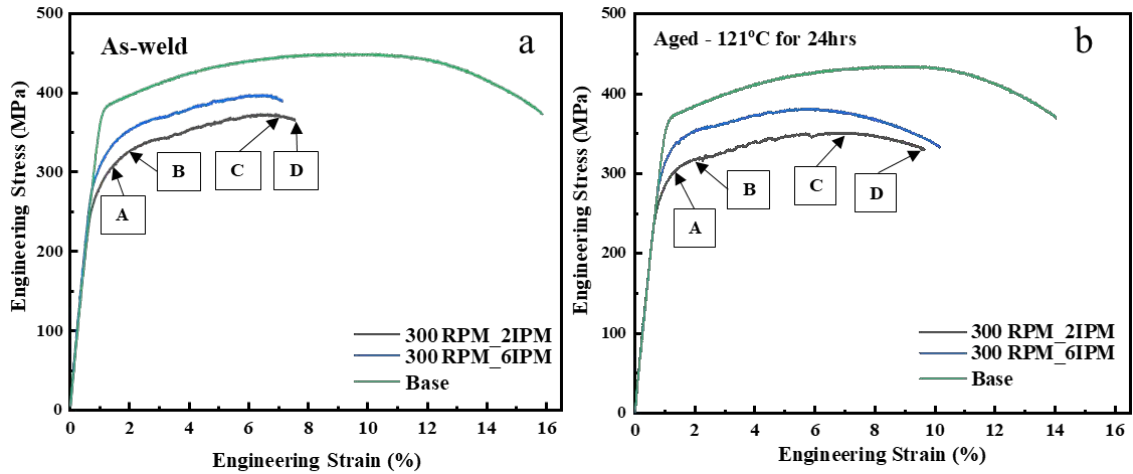
Figure 5.4: Uniaxial tensile testing results of (a) AW (b) PWHT at 121°C for 24hrs conditions compared to BM. Color contour maps of e_{yy} obtained from DIC for (a_1) 300 rpm/2 ipm, (a_2) 300 rpm/6 ipm, (a_3) BM in AW condition, and (b_1-b_3) corresponding PWHT conditions.

PWHT resulted in improved strength levels of both welds. The 300 rpm/6 ipm condition showed 86% JE after being subjected to PWHT compared to 74% YS-based JE for the 300 rpm/2 ipm condition. Elongation to failure of welded joints of 7xxx alloys is usually lower than the ductility of the BM. This is due to severe strain localization occurring in the gauge length of the tensile sample during the tension test [2,13].

The color contour maps of axial strain (e_{yy}), obtained with DIC imaging, in Figure 5.4 represent strain localization due to the response of the composite microstructure within the gauge length consisting of WN, HAZ, and BM of the tensile test. Figure 5.4(a_1-a_3) represents 300 rpm/2 ipm and 300 rpm/6 ipm in the AW condition as compared to the BM, showing that the deformation during a tensile test quickly localizes at the weakest region, i.e., HAZ of both the advancing and retreating sides (points A and B), and the extent of strain localization is approximately equal in both HAZs. With further deformation, the strain localization intensifies in the HAZ region of the retreating side (point C), followed by fracture (point D). The BM in Figure 5.4(a_3) has uniform strain distribution along the gauge length until localized necking initiates, resulting in non-uniform elongation and subsequent failure. Note that the contour maps in Figure 5.4(b_3) look similar to maps in Figure 5.4(a_3) due to similar mechanical behavior in the BM. However, the macro-deformation response of welded samples after PWHT showed a rather distinct response compared to the AW samples. During the initial deformation stage, minor strain localization was observed at both HAZs; the width of the strain localization band became much narrower (Figure 5.4(b_1-b_2)) as compared to AW samples (Figure 5.4(a_1-a_2)). The localized bands at the retreating side of the HAZ extend to the WN after yielding, and the deformation became uniform in the WN and HAZ with signs of strain localization. Also, PWHT at 121°C decreased the difference in hardness of the weakest zone and BM and improved elongation to failure compared to AW and PWHT conditions.

Point D in images of Figure 5.4 is taken just before the failure of AW and PWHT samples which indicates a difference in non-uniform elongation after reaching the UTS. Due to severe strain localization at the HAZ in AW samples in all conditions, necking was insignificant as the failure occurred precisely at the HAZ location on the weld's retreating side. However, in PWHT samples, the bold black dotted box in Figure 5.4(b_1-b_2) necking was appreciable due to more uniform deformation in the HAZ and WN due to changes in precipitate morphology.

The weld joints are heterogeneous, with different zones comprised of various microstructures. Thus, it is expected that the weld zones will show different mechanical properties, as expected from the microhardness results. Using the VIC-2D software, we captured the strain maps with the digital images at different stages of tensile strength, as mentioned previously, shown in Figure 5.4. In correlation to the DIC images represented in Figure 5.4, strain distribution along the centerline of the gauge section for points A to D was captured and shown in Figure 5.5. The plastic deformation and extension of the plastic region for the FSW joints were investigated. The strain distribution across the weld nugget and HAZs in as-welded conditions in Figure 5.5 exhibited differences in strength due to differences in grain size and precipitate size and distribution due to exposure to different temperatures for varying times. However, WN resists deformation more than the HAZ. This was reflected in the strain results shown in Figure 5.5 (a, b), where the lower strength HAZ (i.e., retreating side HAZ region) is locally elongated to high strain levels (over 29% and 35% for 300 rpm/ 2 ipm and 300 rpm/6 ipm run, respectively), eventually resulting in necking and fracture. On the other hand, the WN strain in both the weld runs does not reach the failure strain, as considerable additional ductility is available in the WN based on the uniaxial test results due to the equiaxed grain structure. The 7.3% and 7.6 % strain to failure reported in Table 5.3 is an average strain over the length included with the strain gauge, which

includes different weld zones. The soft, ductile HAZ corresponds to a short gauge length, as identified in the red dotted line in Figure 5.5. Thus, the measure of ductility across the weld reflects variation in YS of different HAZs.

Table 5.3: Tensile testing results for both AW and PWHT conditions of Al 7017-T651.

Sample	AW				PWHT - 121°C for 24hrs			
	YS	UTS	Nominal El.	JE	YS	UTS	Nominal El.	JE
	(MPa)	(MPa)	(%)	(%)	(MPa)	(MPa)	(%)	(%)
300 rpm/2 ipm	264 ± 8	371 ± 8	7.6 ± 0.4	68	275 ± 1	351 ± 1	10.1 ± 0.1	74
300 rpm/6 ipm	287 ± 3	396 ± 3	7.3 ± 0.1	75	321 ± 9	381 ± 2	10.8 ± 0.7	86
BM – T651	384 ± 1	447 ± 1	15.8 ± 0.7	-	371 ± 4	434 ± 8	15.1 ± 0.3	-
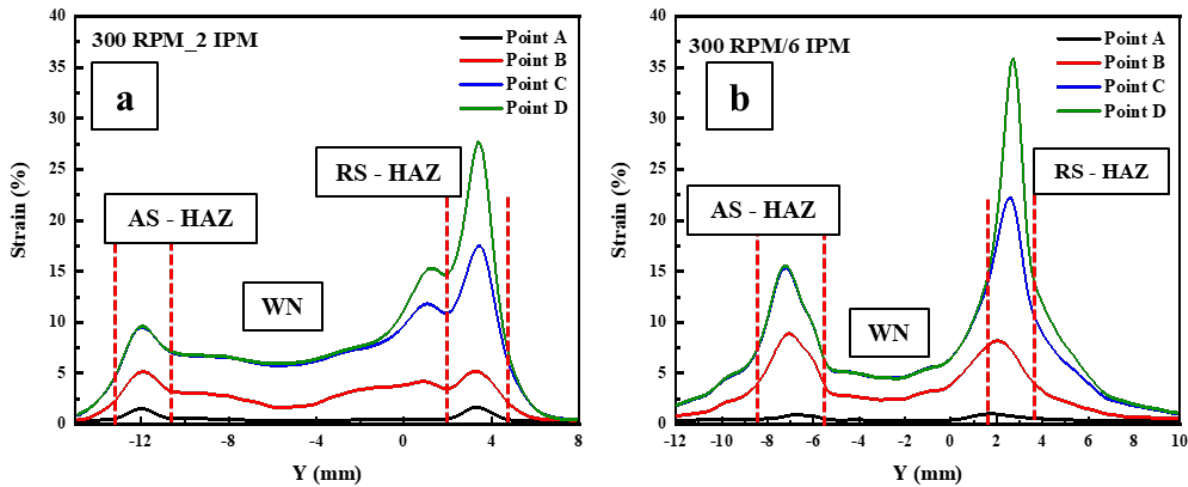
Figure 5.5: Local strain profile along the center of the samples at various strains of as-welded (a) 300 rpm/2 ipm and (b) 300rpm/ 6 ipm.

5.4.3   Corrosion

The cyclic polarization behavior of BM and FSW samples in all conditions in 3.5 wt.% NaCl solution is illustrated in Figure 6. The corrosion potential (E_{corr}) and corrosion current density (i_{corr}) values were determined from the respective polarization curves using the Tafel extrapolation method, as shown in Figure 6(a). Also, the mean values of pitting potentials (E_{pit}) and re-passivation potentials (E_{rp}) are presented in Table 5.4. Figure 6(a) shows that all samples exhibited

a classical passive behavior with current density, independent of applied potential until E_{pit}. After this passive region, the current density was raised abruptly due to stable pit growth and pit propagation until reaching a certain value [25]. Alternatively, it is known that the potential where the reverse cycle curve intersects the forward cycle is defined as E_{rp}. It is well demonstrated that the higher the value of E_{pit}, the more complex the pit formation is. Also, nobler E_{rp} to E_{corr} indicates that the material's resistance to pit growth is superior [26].

The hysteresis loops were revealed in the polarization curves in Figure 5.6, evidencing the nucleation and growth of pitting corrosion in the samples tested in 3.5 wt.% NaCl solution. Although E_{corr} for all samples was close to each other, the E_{pit} of the BM was significantly nobler than that of the AW samples in Figure 5.6(b, c). In addition, the E_{rp} of AW samples was also lower than that of the BM. Elatharasan et al. [27] demonstrated the corrosion behavior of the nugget of Al 7075 and reported that the nugget was more susceptible to pitting attributed to the presence of Al-Cu-Zn-Fe precipitates, which act as cathodic sites with respect to the Al matrix. Also, it could be easily seen that *the susceptibility of welded material to pitting corrosion was decreased by increasing the traverse speed*. However, the E_{rp} of AW samples increased slightly with the traverse speed (as presented in Figure 5.6 and Table 5.4). These results can be explained according to the grain size and the extent of precipitate phases obtained during FSW. Compared with the BM and the samples processed at traverse speeds of 2 ipm and 6 ipm, the one processed at 6 ipm exhibited a better E_{rp}. As it is well known, the grain size is an essential factor influencing the passivation ability and the rapid formation of a solid and stable passive film on the surface of metals [28,29]. Thus, the lower E_{rp}, i.e., -0.958 V of the sample processed at 300 rpm/6 ipm compared to the BM (-0.805V), could be attributed to the presence of coarser-grained region; a higher corrosion resistance in NaCl electrolyte is observed as compared to the fine-grained region, which is

attributed to the presence of fewer corrosion sites in coarse-grained regions [30].
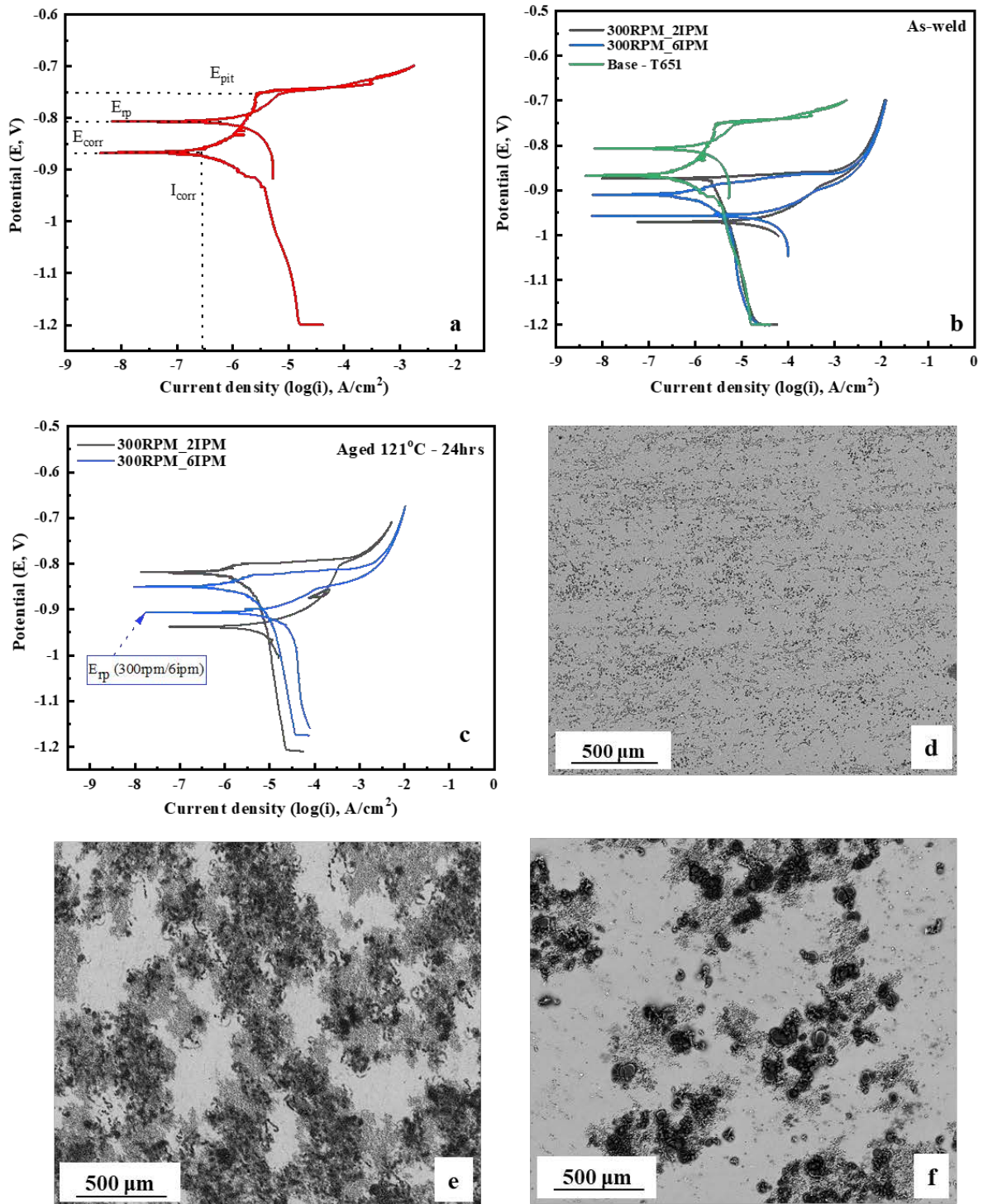
Figure 5.6: Cyclic potentiodynamic polarization curves (a) representative figure illustrating the electrochemical parameters, (b) AW-WN in comparison to BM, (c) PWHT-WN in 3.5 wt.% NaCl solution and SEM images of post-corrosion (d) BM, (e) 300rpm/ 2ipm and (f) 300rpm/ 6ipm.

Table 5.4: Electrochemical parameters obtained from cyclic polarization measurements in 3.5 wt.% NaCl

Sample	I_{corr} (A/cm^2)	E_{corr} (V)	E_{rp} (V)	E_{pit} (V)
300 rpm/2 ipm (AW)	-5.987	-0.875	-0.970	-0.860
300 rpm/6 ipm (AW)	-6.559	-0.910	-0.958	-0.863
300 rpm/2 ipm (PWHT)	-6.159	-0.818	-0.938	-0.803
300 rpm/6 ipm (PWHT)	-6.215	-0.851	-0.909	-0.859
BM – T651	-6.793	-0.866	-0.805	-0.754

Thus, the higher the traverse speed, the higher the corrosion resistance. PWHT of welds leads to grains coarsening, resulting in a shift in E_{rp} to more noble potential, as seen in Figure 5.6(c) and noted in Table 5.4. The SEM images captured post corrosion test in Figure 5.6(d-f) clearly show the effect of traverse speed compared to the BM. Figure 5.6(e) showed extensive pitting instigated in the slower run, and the image in Figure 5.6(f) far fewer corrosion pits post corrosion attack.

5.4.4   Microstructural Evolution

5.4.4.1   Precipitation Kinetics via TEM

The primary strengthening precipitates on lattice defect structures and grain boundaries in the 7xxx Al alloys are η´ (Mg(Zn,Cu)$_2$) formed within the matrix and η (MgZn$_2$) formed in the grain interior and grain boundaries [9,13,31,32]. Traditional TEM diffraction studies were carried out to look for precipitation evolution and its volume fraction after FSW and PWHT of Al 7017-T651. Figure 5.7(a) gives a low magnification bright field (BF) image along the [011] zone axis (in Figure 5.7(b)) of the TEM foil. Figure 5.7(c) has a magnified weak beam dark field (WBDF) image with g = 200, showing homogeneously distributed precipitates of size less than ~20 nm in the grain interior.

Figure 5.8 shows TEM images of a sample obtained from the WN of 300 rpm/6 ipm and 300 rpm/2 ipm run in the AW condition. During FSW, although high temperature and processing

strain dissolve the existing precipitates to form a supersaturated solid solution in the WN, the cooling rate behind the tool can significantly influence the post-weld microstructure.
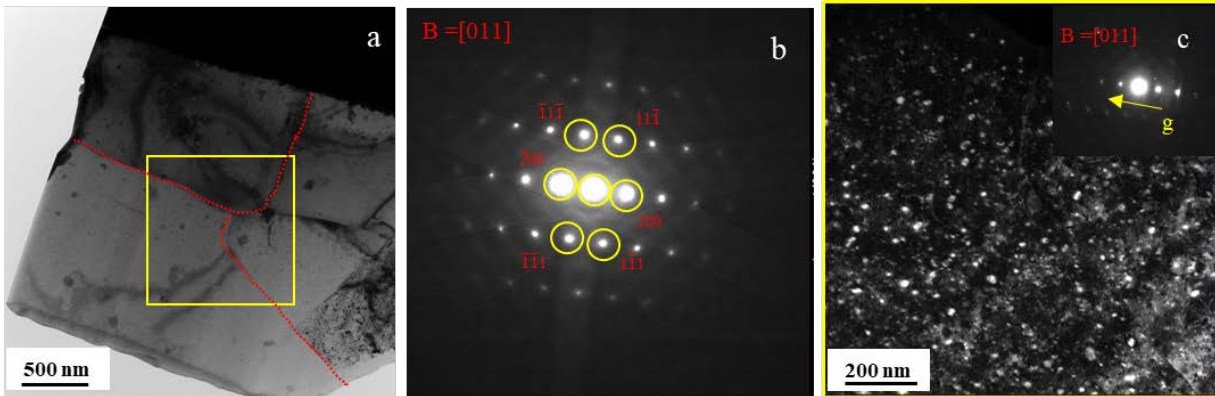
Figure 5.7: TEM imaging of BM-T651 (a) low magnification BF, B=[011], (b) diffraction pattern from [110] zone axis, and (c) WBDF from with g = 2̄00 in (b).

The SEM image of WN of 300 rpm/6 ipm in Figure 5.8(a) indicates a fully recrystallized, near fine equiaxed grain structure with a grain size of ~6μm. The low magnification TEM image of WN for 300 rpm/6 ipm was represented in Figure 5.8(b). The BF and WBDF images in Figure 5.8(b_1-b_4) display the bi-modal precipitation size distribution. Precipitation was observed at the sub-grain boundary in the BF (Figure 5.8(b_1)). A more extensive range of precipitates ranging from 5-10 nm to 20-30 nm was observed in the WBDF image in Figure 5.8(b_3). Figure 5.8(c and d) represents the SEM and TEM images of WN of 300 rpm/ 2ipm run. The more refined equiaxed grain structure (~ 4μm), i.e., the reduced aspect ratio, was observed in 300 rpm/2 ipm than the WN in 300 rpm/6 ipm. The BF and WBDF images show the precipitation distribution in the hotter run (300 rpm/2 ipm) in Figure 5.8(d_1-d_4). The volume fraction of precipitates is smaller than in a higher traverse speed run in a slower run. The higher temperature was observed due to the slower traverse speed, allowing more precipitate dissolution than the faster traverse speed run. Note that the precipitate size and their volume fraction were more significant in WN (in Figure 5.8) than BM, as observed in Figure 5.7.
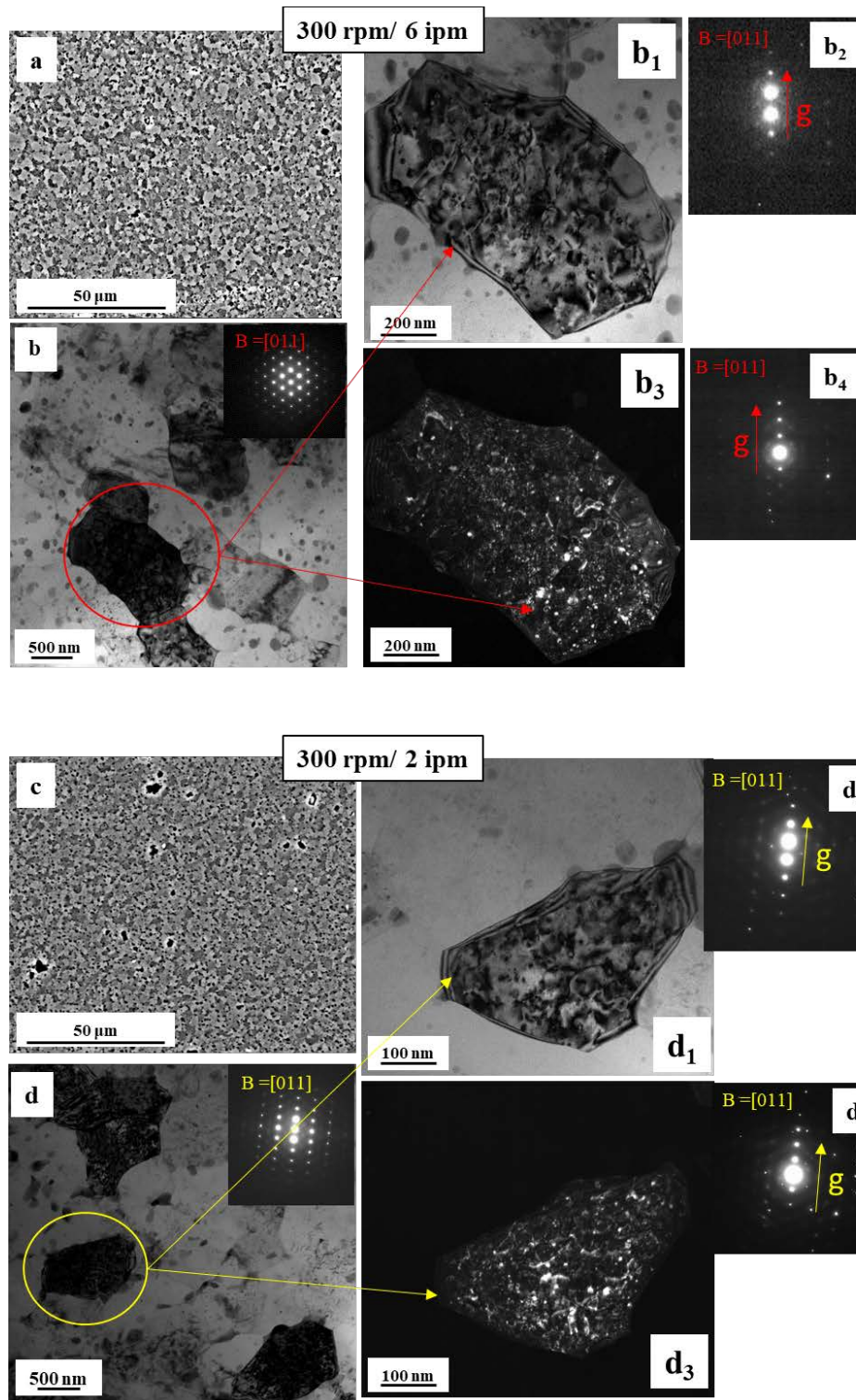
Figure 5.8: SEM & TEM imaging for WN in AW condition (a) Low magnification SEM image of WN – 300rpm/6ipm, (b) BF showing the precipitates of different contrast in a matrix along with grain size in 300 rpm/6 ipm, B = [011], g = 200, (b₁, b₃) high magnification BF and WBDF images respectively, B=[011], g = 200 in (b₂) and (b₄) and (c) low magnification SEM of WN-300rpm/2ipm, (d) low magnification BF image for 300 rpm/2 ipm, B = [011], g = 200, (d₁, d₃) high magnification BF and WBDF images respectively, B = [011], g = 200 in (d₂) and (d₄)

A comparison of TEM micrographs from the WN and BM can be used to understand the effect of FSW. Figure 5.9 shows precipitate evolution in the HAZ region in the AW condition for both runs. When compared to the BM precipitate size in Figure 5.7, the precipitates in the HAZ have coarsened quite significantly. However, it can be observed from Figure 5.9 that the grains in the HAZ region of the slower run (300 rpm/2 ipm) have coarser grains due to the high temperature generated during the FSW process compared to the HAZ region of the colder run.
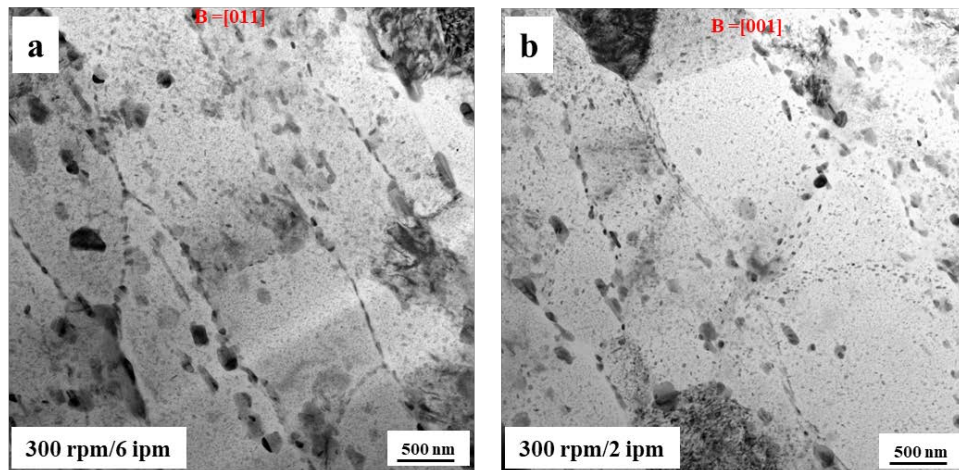
Figure 5.9: TEM imaging of HAZ region for AW conditions (a) BF image of HAZ region of 300 rpm/6 ipm run, B=[011] and (b) BF image of HAZ region of 300 rpm/2 ipm run, B=[001].

However, the width and length of the precipitates observed are in the range of ~15-50 nm and ~50-150 nm in the HAZ region of 300 rpm/6 ipm in Figure 5.9(a). The other observation was that the higher volume fraction of coarsened precipitates were observed in the colder run, and the reason for it would be insufficient time for the precipitates to dissolve when subjected to the peak temperature during FSW. In Figure 5.9 (b), a combination of both fine and coarse precipitates were observed in the HAZ region of 300 rpm/2 ipm run. The slow speed and high temperature (~371°C) would provide sufficient time for the precipitates to dissolve some fine precipitates and simultaneously allow the coarsening of precipitates; with these welding parameters, a reduced volume fraction of coarser precipitates were observed. Thus, the dissolution of precipitates caused

the low hardness values of ~109 HV in the HAZ region of 300 rpm/ 2ipm compared to the hardness

value (119 $\pm$ 2 HV) of the HAZ region of 300 rpm/6 ipm. Sullivan and Robinson [6] also reported

severe coarsening of grain boundary (GB) and intra-grain precipitates.
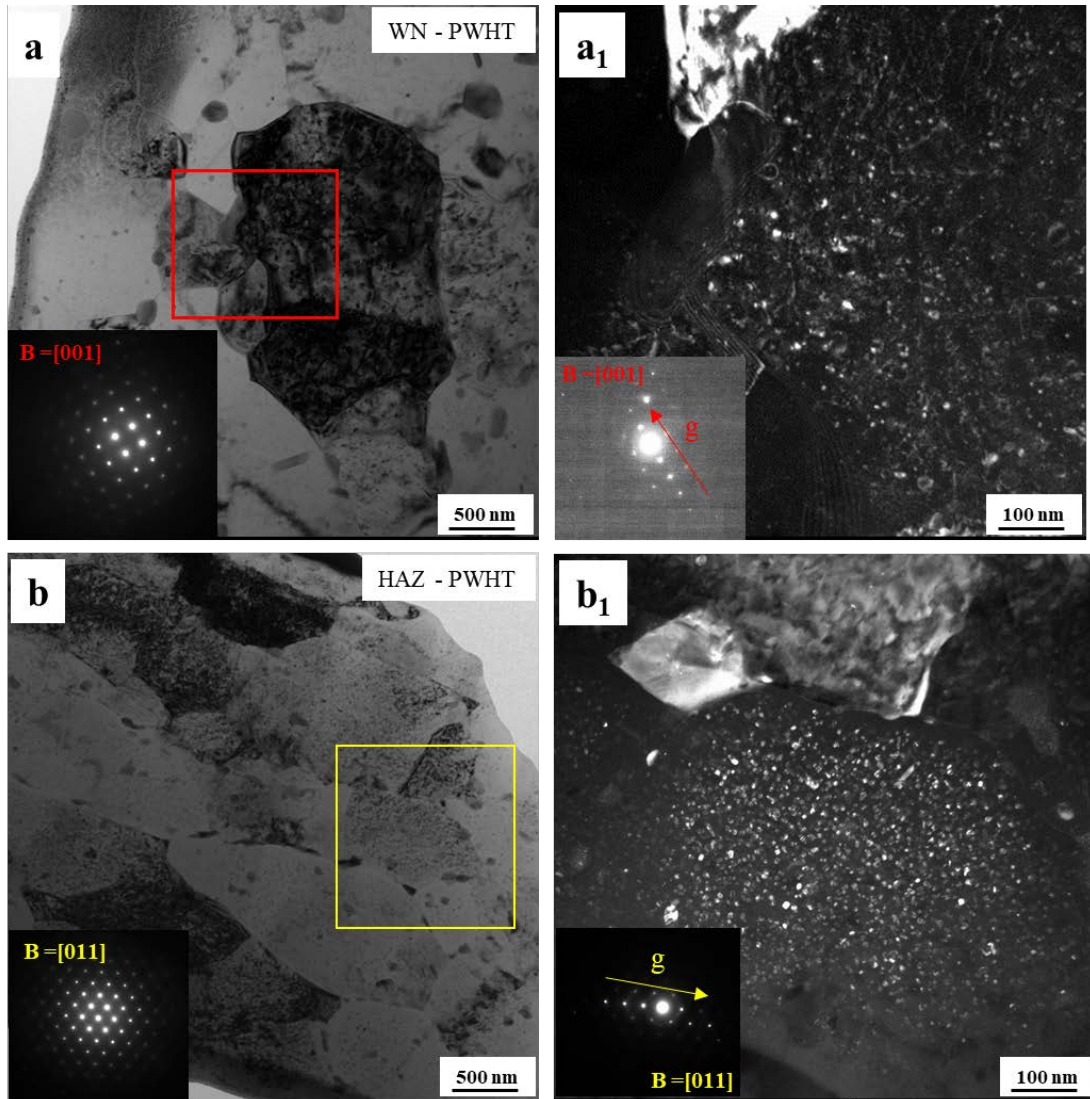
Figure 5.10: TEM images of PWHT (a) low magnification BF image of WN, B = [001], g = 220 and (a1) high magnification WBDF image of PWHTed WN with g = 220 in (a); (b) low magnification BF image of PWHT HAZ region, B = [011], g = 200 and (b1) high magnificati magnification WBDF image of HAZ region with g = 200 in (b).

The effect of PWHT on weld (300 rpm/6 ipm) is captured in Figure 5.10 to understand the

kinetics, volume fraction, and size of precipitates evolving in different weld regions. PWHT

samples from WN given in Figure 5.10(a) indicated coarsening of GB and matrix precipitates with

a grain size with an aspect ratio of 1.3. The micrograph in Figure 5.10(a) represents a low magnification weak beam of the PWHT WN in which the grain is along the [001] zone axis. The high magnification BF in Figure 5.10(a_1) shows a significant change in precipitate evolution after aging. More homogenously distributed precipitates were observed. Also, the volume fraction of precipitates had reduced compared to the WN in the AW condition. Figures 5.10(b) and (b_1) showed the effect of PWHT on the HAZ where the coarsening of the preexisting precipitate. DSC analysis was used to further validate TEM results and mechanical behavior, thus relating the corrosion behavior for selected conditions.

5.4.4.2   Validation of Precipitation Evolution via DSC

DSC has been used extensively to study the precipitation behavior of precipitation strengthened Al alloys [8]. DSC experiments were conducted to study the effect of FSW and PWHT on the precipitation and dissolution of various phases in the welds for the current study. The amplitude of a peak and the area under a peak in a DSC plot relates to the propensity of precipitation and its volume fraction [33,34]. For the same alloy composition and heating rate during the DSC experiment, peak temperature can be related to precipitate size and stability. Figure 5.11(a) shows DSC results for samples from the WN in AW condition. For comparison, the DSC results of the BM are also shown in Figure 5.11(a,b). In Figure 5.11, the prominent exothermic peak is due to the formation of η´ precipitates, and the endothermic peak spanning approximately from 330°C to 400°C is the dissolution of η´ [34]. In Figure 5.11(a), the exothermic peak for 300 rpm/2 ipm WN compared to that of 300 rpm/6 ipm WN shows that dissolution of precipitates during welding is more efficient in 300 rpm/2 ipm as compared to 300 rpm/6 ipm and can be attributed to higher heat generated in the former run due to slower traverse speed. For AW samples from the HAZ region in Figure 5.11(c), observation of a smaller exothermic peak and the larger

endothermic peak as compared to peaks in the WN for AW samples point to the coarsening of η′ precipitates in HAZ. The exothermic peak, i.e., precipitate formation peak for the sample from the HAZ of 300 rpm/6 ipm, is smaller than the HAZ of 300 rpm/2 ipm. Following the temperature data and mechanical test results, the extent of coarsening of η′ precipitate proved to be significantly less in 300 rpm/6 ipm than the slower run (300 rpm/2 ipm). The TEM results for the as-welded HAZ region in Figure 5.9 suggested that the coarsening of precipitates was observed in the colder run, and partial dissolution of precipitates was observed in the hotter run, lowering more solute present in the matrix. Also, absence of GP zones in the HAZ region of the hotter run indicates the dissolution of smaller η′ precipitates due to the higher temperature generated during the slower traverse speed weld.
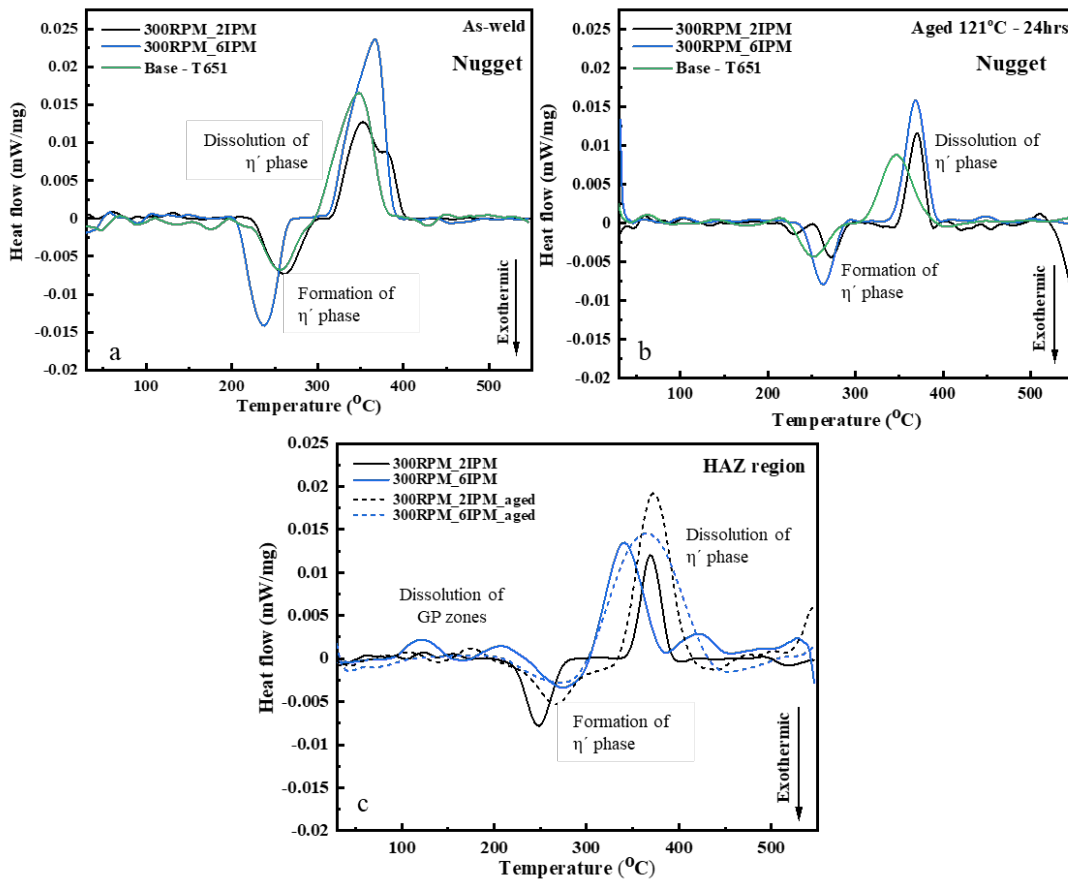
Figure 5.11: DSC results of (a) samples from WN in AW condition, (b) samples from WN in PWHT condition, and (c) samples from HAZ in both AW and PWHT conditions.

Figure 5.11(b) shows the DSC results of samples taken from the WN in PWHT conditions. Precipitation of the η′ phase was observed in all conditions. Interestingly, for PWHT samples, the exothermic peak reduces with respect to the area under the curve. Change in the area under the curve for the exothermic peak in PWHT samples compared to AW samples is due to the coarsening of η′ precipitates during PWHT. Referring to Figure 5.11(c) for PWHT, the temperature in the HAZ of 300 rpm/6 ipm was not sufficiently high to dissolve all pre-existing precipitates, and very few solutes are available to form new precipitates. PWHT further reduces the exothermic peak, attributed to the coarsening of precipitates. Thus, the change in the volume fraction of precipitates in the HAZ is much smaller than samples from the nugget, indicating the only coarsening of precipitates occurs in the HAZ region, whereas precipitation and growth of precipitates occur in the WN when subjected to PWHT.

5.5   Discussion

The DSC and TEM results indicated that FSW parameters determine the amount of dissolution, re-precipitation, and coarsening in different zones in the weld. In the WN, the dissolution of strengthening precipitates significantly contributes to the drop in strength. PWHT of the WN improves properties by either forming GP zones or η′ precipitates from the solute in solution. However, the heat gradient in the WN affects the level of re-precipitation. In the case of the HAZ, precipitates dissolve and coarsen the η′ phase. The degree of dissolution or coarsening depends on the amount of heat generated by the tool and the amount of time associated with the temperature rise. With an increase in temperature in the HAZ, coarsening occurs. A higher temperature leads to greater dissolution of both smaller and medium-sized precipitates. For coarsening to occur, a temperature rise must occur for a prolonged period. This would be the case for slow traverse speed welds.

In this work, results validate the concept of dissolution and coarsening of precipitates in the WN and HAZ for the slow traverse speed weld due to higher peak temperature. The hardness profile and tensile test results indicated better properties for the colder run (300 rpm/6 ipm) in the WN and HAZ than the hotter run (300 rpm/2 ipm). Higher hardness and smaller width of the HAZ in 300 rpm/6 ipm run results from the lower temperature in the HAZ. Also, due to higher traverse speed, the HAZ of 300 rpm/6 ipm experienced peak temperature for less time, resulting in less coarsening of the precipitates in the HAZ. During the tensile test, loss of strength is mainly due to partial precipitate dissolution in HAZ, which causes severe precipitate coarsening and inefficient reprecipitation of fine strengthening precipitates. Thus, HAZ deforms first, resulting in strain localization and subsequent localized weld failure. Mishra and Komarasamy [35] have suggested that the location of the lowest yield strength across the weld in 7XXX alloys is typically the HAZ. Thus, better mechanical properties with higher JE depend on the FSW parameter selection process, i.e., higher traverse speed reduces the HAZ size (see mechanical property trends in Table 5.3). The 54% YS-based JE for Al 7075-T6 (in wt.% 5.6Zn-2.5Mg-1.6Cu) was reported by Mahoney [36] for as-welded and PWHTed samples; however, the alloy studied here showed 75% YS-based JE for Al 7017-T6 (in wt% 4.95Zn-2.22Mg-0.2Cu) for the as-welded condition and improvement of JE by 11% (86% JE) when subjected to PWHT for the faster run. Thus, a low amount of alloying element addition did not affect the properties, with conditions the suitable weld parameters are selected. The effect of process parameters caused the change in grain size due to the combined influence of temperature and strain during FSW, directly impacting the corrosion behavior of the weld. A slower traverse speed induces a more significant amount of deformation at any given location along the weld. This results in a smaller grain size for the 300 rpm/ 2 ipm weld and more corrosion sites than 300 rpm/ 6 ipm and BM. Hence, the higher traverse speed welds aid in the

formation of strengthening precipitate η′ in both WN and HAZ, which allows improvement in weld strength and corrosion resistance after heat treatment.

The effect of heat treatment was evident from the mechanical and corrosion tests. However, a significant improvement was seen in the hardness and tensile values of the faster run when subjected to PWHT. The reason for improved properties was explained with the help of DSC in Figure 5.11(b) results. Post heat-treatment, we see that nucleation of strengthening precipitates dominated over the coarsening of precipitates in the faster run compared to the slower run, where coarsening or precipitates dominated over the nucleation of precipitates. Thus, allowing improvement in strength and corrosion resistance.

5.6   Conclusion

A systematic experimental evaluation, including mechanical and corrosion testing, DSC analysis, and electron microscopy, was conducted to study the effect of weld parameters on as-welded and aged FSWed 7017-T651 alloy. The selection of welding parameters and thermal management scheme during and after FSW of precipitation strengthened Al alloys can significantly influence the final microstructure and properties. Higher tool traverse speed leads to a lower temperature profile within the WN, thus resulting in a narrower HAZ, which eventually improved the JE of the weld (YS-based JE -75 %) compared to the hotter run with a wider HAZ region (YS based JE is 68%). Also, the lower peak temperature in 300rpm/ 6ipm allowed less dissolution of strengthening precipitates and coarser grain (~6μm) in comparison to the slower run. Therefore, higher strength and better corrosion resistance were observed. When subjected to PWHT, the colder run showed significant improvement in mechanical and corrosion properties. In addition, improved JE was observed in 300 rpm/ 6ipm (YS-based JE 86%); less time was spent at the peak temperature, and the presence of solute in the matrix allowed the nucleation and growth

of strengthening precipitates to occur when subjected to PWHT at 121°C for 24 hours. Thus, the

300 rpm/ 6ipm is an effective welding parameter with appropriate properties.

5.7   References

[1]   T. Dursun, C. Soutis, Recent developments in advanced aircraft aluminium alloys, Mater. Des. 56 (2013) 862–871.

[2]   R.S. Mishra, Z.Y. Ma, Friction stir welding and processing, Mater. Sci. Eng. R Reports. 50 (2005) 1–78.

[3]   R.S. Mishra, P.S. De, N. Kumar, Friction stir welding and processing: Science and engineering, Frict. Stir Weld. Process. Sci. Eng. 9783319070 (2014) 1–338.

[4]   Wayne M. Thomas, E.D. Nicholas, J.C. Needham, M.G. Murch, P. Temple-Smith, C.J. Dawes, Friction welding, 5,460,317, 1995.

[5]   M.W. Mahoney, Rajiv.S.Mishra, Friction stir welding and processing, ASM Int. (2007) 360.

[6]   A. Sullivan, J.D. Robson, Microstructural properties of friction stir welded and post-weld heat-treated 7449 aluminium alloy thick plate, Mater. Sci. Eng. A. 478 (2007) 351–360.

[7]   J.Q. Su, T.W. Nelson, C.J. Sterling, Microstructure evolution during FSW/FSP of high strength aluminum alloys, Mater. Sci. Eng. A. 405 (2005) 277–286.

[8]   M.J. Starink, Analysis of aluminium based alloys by calorimetry: quantitative analysis of reactions and reaction kinetics, Int. Mater. Rev. 49 (2013) 191–226.

[9]   L.K. Berg, J. Gjoønnes, V. Hansen, X.Z. Li, M. Knutson-Wedel, G. Waterloo, D. Schryvers, L.R. Wallenberg, GP-zones in Al–Zn–Mg alloys and their role in artificial aging, Acta Mater. 49 (2001) 3443–3451.

[10]   G. Sha, A. Cerezo, Early-stage precipitation in Al–Zn–Mg–Cu alloy (7050), Acta Mater. 52 (2004) 4503–4516.

[11]   G. Sha, Y.B. Wang, X.Z. Liao, Z.C. Duan, S.P. Ringer, T.G. Langdon, Influence of equal-channel angular pressing on precipitation in an Al–Zn–Mg–Cu alloy, Acta Mater. 57 (2009) 3123–3132.

[12]   T. Engdahl, V. Hansen, P.J. Warren, K. Stiller, Investigation of fine scale precipitates in Al–Zn–Mg alloys after various heat treatments, Mater. Sci. Eng. A. 327 (2002) 59–64.

[13]   A.P. Reynolds, W. Tang, Z. Khandkar, J.A. Khan, K. Lindner, Relationships between weld parameters, hardness distribution and temperature history in alloy 7050 friction stir welds, Sci. Technol. Weld. Join. 10 (2005) 190–199.

[14] N. Kamp, A. Sullivan, J.D. Robson, Modelling of friction stir welding of 7xxx aluminium alloys, Mater. Sci. Eng. A. 466 (2007) 246–255.

[15] C.B. Fuller, M.W. Mahoney, M. Calabrese, L. Micona, Evolution of microstructure and mechanical properties in naturally aged 7050 and 7075 Al friction stir welds, Mater. Sci. Eng. A. 527 (2010) 2233–2240.

[16] N. Kamp, A. Sullivan, R. Tomasi, J.D. Robson, Modelling of heterogeneous precipitate distribution evolution during friction stir welding process, Acta Mater. 54 (2006) 2003–2014.

[17] R. Brown, W. Tang, A.P. Reynolds, Multi-pass friction stir welding in alloy 7050-T7451: Effects on weld response variables and on weld properties, Mater. Sci. Eng. A. 513–514 (2009) 115–121.

[18] J.Q. Su, T.W. Nelson, R. Mishra, M. Mahoney, Microstructural investigation of friction stir welded 7050-T651 aluminium, Acta Mater. 51 (2003) 713–729.

[19] C.G. Rhodes, M.W. Mahoney, W.H. Bingel, M. Calabrese, Fine-grain evolution in friction-stir processed 7050 aluminum, Scr. Mater. 48 (2003) 1451–1455.

[20] M. Dumont, A. Steuwer, A. Deschamps, M. Peel, P.J. Withers, Microstructure mapping in friction stir welds of 7449 aluminium alloy using SAXS, Acta Mater. 54 (2006) 4793–4801.

[21] K.S.R. and K.P. Rao, Pitting corrosion of heat-treatable aluminium alloys and welds: A review, Trans. Indian Inst. Met. 57 (2004) 593–610.

[22] J.B. Lumsden, M.W. Mahoney, G. Pollock, C.G. Rhodes, Intergranular Corrosion Following Friction Stir Welding of Aluminum Alloy 7075-T651, Corrosion. 55 (1999) NACE-99121127.

[23] C.S. Paglia, M.C. Carroll, B.. Pitts, T. Reynolds, R.G. Buchheit, Strength, Corrosion and Environmentally Assisted Cracking of a 7075-T6 Friction Stir Weld, Mater. Sci. Forum. 396–402 (2002) 1677–1684.

[24] K. V. Jata, K.K. Sankaran, J.J. Ruschau, Friction-stir welding effects on microstructure and fatigue of aluminum alloy 7050-T7451, Metall. Mater. Trans. A. 31A (2000) 2181–2192.

[25] M.A. Amin, A newly synthesized glycine derivative to control uniform and pitting corrosion processes of Al induced by SCN− anions – Chemical, electrochemical and morphological studies, Corros. Sci. 52 (2010) 3243–3257.

[26] S.J. Kalita, Microstructure and corrosion properties of diode laser melted friction stir weld of aluminum alloy 2024 T351, Appl. Surf. Sci. 257 (2011) 3985–3997.

[27] G. Elatharasan, Corrosion Analysis of Friction Stir-welded AA 7075 Aluminium Alloy, J. Mech. Eng. 60 (2014) 29–34.

[28] A. Balyanov, J. Kutnyakova, N.A. Amirkhanova, V. V. Stolyarov, R.Z. Valiev, X.Z. Liao, Y.H. Zhao, Y.B. Jiang, H.F. Xu, T.C. Lowe, Y.T. Zhu, Corrosion resistance of ultra fine-grained Ti, Scr. Mater. 51 (2004) 225–229.

[29] G.R. Argade, S.K. Panigrahi, R.S. Mishra, Effects of grain size on the corrosion resistance of wrought magnesium alloys containing neodymium, Corros. Sci. 58 (2012) 145–151.

[30] W.R. Osório, C.M. Freire, A. Garcia, The role of macrostructural morphology and grain size on the corrosion resistance of Zn and Al castings, Mater. Sci. Eng. A. 402 (2005) 22–32.

[31] A. Deschamps, F. Livet, Y. Bréchet, Influence of predeformation on ageing in an Al–Zn–Mg alloy—I. Microstructure evolution and mechanical properties, Acta Mater. 47 (1998) 281–292.

[32] J. Buha, R.N. Lumley, A.G. Crosky, Secondary ageing in an aluminium alloy 7050, Mater. Sci. Eng. A. 492 (2008) 1–10.

[33] X.M. Li, M.J. Starink, DSC Study on Phase Transitions and Their Correlation with Properties of Overaged Al-Zn-Mg-Cu Alloys, J. Mater. Eng. Perform. 2011 216. 21 (2011) 977–984.

[34] L. X.-M., M.J. Starink, Effect of compositional variations on characteristics of coarse intermetallic particles in overaged 7000 aluminium alloys, Mater. Sci. Technol. 17 (2001) 1324–1328.

[35] M.K. R.S.Mishra, Friction Stir Welding of High Strength 7XXX Aluminum Alloys, 2016.

[36] M.W. Mahoney, C.G. Rhodes, J.G. Flintoff, R.A. Spurling, W.H. Bingel, Properties of friction-stir-welded 7075 T651 aluminum, Metall. Mater. Trans. A 1998 297. 29 (1998) 1955–1964. https://doi.org/10.1007/S11661-998-0021-5.

CHAPTER 6

CORRELATION BETWEEN MODELING AND EXPERIMENTAL CHARACTERIZATION

OF MICROSTRUCTURAL EVOLUTION OF AA 7017-T7 DURING FRICTION STIR

WELDING

6.1   Abstract

An interactive interface has been established between thermomechanical, microstructural, and property models, making the study of friction stir welded (FSW) AA 7017-T7 to understand the effect of different weld parameters to get appropriate mechanical properties entirely dependent on the evolution of strengthening precipitates. The thermal profile generated via COMSOL-Multiphysics in the thermal model shows the dependence of peak temperature observed during FSW on the welding parameters, and higher rotational speed resulted in higher peak temperature (~455°C) compared to the slower rotational rate weld. Using these temperature profiles, precipitation evolution was studied in nugget for different weld parameters and compared to the base material (BM) with the help of the KWN model via TC-Prisma. The microstructure model predicts the presence of η' and η in the base material (BM) and only η in the FSWed samples as high temperatures generated during the weld causes the dissolution of precipitates, which would result in lower strength of FSWed samples compared to BM. The property model comprised of four crucial strengthening mechanisms that assisted in calculating the yield strength (YS) for two different weld parameters (300rpm/4ipm and 600rpm/4ipm) compared to BM are 401MPa and 376MPa, and 403MPa, respectively. The effect of post-weld heat treatment (PWHT) was also studied to improve and achieve the desired weld properties by allowing the formation of strengthening precipitates. Finally, with the help of experiments, defect-free welds were characterized with the help of differential scanning calorimetry (DSC), transmission electron

microscopy (TEM), and mechanical tests to validate the modeling outputs.

6.2   Introduction

Due to its high strength-to-weight ratio and excellent processing performance, 7xxx alloys have been extensively used in the aerospace industry [1]. The fabrication of aluminum (Al) alloy parts and components widely uses welding technology. However, high-strength Al alloys such as AA 7017 are challenging to be joined via conventional fusion welding because of the thermal cracks and pores. Since its invention at The Welding Institute [2], FSW has proven to be a superior joining technique for precipitation-hardened aluminum alloys [3,4].

In the FSW, the rotating tool is plunged into the workpiece at a specified velocity, traversing along the abutting edge of the workpiece to generate a solid weld [5]. Heat is generated due to friction between the workpiece and rotating tool, as well as adiabatic heating of the material due to the plastic deformation of the material. The material softens at a higher temperature, facilitating material flow around the pin from front to back and consolidating during the traverse stage of welding. The synergistic action of temperature, strain, and strain rate changes the local weld microstructure, thus affecting the mechanical properties.

The strengthening precipitates in 7xxx alloys are well-established and coherent η´ precipitates is dominant [5]. The literature reveals the evolution of precipitation in the 7xxx series are in Table 6.1.

Table 6.1: Precipitation evolution in 7xxx alloys

Precipitates	Forming Temperature (°C)	Dissolving Temperature (°C)
GP Zones	25 - 50	90 – 120
η´	140 - 190	>190
η	215 - 250	>320
M-phase	350	>430

Various studies have reported experimental FSW of Al alloys [7–10]. However, studies on the simulation of FSW have not been reported extensively. Although the operation of FSW appears very simple, the physics involved is quite complex. Various modeling approaches have been utilized to elucidate the thermal profile, microstructural and material strength aspects during FSW separately, but no correlation between these models has been established.

Multiple researchers have modeled the thermal profile and material flow during FSW [6,11–14]. A study by Khandkar et al.[15] proposed a three-dimensional model based on experimentally measured torque distribution, considering the bottom heat transfer coefficient. However, these initial models ignored viscoplastic flow and convective heat transfer. Ulysse et al. [13] developed a three-dimensional viscoplastic model for FSW of Al alloys, which showed tool rotation rate and traverse speed effects on temperature and forces. Nandan et al. [11,14] reported temperature fields, cooling rates, and plastic flow fields using three-dimensional material flow and heat transfer during FSW of AA 6061.

Several authors have successfully modeled precipitation kinetics [16–20] for Al Alloys, and the most successful precipitation models are based on the Kampmann and Wanger numerical (KWN) approach [17], where they developed a numerical model for homogeneous precipitation. Deschamps et al. [19–21] developed numerous models for precipitate evolution in the 7xxx series when considering the KWN approach subjected to aging. Kamp et al. [22–24] proposed a numerical model to predict precipitate distribution during FSW of AA 7449 alloy. In addition, Schercliff et al. [25] developed a process model for age hardenable Al alloys based on classical kinetic theory and calibrated hardness data. Myhr and Grong et al. [18] model calculated the strength of the material but failed to predict the microstructure and precipitate evolution. To model

the strength of the weld for age hardenable alloys, a more detailed prediction of microstructure is required.

None of the above-mentioned works incorporated a direct relationship between the thermal model and the microstructural model to predict precipitation evolution and finally predict the weld properties. Thus, this work was designed to merge multiple aspects of FSW of Al alloys minimum input variables and reduce the Edisonian approach by increasing productivity via faster process development and is being referred as **"*Super-predictor"*** in this manuscript*.* The current simulation approach involved all possible aspects of the FSW process, which was not performed together before. We used three-dimensional heat transfer for FSW of AA7017 alloy to evaluate the tool rotation rate and traverse speed effect on the thermal profile. The microstructural model tracks the evolution of precipitates during welding. Using the thermal profile generated, precipitation evolution in nugget was modeled; finally, strength was predicted before and after FSW AA 7017 alloy. Additionally, the effect of PWHT on precipitation evolution was studied in the nugget to improve post-weld properties.

6.3   Materials and Experimental Methods

AA 7017-T7651 with composition Al-4.5Zn-2.5Mg-0.2Cu (wt%) was used for the Super-predictor simulation. Table 6.2 represents the FSW details used for thermal simulation using a steady-state Eulerian solution in COMSOL-Multiphysics developed by Schmidt et al. [26]. The simulations were performed for one tool but with different rotational rates and constant traverse speed, as mentioned in Table 6.2. The thickness of the plate used was 12 mm. The simulation was performed for the stirred zoned, i.e., nugget on cross-sections of the run transverse (YZ) plane, as shown in Figure 6.1, along with the coordinates of points (0 cm, 0 cm, 0.3 cm) from the bottom of

the plate. The precipitate evolution for the AA 7017 system was modeled on the KWN framework [17] using the TC-Prisma module of Thermo-Calc software.

Table 6.2: Material and other parameters of plate and tool for simulation

FSW process conditions	
Material	AA 7017-T7651
Tool material	H13 steel
Shoulder diameter (mm)	8.128
Pin Length (mm)	6.604
Pin diameter (mm)	3.276
Tilt	2.5 degree
Tool	threaded, cylindrical pin, and a dished shoulder
Weld speed (mm/sec)	1.69
Tool rotation rate (RPM)	300 and 600
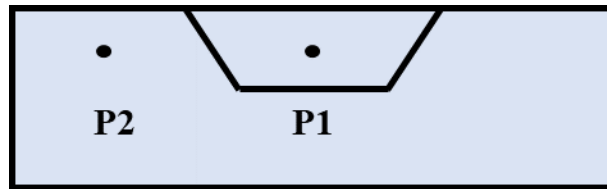
Figure 6.1:Schematic of locations of points for the thermal cycle.

Experimental FSW was performed in position control mode using the Manufacturing Technology, Inc. friction stir welding machine with thermocouples inserted in the tool to measure the thermal profile during the experiment for the nugget shown as a schematic in Figure 6.2. The parameters used for the experimental FSW runs were the same as those used for the simulations, as in Table 6.2. The welds were subjected to post-weld heat treatments (PWHT) in an oven with air at 121°C for 24 hours. DSC was performed for precipitate type and volume fraction for the precipitates for the nugget and BM for the two different parameters. All DSC runs were made from room temperature to 550°C at a heating rate of 10°C/min. TEM samples were prepared using a dual-beam FEI Nova 200 Nano Lab focused ion beam microscope, and FEI Tecnai G2 F20 S-

Twin operating at 200 keV was used for TEM imaging for selected samples. Mechanical property evaluations were conducted for both as-welded and PWHT conditions using the mini tensile test for the nugget and BM at room temperature with a strain rate of $10^{-3}s^{-1}$ with a gauge length and width of ~5 mm and ~1.25 mm, respectively.
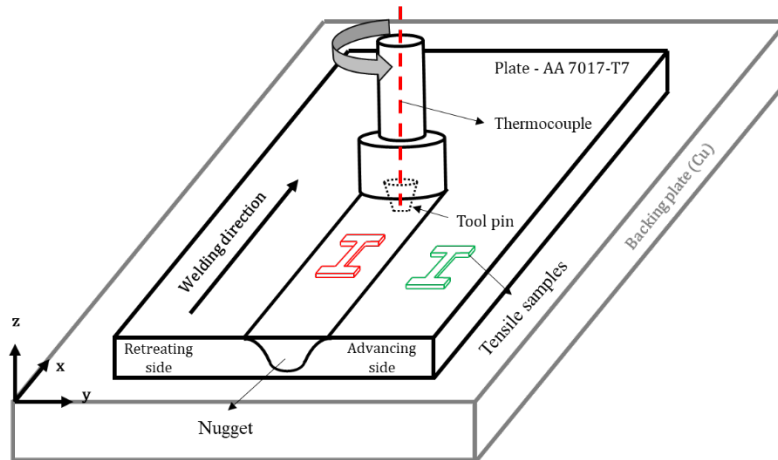
Figure 6.2: Schematic of FSW with a thermocouple inserted in the tool and locations marked for mini tensile samples.

6.4 Results and Discussion

The results are discussed in two parts: (a) Super-predictor – a one-stop-place to get answers related to FSW, which involves thermal profile, microstructure, and properties via simulations for different weld parameters, and (b) involving the validation of the model via experiments.

6.4.1 Super-Predictor

6.4.1.1 Thermal Model

The thermal model for FSW for the present study was solved using a steady-state Eulerian solution in COMSOL-Multiphysics to understand the effect of process parameters generating heat and thus, influencing the final properties of the weld [26]. In addition, the thermal model is a starting point for other succeeding models of microstructure and or precipitation of FSWed material. The heat transfer model deals with the heat source and heat distribution (transfer) under

different thermal boundary conditions. This model presents temperature-dependent flow stress as the heat source and thus is called a thermal pseudo-mechanical model. Assumptions made during the simulations are that friction shear stress and deformation stress are in equilibrium in the shear layer close to the tool and workpiece interface. The model was developed using the heat transfer module in COMSOL [26], where the following energy equation is solved,

$$\frac{\rho C_p}{k}\left(u\frac{\partial \tau}{\partial x} + v\frac{\partial \tau}{\partial y} + w\frac{\partial \tau}{\partial z}\right) = \frac{\partial^2 \tau}{\partial x^2} + \frac{\partial^2 \tau}{\partial y^2} + \frac{\partial^2 \tau}{\partial z^2} + q \qquad \text{(Eq. 6.1)}$$

where ρ is the density, C_p is the specific heat, and q is the heat source. The contribution of heat generation from friction and plastic deformation was defined in terms of a surface flux in the coming sections. The heat source q was considered as an infinitesimal element at a distance r from the tool center rotation at an angular velocity of ω and is given in the equation,

$$q = \omega r \tau_{contact} \qquad \text{(Eq. 6.2)}$$

where $\tau_{contact}$ is the shear stress at the workpiece element under consideration.

$$\tau_{contact} = \delta \tau_{yield} + (1-\delta)\tau_{friction} \qquad \text{(Eq. 6.3)}$$

τ_{yield} is the temperature-dependent shear stress of the material, and δ is a dimensionless parameter of slip rate with various varying from 0 to 1. It is expressed as,

$$\delta = \frac{v_{matrix}}{v_{tool}} \qquad \text{(Eq. 6.4)}$$

where v_{matrix} is the matrix velocity of the deforming material at the interface of the tool, v_{tool} is the tool velocity. Assuming a steady-state condition at the tool-matrix interface leads to the following relation [5]

$$\tau_{friction} = \tau_{contact} = \tau_{yield} \qquad \text{(Eq. 6.5)}$$

In this model, the material constitutive law considered the first-order effect of thermal softening without considering the influence of strain hardening and strain rate hardening on the flow stress. The flow stress of a material depends on both temperature and strain rate. The model

76

also considered the backing plate, as it acts as a heat sink resulting in a significant amount of heat is loss through the bottom of the workpiece. Figure 6.3 (a) represents the thermal model flowchart, and Figures 6.3(b) and (c) show meshed geometry and the tool geometry for the thermal model. The tool designed for the model resembles the tool used for the experimental runs. The fine-meshed region near the tool and workpiece interface in Figure 6.3(b) represents the effect of a high thermal gradient.
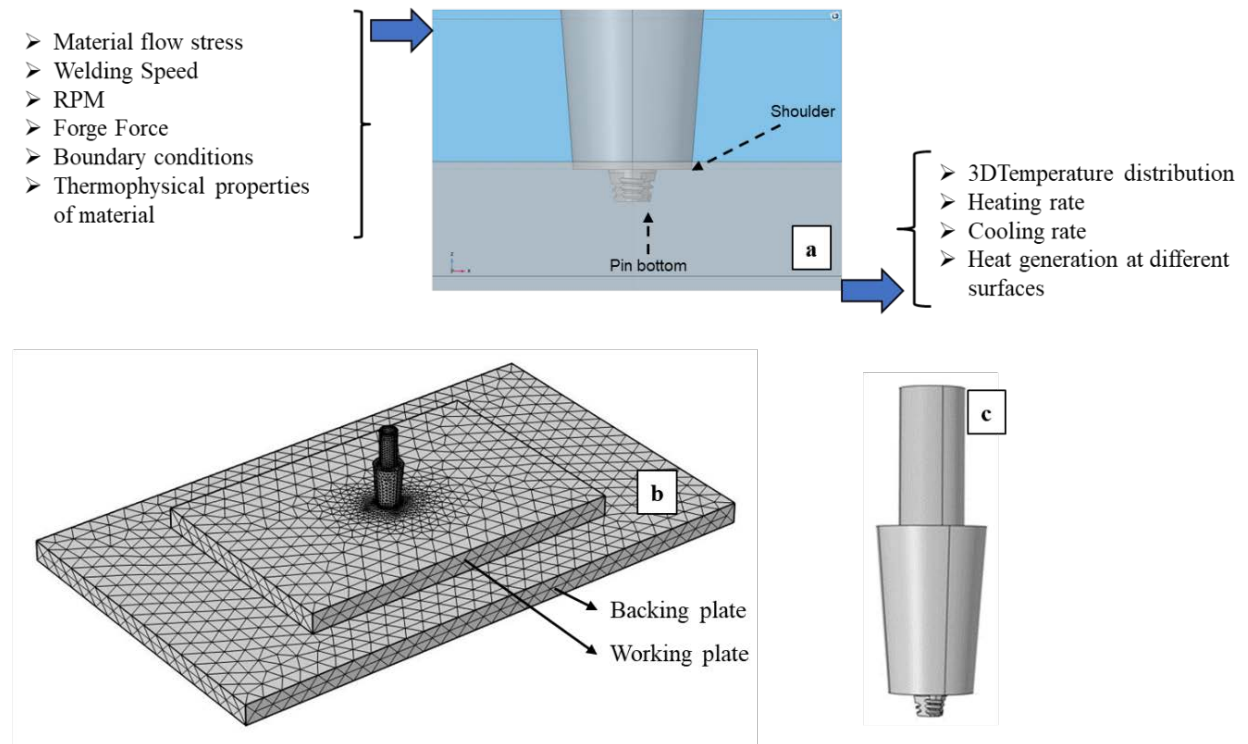
Figure 6.3: (a) Flow chart of the thermal model, (b) meshed geometry, and (c) tool design used in the model.

The material was assumed to follow the von-Mises yield criteria where different thermal boundary conditions were applied to the different surfaces. The convective heat transfer coefficients h_{air} were used on the top surface of the workpiece and backing plate that was exposed to air. The h_{bottom} was provided at the bottom of the backplate, and the tool surface exposed to air was modeled with the convective heat transfer coefficient of h_{tool}. The values for the heat transfer coefficients [27] are mentioned in Table 6.3.

Table 6.3: Different heat transfer coefficients used in the thermal model

Heat Transfer Coefficient	W/m².K
h_{air}	700
h_{bottom}	500
h_{tool}	800

The heat is generated on the tool shoulder and pin bottom surface, and the computed temperature profiles in the 3D view and YZ plane is shown in Figure 6.4. The contour maps in Figures 6.4(a) and (b) show the compressed temperature profiles in the front of the tool and expanded behind it. The effect of the parameters on the nugget, i.e., P1, is recorded in the simulated temperature profile in Figure 6.4(d). Local variations of relative velocities between workpiece and tool surface and material thermal conductivity result in a difference of ~52°C in heat generation, thus ensuing in the asymmetry in the temperature profile as observed in Figure 6.4. Thermal cycles are generated from point P1 for different parameters are seen in Figure 6.4(d). 600rpm/4ipm showed a higher peak temperature of 455°C compared to the 300rpm/4ipm run, where the peak temperature was 396°C. The higher rotational speed resulted in a higher peak temperature.
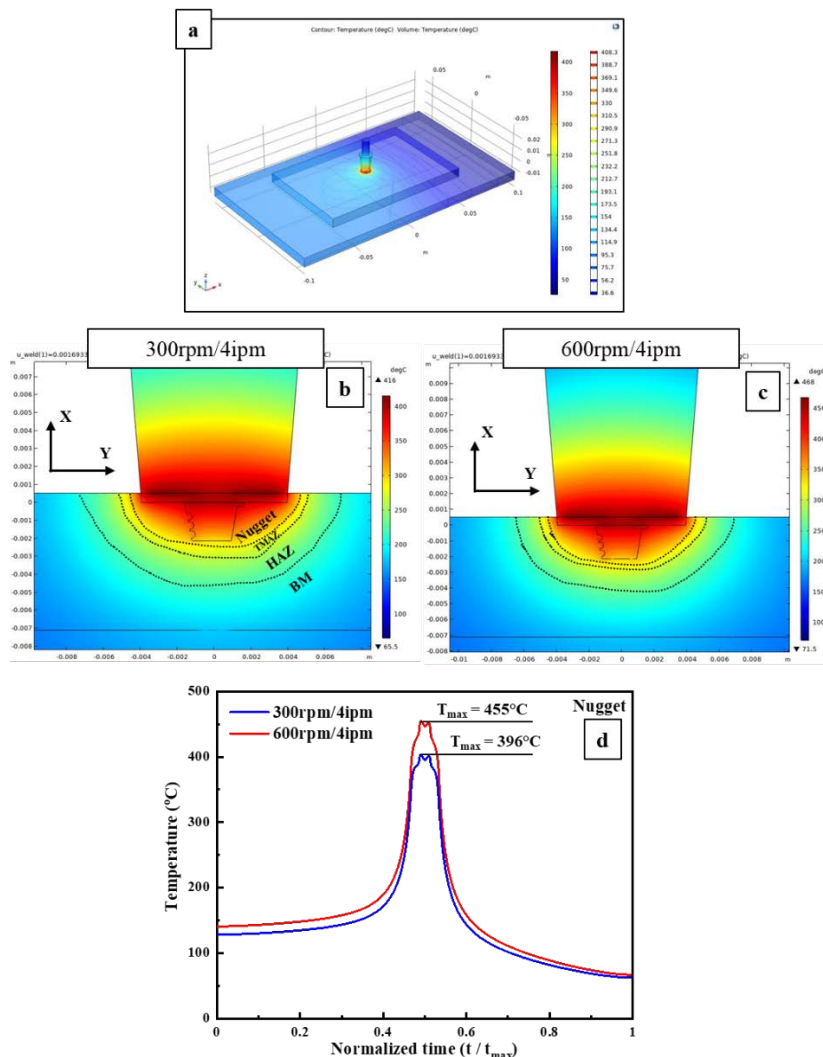
Figure 6.4: Computed temperature profiles in (a) 3D view of the weld for 300rpm/4ipm, 2D view (x = 0, YZ plane) along with the heat generation in the different surfaces of tool shoulder and pin (b) 300rpm/4ipm, (c) 600rpm/4ipm and (d) results for simulation in terms of the time-temperature thermal profile for the two parameters.

6.4.1.2   Microstructure Model via KWN Framework

Using the classical nucleation and growth theory, the KWN [21] framework describes the nucleation, growth, and coarsening of precipitates in discrete time. After every step, the matrix composition is calculated using the mean-field approach, thus predicting growth and coarsening.

AA 7017 is an Al-Zn-Mg alloy system containing various precipitates like GP zones, η', and η. The thermal cycle during FSW results in different levels of dissolution of metastable and stable phases, transforming metastable phases to stable phases, and reprecipitation and/or coarsening of the phases over the cooling cycle. The KWN method predicts the evolution of multiple phases at multisite in a multicomponent system.

6.4.1.2.1   Nucleation of Precipitates

Homogenous nucleation rates given by classical nucleation theory are [28,29]:

$$J(t) = J_s \, exp\left(-\frac{\tau}{t}\right) \tag{Eq. 6.6}$$

where J_s is the steady-state nucleation rate, τ is incubation time, and t is the time. The nucleation rate can also be expressed as

$$J(t) = Z\beta^* N_o \, exp\left(-\frac{\Delta G^*}{kT}\right) \tag{Eq. 6.7}$$

where Z is the Zeldovich factor, β^* is the rate at which atoms or molecules are attached to the critical nucleus, N_o is the number of available nucleation sites per unit volume, ΔG^* is the Gibbs free energy for critical nucleus formation, and T is the absolute temperature.

The Gibbs free energy (ΔG^*) is

$$\Delta G^* = \frac{16\pi\sigma^3}{3\left(\frac{\Delta G_m^{\alpha\to\beta}}{V_m^\beta}\right)^2} \tag{Eq. 6.8}$$

where σ is interfacial energy, $\Delta G_m^{\alpha\to\beta}$ is molar Gibbs free energy for the formation of β precipitate

from the α matrix, and V_m^β is the molar volume of β precipitate, assumed to depend only on the chemical-free energy of the driving force of nucleation sites, which reduces the energy barrier for critical nucleus formation.

6.4.1.2.2   Growth Theory

The model developed by Chen, Jeppsson, and Agren (CJA) was used for precipitate growth [30]. The velocity of a moving phase interface was determined by identifying the operating tie-line and solving the flux balance governing equation. The interfacial velocity v can be obtained from the following expression

$$v\left(c_i^{\frac{\beta}{\alpha}} - c_i^{\frac{\alpha}{\beta}}\right) = c_i^{\alpha/\beta} M_i \frac{\mu_i^\alpha - \mu_i^{\alpha/\beta}}{\xi_i r} \qquad \text{(Eq. 6.9)}$$

$$\mu_i^{\alpha/\beta} = \mu_i^{\beta/\alpha} + \frac{2\sigma V_m^\beta}{r} \qquad \text{(Eq. 6.10)}$$

where, $c_i^{\frac{\beta}{\alpha}}$ and $c_i^{\frac{\alpha}{\beta}}$ are the volume concentration of component i at the interface, M_i is atomic mobility in the matrix, μ_i^α is the chemical potential of mean-field concentration in the matrix, $\mu_i^{\alpha/\beta}$ is chemical potential at the interface in the matrix, $\mu_i^{\beta/\alpha}$ is chemical potential at the interface in the precipitate, and ξ_i is the effective diffusion distance factor for component i. Combining equations (6.9) and (6.10), velocity is defined as

$$v = \frac{K}{r} \left[\Delta G_m - \frac{2\sigma V_m^\beta}{r} \right] \qquad \text{(Eq. 6.11)}$$

where K is the chemical factor and V_m^β is the molar volume of the precipitate phase in the matrix. In the present study, to avoid complications, TC-PRISMA was used by using the initially calculated operating tie-line.

In this study, time-temperature profiles in nugget were extracted from the thermal model generated in COMSOL Multiphysics and were used in the KWN model. Assumptions and

considerations made for the microstructure model:

1. The thermal weld cycle was assumed to influence the precipitate evolution, and the strain was neglected to maintain simplicity in calculations.

2. Considering bulk nucleation of η´ and nucleation of η at the grain boundary

3. The precipitate shape was considered spherical. However, in reality, η´ and η exist as plates

4. The formation of GP zones was excluded after the thermal weld cycle in the nugget. Thus, the model predicts the precipitates just after the thermal weld cycle, and the formation of GP zones will only occur after some time.

The initial precipitation in BM of AA 7017-T7 was performed by subjecting the material to aging treatment at 160°C for 24 hours (usually followed in an industrial process for achieving T7 temper in AA 7017). The initial precipitate distribution of BM was calibrated using TEM, where volume fraction and precipitate mean radius was calculated in Figure 6.5. The average radius for η´ was 2.5nm.
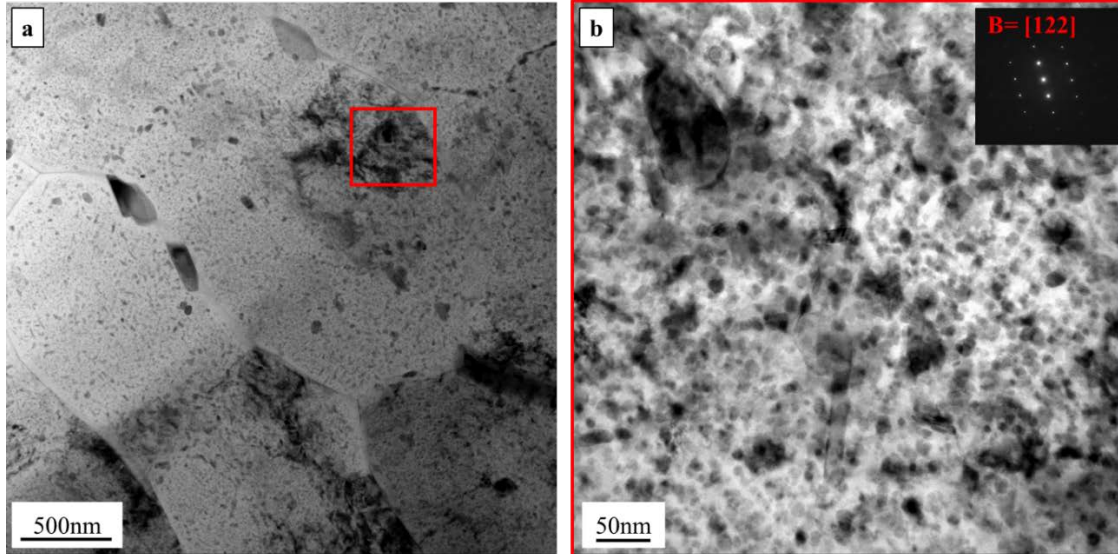
Figure 6.5: TEM images showing the volume fraction and average radius of precipitates present in the BM

Model prediction for BM-T7 when subjected to aging at 160°C for 24 hours is shown in Figure 6.6. Figure 6.6(a-b) displayed the status of the volume fraction and the average radius of

the precipitates post heat treatment. The volume fraction and average radius of strengthening precipitates η′ are lower than the η precipitates at the end of the aging treatment, and the average radius values were 0.0121 nm and 1.65 nm, respectively. The solute amount available for the precipitates to nucleate and grow post-aging was calculated using the model predictions for matrix composition in Figure 6.6(c). The solute present was 3.8 wt% Zn, 2.45 wt% Mg, and 0.12 wt% Cu. The results for the BM are then used in running simulations for the nugget region for different weld parameters.
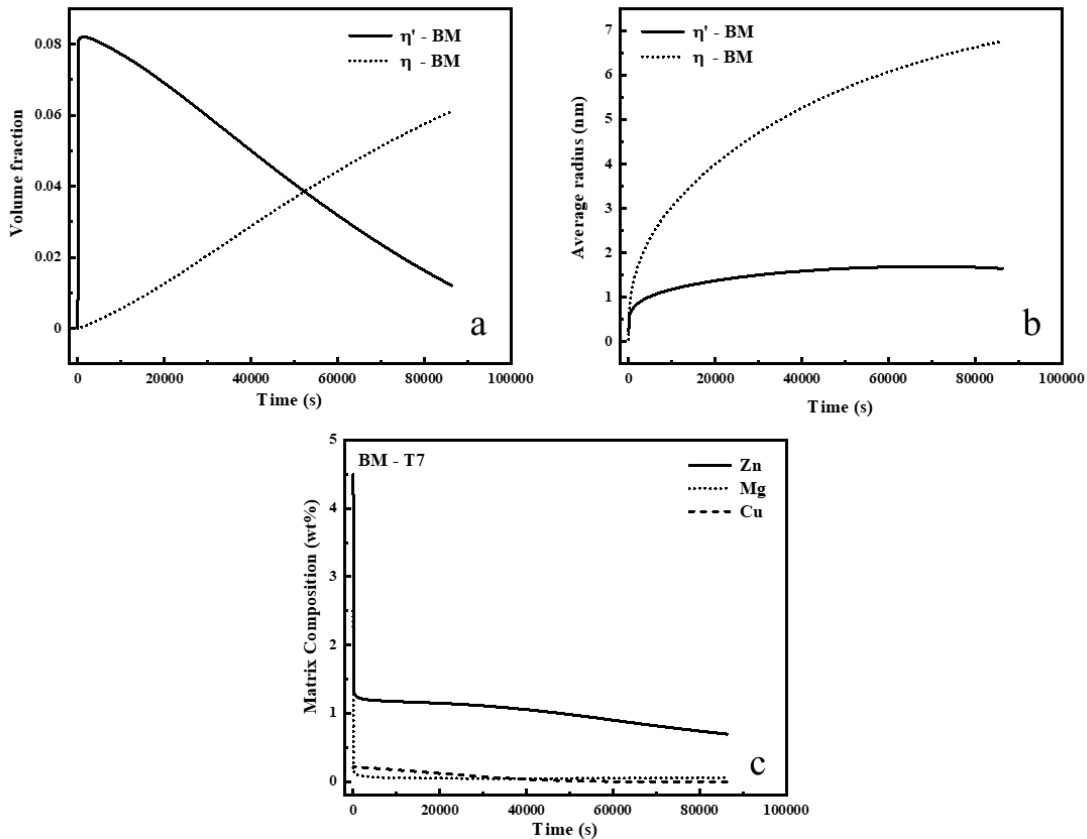
Figure 6.6: Model prediction for the BM-T7 aged at 160°C for 24 hours for the variation of (a) volume fraction, (b) average radius, and (c) matrix composition.

Model predictions for P1 (nugget) for the two weld parameters are shown in Figure 6.7(a). Figure 6.7(a_1) showed the evolution of the volume fraction of η′ and η at the nugget. As the peak temperature at P1 approaches ~390°C, the volume fraction of η′ increases and then suddenly drops,

82

as observed in Figure 6.7(a_1); the reason is the complete dissolution of small η' precipitates and the making of more solute available in the matrix for the transformation of η' to η. On cooling, the volume fraction of η precipitates increases, as observed in Figure 6.7(a_1). The effect of the FSW parameters is also observed in Figure 6.7(a_1), where the volume fraction of η for 300rpm/4ipm is ~0.0731 in comparison to the volume fraction for 600rpm/ipm is ~0.0524; however, the volume fraction for the strengthening precipitate η' is found to be zero. The lower volume fraction of η precipitates in 600rpm/4ipm run is due to the high temperature of ~455°C observed during welding resulting in more dissolution of precipitates and less time for nucleation. Thus, more solute in the matrix would eventually help evolve strengthening precipitates when subjected to PWHT. The effect of the welding parameters was also seen on the average radius of the precipitates, as illustrated in Figure 6.7(a_2). The initial peaks represented in the solid line for the nugget in Figure 6.7(a_2) seem to be increasing to an average radius of ~1.8nm with an increase in temperature, but they dissolve just before the nugget approaches the peak temperature at P1. Thus, indicating the dissolution of small η' precipitates. On cooling, the surviving precipitates tend to coarsen with an average radius of 0.55nm. The average radius of η precipitates for 300rpm/4ipm and 600rpm/4ipm were ~7.52nm and ~1.49nm, respectively (Figure 6.7a_2). Thus, the number of precipitates dissolved and the increase in radius of the surviving precipitates were predicted to be directly related to the peak temperature during the FSW cycle. Figure 6.7(a_3) represented the matrix composition of the nugget when subjected to FSW and helped in accounting for the amount of solute present in the matrix. The remaining solute concentration observed in the 600rpm/4ipm run was 1.5 wt% Zn, 1.0 wt% Mg and 0.14 wt% Cu. The lower amount of solute was available post FSW in the 300rpm/4ipm run (1.0 wt% Zn, 0.67 wt% Mg, and 0.11 wt% Cu) because of the lower peak temperature during the weld, thus allowing more coarsening of existing precipitates than

dissolution. Hence, validating the higher volume fraction and larger average radius of precipitates post-weld in 300rpm/4ipm run compared to 600rpm/4ipm allows it to exhibit better mechanical properties.
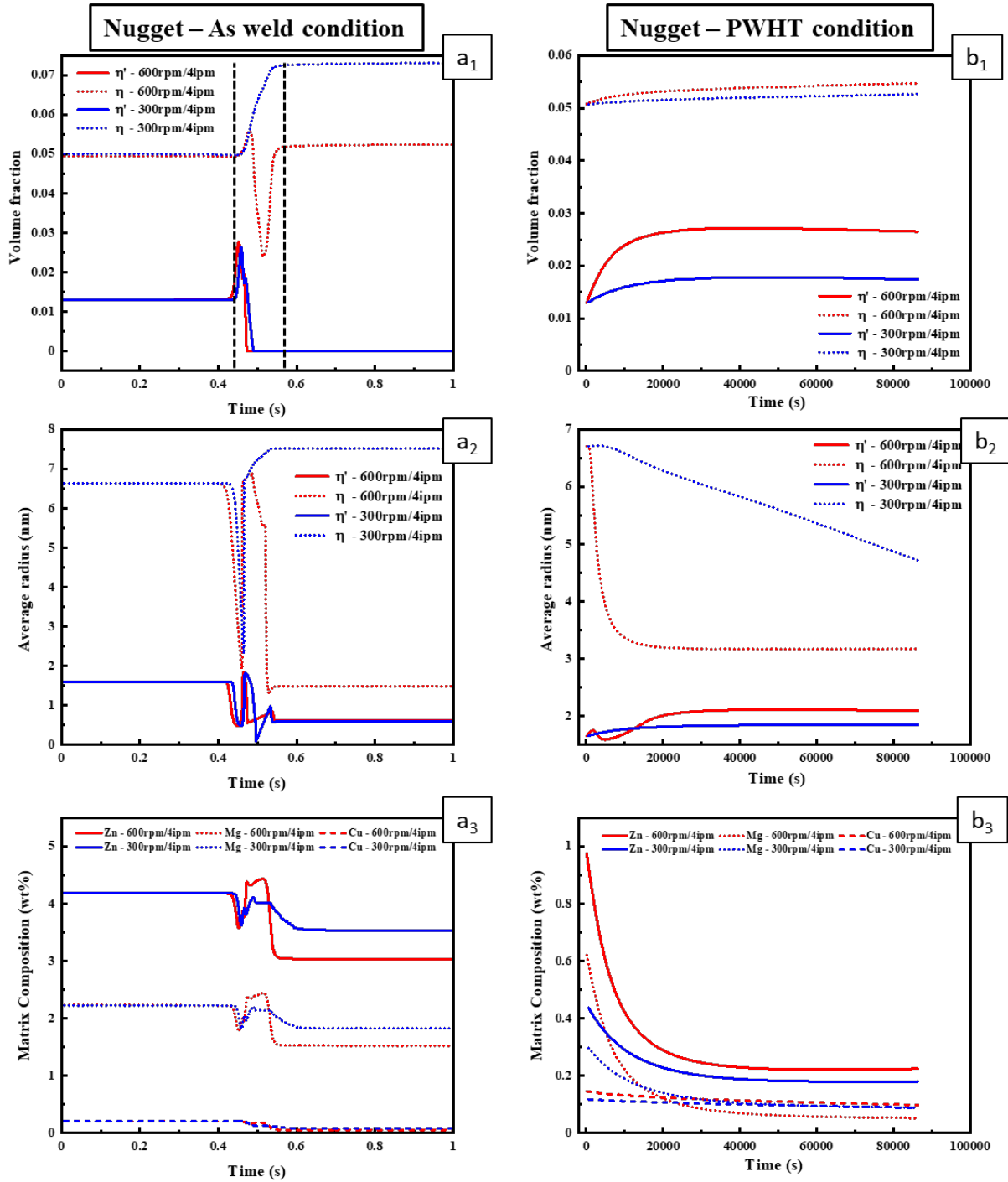
Figure 6.7: Model predictions for volume fraction, average radius, and matrix composition in nugget for (a1-a3) as-welded and (b1-b3) PWHT conditions.

Simulation results representing the effect of PWHT, i.e., 121°C for 24 hours, on the P1 region, are shown in Figure 6.7(b). Figures 6.7(b$_1$-b$_2$) showed improvement in the volume fraction and average radius of strengthening precipitates η´ at 600rpm/.4ipm run compared to 300rpm/4ipm run. The volume fraction for η´ observed in 600rpm/4ipm and 300rpm/4ipm were ~0.027 and ~0.017, respectively. The higher peak temperature observed in the 600rpm/4ipm run allowed more dissolution of existing precipitates, thus making more solute available in the matrix for nucleation and growth of precipitates when subjected to PWHT. Hence, better mechanical properties are expected in the 600rpm/4ipm run. A similar effect is observed in the average radius of the strengthening precipitate in Figure 6.7(b$_2$). The matrix composition (in Figure 6.7b$_3$) PWHT for both the weld parameters facilitated calculating the solid solution strengthening for the property model.

6.4.1.3   Property Model

A host of microstructural elements controls the strength of the material, and the primary strengthening mechanisms contributing [31] to the yield stress (σ_y) 7xxx alloy can be expressed as,

$$\sigma_y = \Delta\sigma_{gb} + M\left(\Delta\tau_0 + \Delta\tau_{SS} + \sqrt{\Delta\tau_{ppt}^2 + \Delta\tau_D^2}\right) \qquad \text{(Eq. 6.12)}$$

where $\Delta\sigma_{gb}$ is grain boundary strengthening, $\Delta\tau_0$ is the frictional stress in Al alloys, $\Delta\tau_{ss}$ is the solid solution strengthening, $\Delta\tau_{ppt}$ is the precipitation strengthening, $\Delta\tau_D$ is the dislocation strengthening, and M is the Taylor factor and is considered as 3 for fcc system. Each strengthening term is calculated to obtain the tensile strength of the weld in comparison to the BM.

6.4.1.3.1   Grain Boundary Strengthening

The yield strength can be related to the average grain size of the material using the standard

Hall-Petch relationship [32,33].

$$\Delta\sigma_{gb} = \sigma_f + kd^{-1/2} \qquad \text{(Eq. 6.13)}$$

where σ_f is the intrinsic lattice resistance to dislocation motion (i.e., ~16 MPa for fcc) and k is a parameter describing the relative strengthening contribution of grain boundaries which is ~ 0.065 MPa/m$^{1/2}$ for Al, and d is the average grain size. Based on the literature survey [5], the grain size observed in the nugget is in the range of 3μm - 8μm, and BM is ~40μm, where the higher rotational speed run resulted in larger grain. The results in Table 6.4 were calculated using Eq. 6.13.

Table 6.4: The calculation for grain boundary strengthening

Run	Condition	Average grain size (d - μm)	GB Strengthening (MPa)
BM	T-7	40	26.3
300rpm-4ipm	As-weld	4	48.5
600rpm-4ipm		6	42.5

6.4.1.3.2   Solid Solution Strengthening

The solid solution strengthening in AA 7017 depends on the concentration of solute in the solid solution and is represented as [34]

$$\Delta\tau_{SS} = \sum_i A_i C_{o,i}^{2/3} \qquad \text{(Eq. 6.14)}$$

where A is the solid solution coefficient for the alloying elements and C_0 is the solute concentration in the matrix. Table 6.5 showed the values for the solute concentration obtained from the different weld runs (in Figure 6.7a$_3$) and the BM (in Figure 6.6a$_3$) taken from the simulations ran for matrix composition on TC-Prisma. The contribution of solid solution strengthening in as-welded conditions, i.e., ~39.97MPa and 35.41MPa for 300rpm/4ipm and 600rpm/4ipm, respectively, is quite significant compared to the PWHT and BM conditions.

Table 6.5: Results for solid solution strengthening

Run	Condition		Elements			Solid Solution strengthening (MPa)
			Mg	Cu	Zn	
		A	20.481	12.431	3.085	
BM	T-7	C_0	0.06	0.08	0.699	7.98
300rpm-4ipm	As-weld	C_0	1.825	0.0837	3.53	39.97
600rpm-4ipm		C_0	1.527	0.058	3.04	35.41
300rpm-4ipm	PWHT	C_0	0.0892	0.0885	0.1808	7.66
600rpm-4ipm		C_0	0.0525	0.0983	0.2246	6.77

6.4.1.3.3 Dislocation Strengthening

The contribution of dislocations to strengthening Eq. 6.15 is related as follows [35,36].

$$\Delta\tau_D = \alpha Gb\sqrt{\rho} \qquad\qquad \text{(Eq. 6.15)}$$

where G is the shear modulus (~26 GPa), b is the Burgers vector, i.e., 0.286 nm for Al, ρ is the dislocation density, and α is constant with the value of 0.3. The dislocation density is estimated by the X-ray line broadening method following Ungar et al. [37] for BM and nugget for both the weld parameters. The dislocation strengthening calculation is mentioned in Table 6.6.

Table 6.6: Results for dislocation strengthening

Run	Condition	ρ (m^{-2})	Dislocation Strengthening (MPa)
BM	T-7	8.26E-14	64.114
300rpm-4ipm	as-weld	9.17E-14	67.553
600rpm-4ipm	as-weld	8.73E-14	65.912

6.4.1.3.4 Precipitation Strengthening

The current model for AA 7017 is characterized by the primary strengthening precipitates η'. These precipitates act as obstacles to moving dislocations that must either shear through (for small size precipitates) or bypass them (for large-sized particles). The strength depended upon the

precipitate size, shape, and volume fraction. For the present study, the precipitation strengthening mechanism was calculated using the ideal condition of precipitates using the Orowan theory [31] (Eq. 6.16) and the modified Orowan theory [38] mentioned in Eq. 6.17. Also, only shearing of precipitates is considered for the property model as the precipitates are not big enough for the bypass mechanism to take place as the simulations are recorded just after the weld, allowing no coarsening of precipitates,

$$\Delta\tau_{ppt} = \sqrt{\frac{3}{4\pi\beta}} \frac{k^{3/2}G}{\sqrt{b}} (f \times r)^{1/2} \qquad \text{(Eq. 6.16}$$

$$\Delta\tau_{ppt} = \frac{Gb}{\lambda} [\cos(\frac{\phi_{cr}}{2})]^{3/2} \qquad \text{(Eq. 6.17)}$$

where r is the average radius of η' precipitates (nm), f is the volume fraction of η', γ is the energy required to form antiphase boundary (0.185 J/m^2), k and β are constants with the value of 0.07 and 0.43, respectively. The critical angle ($\phi_{cr)}$ and inter-particle spacing (λ) were calculated using Eq. 6.18 and 6.19.

$$\lambda = 1.23r\sqrt{\frac{2\pi}{3f}} \qquad \text{(Eq. 6.18)}$$

$$\phi_{cr} = 2\cos^{-1}[\frac{\sqrt{f}\gamma^{\frac{3}{2}}}{G^{\frac{3}{2}}b^3} (\lambda\sqrt{r})]^{2/3} \qquad \text{(Eq. 6.19)}$$

The values for the average radius and volume fraction for the strengthening precipitates η' for both the as-welded and PWHTed conditions compared to BM were taken from the microstructure model in Figure 6.7 and summarized in Table 6.8 with the calculation of precipitation strength using Eqs. 16 and 17. The volume fraction for the strengthening precipitates in the as-welded condition was negligible due to the dissolution of precipitates in the as-welded condition. Thus, their contribution to the calculation of the strengthening mechanism is zero. However, a significant contribution was observed in the case of BM and PWHTed conditions. The

other observation made in the PWHTed condition is that 600rpm/4ipm showed higher strength values than the 300rpm/4ipm run.

The strength values in Ideal-Orowan calculations are higher than in Modified-Orowan calculations (Table 6.7). The reason is that the dislocation interaction with the precipitates solely depends on the volume fraction and mean radius of the precipitates. However, in the Modified-Orowan theory, dislocation interaction with the precipitate depends not only on the volume fraction and average radius but also on the inter-particle spacing and orientation of particles, allowing it to be closer to the real-time precipitation distribution [38]. Hence, the lower strength values are observed in the Modified-Orowan theory, and their contribution,

Table 6.7: Summary for precipitation strengthening using data from the microstructure model.

Run	Condition	f	r (nm)	Ideal-Orowan (MPa)	Modified-Orowan (MPa)
BM	T-7	0.0121	1.647	94.53	86.33
300rpm-4ipm	As-weld	0	0.59	0.00	0.00
600rpm-4ipm		0	0.627	0.00	0.00
300rpm-4ipm	PWHT	0.0174	1.84	120.06	95.86
600rpm-4ipm		0.0265	2.099	158.25	103.70

The results in Table 6.8 summarize each strengthening mechanism's contribution. The significant contribution to yield strength (YS) in the as-welded condition is the solid solution strengthening mechanism with the values of ~40 MPa and 35 MPa for 300rpm/4ipm and 600rpm/4ipm, respectively, whereas no contribution is observed from the precipitation strengthening mechanism. Thus, a drop-in YS for nugget is observed compared to BM. However, in the PWHTed condition, the lowest contribution is observed from the solid solution strengthening mechanism because post-heat treatment, the maximum solute is consumed in the nucleation, and the growth of new strengthening precipitates left no solute in the matrix. Using the

same theory of nucleation and growth of strengthening precipitates when heat-treated at 121°C for 24 hours allowed enough time for the precipitates to nucleate and grow, contributing to the total strengthening mechanism. Thus, a high amount of contribution from the precipitation strengthening mechanism is observed, leading to improvement in YS of the nugget region compared to the as-welded and BM region.

Table 6.8: Results summarizing the contribution of each strengthening mechanism

Material	Condition	$\Delta\sigma_{gb}$	$\Delta\tau_{ss}$	$\Delta\tau_{ppt}$ Ideal	$\Delta\tau_{ppt}$ Modified	$\Delta\tau_D$	σ_y Ideal-YS	σ_y Modified -YS
BM	T-7	26.3	7.98	95	86.33	64.1	424	403
300rpm-4ipm	As-weld	48.5	39.97	0	0	67.6	401	401
600rpm-4ipm		42.5	35.41	0	0	65.9	376	376
300rpm-4ipm	PWHT	48.5	7.66	120	92.86	67.6	515	453
600rpm-4ipm		42.5	6.77	144	100.46	65.9	567	461

6.4.2 Validation via Experiments

6.4.2.1 Temperature Profile

The temperature values obtained from the thermocouple inserted in the tooltip are shown in Fig. 6.8 (a), which depicts the influence of process parameters on the peak temperature and the macro-image of the defect-free welds (in Figure 6.8b$_1$-b$_2$). Higher rotational rate resulted in higher peak temperature impacting the precipitation evolution, which further influences the mechanical properties of the weld. Peak temperature during FSW in nugget for 600rpm/4ipm was recorded as ~450°C, whereas 300rpm/4ipm is ~370°C. Also, the thermal profile recorded via thermocouple was lower than the simulated thermal profile. The welding environment plays an important factor, whereas the simulation took place in a controlled environment (Figure 6.5). Hence a lower peak temperature was observed in the experiments.
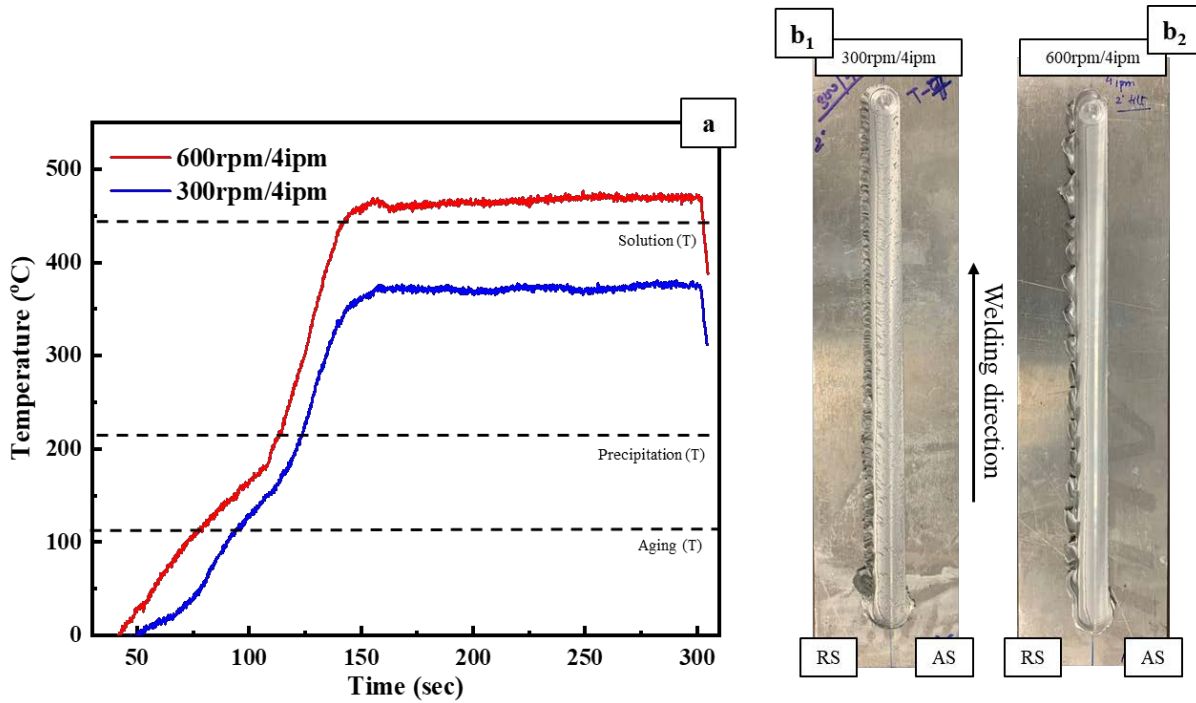
Figure 6.8: Temperature profile recorded in nugget via inserting thermocouple and (b₁-b₂) macro images of the defect-free welds.

6.4.2.2   DSC and Microstructural Characterization

DSC was used to validate the precipitation behavior during FSW in nugget compared to BM. The exothermic peaks in Figure 6.9 correspond to the formation of precipitates, and the dissolution of precipitates is identified as endothermic peaks [39,40]. Peak A is due to the dissolution of GP zones, peak B corresponds to the formation of strengthening precipitates, and peak C spanning approximately 330°C to 430°C identifies as the dissolution of high-temperature precipitates [40]. The results for the as-welded condition in Figure 6.9, the volume fraction of strengthening precipitates (peak B) in the 300rpm/4ipm run is more significant than in the 600rpm/4ipm run because the low peak temperature during weld allowed less dissolution of precipitates in the matrix, signifying that more solute is available in the matrix for the 600rpm/4ipm run. However, when the samples were subjected to PWHT (dotted lines in Figure 6.9), improvement in volume fraction of strengthening precipitate was observed in the 600rpm/4ipm

run by the formation of new precipitates and the coarsening of existing precipitates. In the 300rpm/4ipm aged sample coarsening of precipitates was more dominant, and the same is reflected in the reduced volume fraction of formation of strengthening precipitates. The TEM results in the upcoming section validate the DSC results.
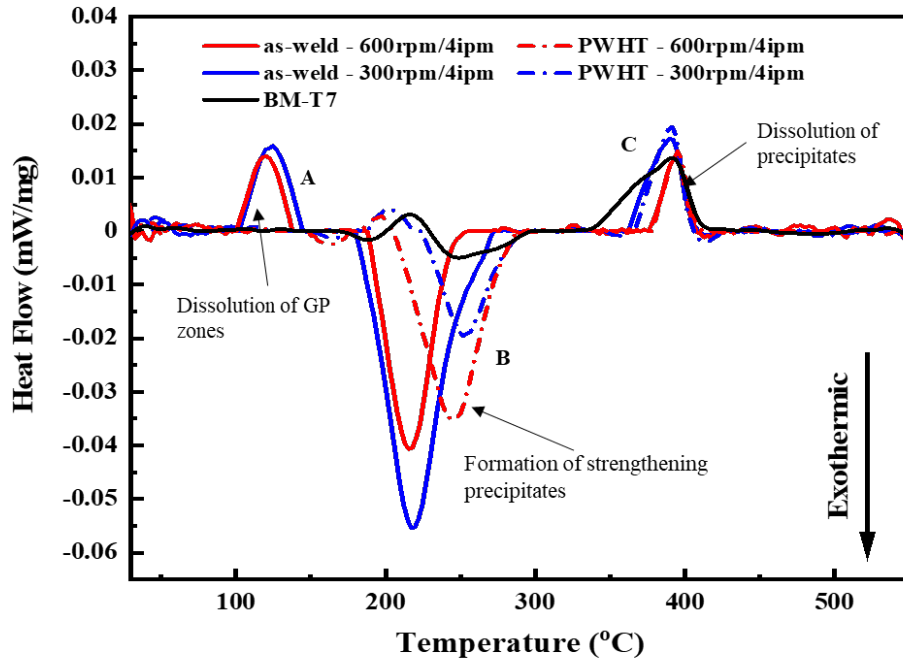
Figure 6.9: DSC results of samples from nugget in as-weld and PWHT condition in comparison to BM - T7.

Figure 6.10 shows micrographs of samples obtained from the nugget of 300rpm/4ipm and 600rpm/4ipm in as-weld conditions. High temperature and processing strain during FSW dissolved the existing precipitates to form a supersaturated solid solution in the nugget. The SEM image of the fully recrystallized, near-equiaxed grain structure of the nugget in Figure 6.10(a, b) showed the effect of weld parameters with a difference in grain size of 4μm and 6μm for 300rpm/4ipm and 600rpm/4ipm runs, respectively. The low magnification TEM image in Figures 6.10(a_1, b_1) displayed the precipitation evolution in the nugget. The low amount of precipitates are observed in the 600rpm/4ipm nugget due to a higher peak temperature of ~450°C, causing dissolution of

precipitates into the matrix (Figure 6.10b$_1$). However, the lower rotational rate run in Figure 6.10(a$_1$) showed an extensive range of precipitates ranging from 2-7 nm to 15-25 nm.
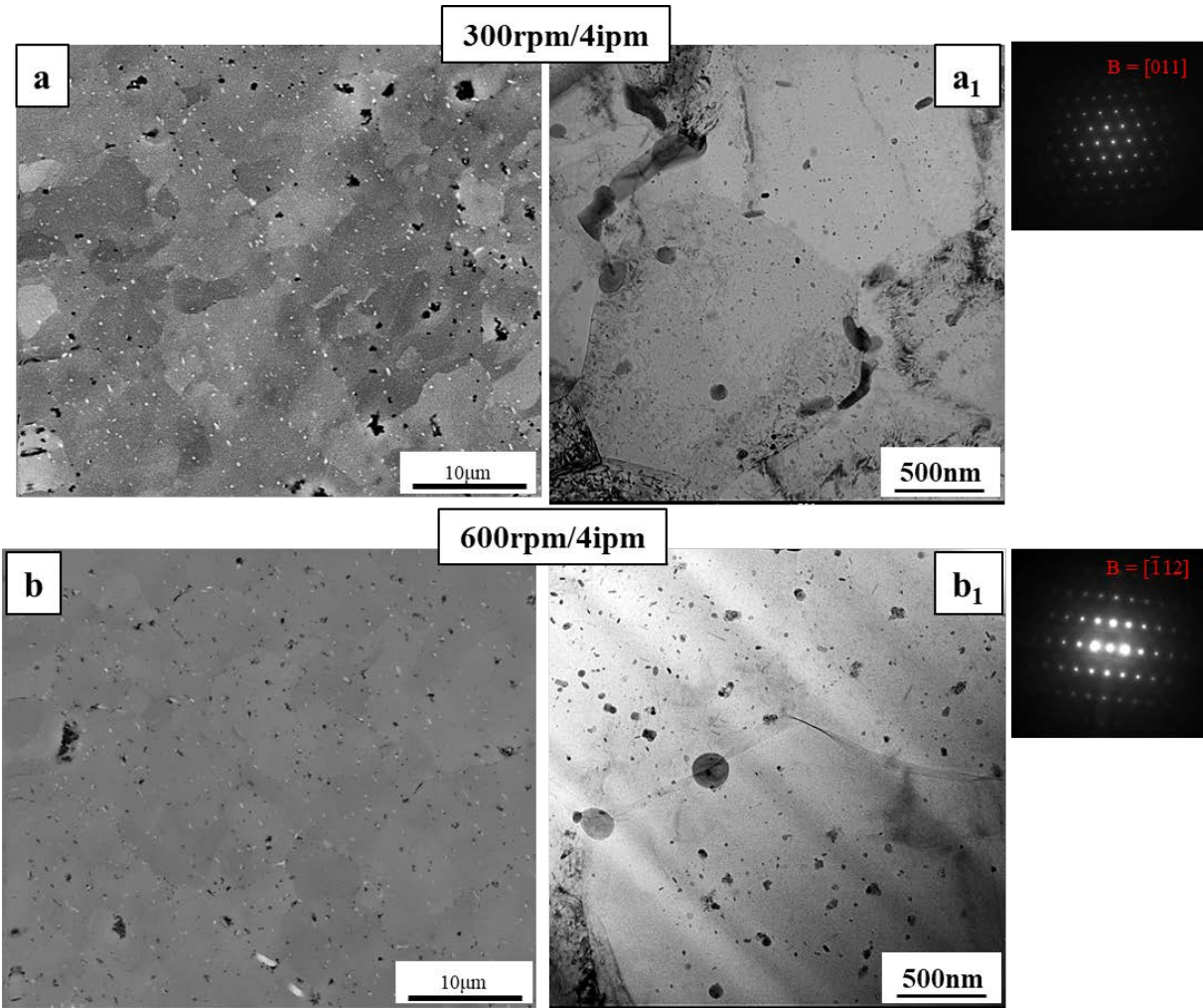
Figure 6.10: Micrographs for nugget in as-weld condition (a - a1) low magnification SEM image of nugget along with the TEM image showing the precipitates evolution in 300rpm/4ipm run, B= [011], (b) low magnification SEM image of nugget along with the TEM image showing the precipitates evolution in 600rpm/4ipm run, B=[112].

The effect of PWHT on nugget was captured via TEM images shown in Figure 6.11. The significant coarsening of precipitation was observed in the 300rpm/4ipm run in Figure 6.11(a) compared to the precipitates in as-welded conditions for the same weld (Figure 6.10). The average strengthening precipitate size observed in the 300rpm/4ipm run is ∼ 12 – 15nm, along with the precipitate-free zones (PFZ) formed around the grain boundary marked in Figure 6.11(a$_1$).

93

Figure 6.11: Low and high magnification TEM image PWHTed nugget to capture the precipitation evolution (a, a₁) 300rpm/4ipm, B=[011] and (b, b₁) 600rpm/4ipm, B= [112].

The coarsening observed in the 300rpm/4ipm run is due to PWHT, which resulted in the formation

of PFZ, meaning depleted solute concentrations near the grain boundaries. Ogura et al. [41] studied

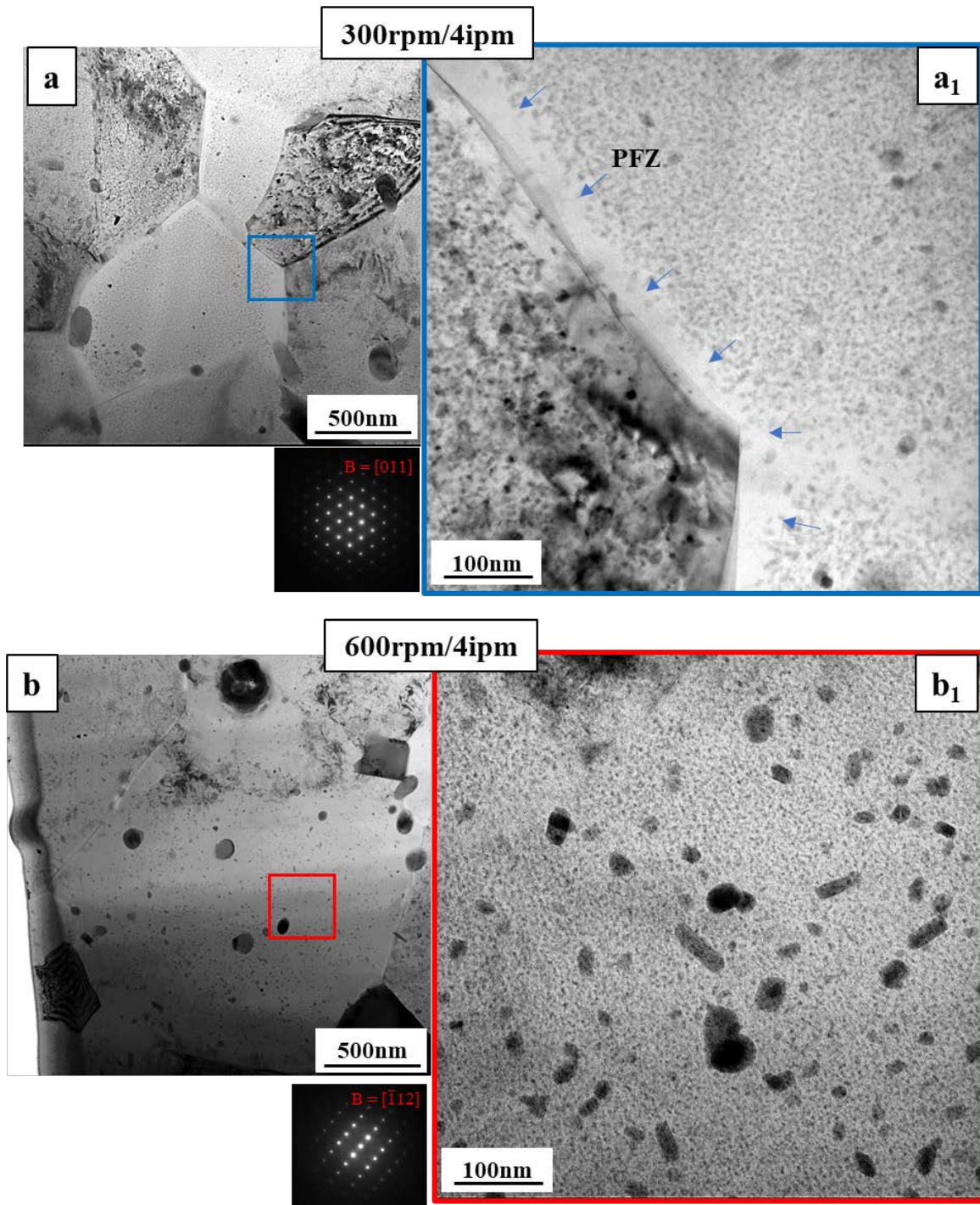the effect of FSW and aging post-weld on the solute concentration for the formation of PFZs. However, the TEM image of the nugget for 600rpm/4ipm run in Figures 6.11(b, b_1) showed a high-volume fraction of homogenously distributed precipitates formed with no PFZ formation when subjected to PWHT. The reason being enough solute was available in the matrix for precipitates to form and grow, allowing a chance to improve the mechanical properties of the weld.

6.4.2.3   Mechanical Properties

Mini tensile tests from the welds in all conditions compared to BM are shown in Figure 6.12(a). The tensile test helped in quantifying the mechanical response of the weld when subjected to load. Nugget for as-welded condition showed inferior mechanical properties compared to BM. The reason was simply because of the dissolution of precipitates observed in the nugget during the FSW process. However, the 300rpm/4ipm run in as-welded condition showed higher strength (~340MPa) than the 600rpm/4ipm run where the YS was ~326 MPa in Figure 6.12(a). The reason is that 600rpm/4ipm run experienced high peak temperature, causing more dissolution of precipitates. However, when the samples were subjected to PWHT, improvement in strength was observed in the nugget compared to the BM run due to the formation of new strengthening precipitates. The YS of 600rpm/4ipm and 300rpm/4ipm run observed post-heat treatment were 456MPa and 425MPa, respectively.

The experimental strength of weld and BM are lower than the simulated values, as shown in Figure 6.12(b). Higher strength values obtained through simulation are dependent upon the assumption and simplification of the model. The fundamental assumption made for the simulations is the shape, nucleation site, and type of precipitates that dominate the results. The impact of assumptions is reflected in the YS results generated from the property model in comparison to the experimental data are:

- The volume fraction and average radius of precipitates taken for calculation are just after the weld, which does not allow time for precipitates to grow and coarsen. In experimental values, samples were air-cooled after the welding, allowing growth and coarsening of precipitates. Thus, lower strength is observed in the experimental data.

- In reality, the considered precipitates are in the form of plates, whereas the assumption of precipitates as spheres affects the volume fraction and radius of precipitate size. Thus, higher strength is observed in the calculated values.

- The controlled distribution of precipitates by assigning the nucleation site of considered precipitates impacts the dislocation interaction with the precipitates. For the model, bulk nucleation of η´ is considered, which will cause multiple interactions; thus, high strength is observed. However, in real-time, the random distribution of precipitates causes a drop-in strength.

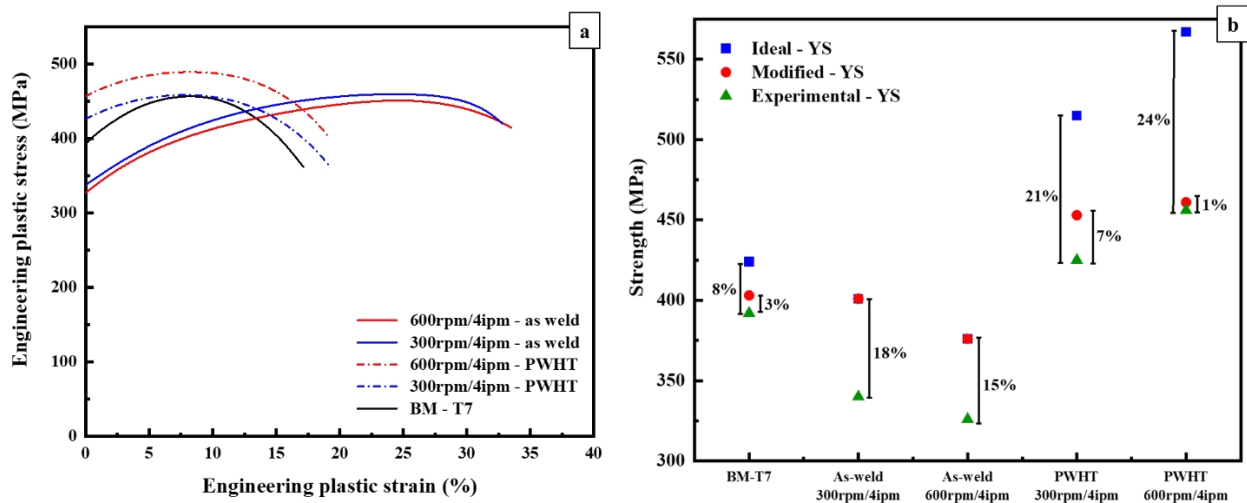**Figure 6.12: (a) Engineering stress-strain curves of 300rpm/4ipm and 600rpm/4ipm run in as-welded and PWHT conditions compared to BM-T7 and (b) strength comparison chart for experimental data with the simulated data**

.

6.5   Discussion

The generation of the temperature profile during FSW using the thermal model has a similar trend to the experimental data. A high peak temperature (~455°C) is observed with a high

rotational rate causing more dissolution of precipitates. The literature shows us that the temperature cycle affects the presence of strengthening precipitates and the time they are exposed to the peak temperature [3,5,15,22,23]. The effect of temperature on strengthening precipitate are:

1. For temperatures ~330°C – 430°C

   a. Dissolution of small η´ precipitates occurred while larger η´ precipitates transformed to η.

   b. Temperature close to 430°C, the η started to dissolve, leaving more solute available in the matrix

2. For temperature >430°C: The small η´ precipitates dissolved entirely, and η precipitates also dissolve, and a large amount of solute was available.

The effect of welding parameters showed a difference in mechanical properties after FSW. The weld run with a high rotational rate shows low strength in the as-welded condition than the slower rotational rate run and BM. However, the heat generated during a run affects the existing BM precipitates differently [20,42]. However, the extent of dissolution or coarsening depends on the size of the precipitates and the temperature reached. The simulated data showed peak temperatures of ~455°C and 396°C for the 600rpm/4ipm and 300rpm/4ipm run, respectively. The thermal profile in 600rpm/4ipm run is above the dissolution temperature whereas, in 300rpm/4ipm run, only finer precipitates would dissolve, allowing the presence of only stable η precipitate. Thus, existing post-weld precipitates will have little to no effect on the final microstructure. The microstructure model shows a similar trend in agreement with the DSC and TEM imaging. The availability of more solute in the matrix was observed in the 600rpm/4ipm weld than in the 300rpm/4ipm run, thus affecting the mechanical properties of as-weld material compared to BM. This solute availability plays a significant role in the PWHT process. Substantial improvements in the strength displayed by the weld were due to the formation of strengthening precipitates when they were aged at 121°C for 24 hours. Solute available in matrix allowed the formation of

strengthening precipitates in larger amounts, resulting in obstruction of dislocation motion and, therefore, improving the strength of the weld. The experimental results validate the data generated via Super-predictor.

6.6   Conclusion

An interactive interface using a science-driven approach between the welding process and microstructural models was developed to predict the weld properties to increase productivity and reduce the trial-error approach for Al alloys. Validation of the model was obtained through detailed experiments. Peak temperature in nugget during FSW was a function of welding parameters as heat generation during FSW is depends on the yield stress (flow stress) of the workpiece. Higher rotational rate generates higher peak temperature, thus affecting the microstructure by the dissolution of precipitates and finer grain size. Variation in thermal profile due to different welding parameters causes microstructural changes in the nugget. Higher the peak temperature, higher the dissolution of strengthening precipitates in nugget, and lower the dislocation interaction with the precipitates, thus deterioration in the strength of weld compared to BM. Also, higher peak temperature causes more solute availability in the matrix as solid solution, allowing nucleation of new strengthening precipitates when subjected to PWHT, leading to improved weld strength compared to BM.

6.7   References

[1]   Y. Liu, C. Deng, B. Gong, Y. Bai, Effects of heterogeneity and coarse secondary phases on mechanical properties of 7050-T7451 aluminum alloy friction stir welding joint, Mater. Sci. Eng. A. 764 (2019).

[2]   Wayne M. Thomas, E.D. Nicholas, J.C. Needham, M.G. Murch, P. Temple-Smith, C.J. Dawes, Friction welding, 1995.

[3] M.W. Mahoney, C.G. Rhodes, J.G. Flintoff, R.A. Spurling, W.H. Bingel, Properties of friction-stir-welded 7075 T651 aluminum, Metall. Mater. Trans. A 1998 297. 29 (1998) 1955–1964.

[4] S. Gupta, R.S. Haridas, P. Agrawal, R.S. Mishra, K.J. Doherty, Influence of welding parameters on mechanical, microstructure, and corrosion behavior of friction stir welded Al 7017 alloy, Mater. Sci. Eng. A. 846 (2022) 143303.

[5] R.S. Mishra, Z.Y. Ma, Friction stir welding and processing, Mater. Sci. Eng. R Reports. 50 (2005) 1–78.

[6] A.P. Reynolds, W. Tang, Z. Khandkar, J.A. Khan, K. Lindner, Relationships between weld parameters, hardness distribution and temperature history in alloy 7050 friction stir welds, Sci. Technol. Weld. Join. 10 (2013) 190–199.

[7] L.E. Murr, G. Liu, J.C. Mcclure, A TEM study of precipitation and related microstructures in friction-stir-welded 6061 aluminium, J. Mater. Sci. 33 (1998) 1243–1251.

[8] O.V. Flores, C. Kennedy, L.E. Murr, D. Brown, S. Pappu, B.M. Nowak, J.C. McClure, Microstructural issues in a friction-stir-welded aluminum alloy, Scr. Mater. 38 (1998) 703–708.

[9] C. Dawes, W. Thomas, Friction stir process welds aluminium alloys : The process produces low-distortion, high-quality, low-cost welds on aluminium, Weld. J. (1996).

[10] G. Liu, L.E. Murr, C.S. Niou, J.C. McClure, F.R. Vega, Microstructural aspects of the friction-stir welding of 6061-T6 aluminum, Scr. Mater. 37 (1997) 355–361.

[11] R. Nandan, G.G. Roy, T.J. Lienert, T. Debroy, Three-dimensional heat and material flow during friction stir welding of mild steel, Acta Mater. 55 (2007) 883–895.

[12] R.Y. Hwang, C.P. Chou, The study on microstructural and mechanical properties of weld heat affected zone of 7075-T651 aluminum alloy, Scr. Mater. 38 (1997) 215–221.

[13] P. Ulysse, Three-dimensional modeling of the friction stir-welding process, Int. J. Mach. Tools Manuf. 42 (2002) 1549–1557.

[14] R. Nandan, G.G. Roy, T. Debroy, Numerical simulation of three-dimensional heat transfer and plastic flow during friction stir welding, Metall. Mater. Trans. A. 37 (2006) 1247–1259.

[15] M.Z.H. Khandkar, J.A. Khan, A.P. Reynolds, Prediction of temperature distribution and thermal history during friction stir welding: Input torque based model, Sci. Technol. Weld. Join. 8 (2003) 165–174.

[16] O.T. Midling, Grong, A process model for friction welding of AlMgSi alloys and AlSiC metal matrix composites—II. Haz microstructure and strength evolution, Acta Metall. Mater. 42 (1994) 1611–1622.

[17] R. Wagner, R. Kampmann., Phase transformation in materials, Mater. Sci. Technol. 5 (1991).

[18] O.R. Myhr, Grong, Process modelling applied to 6082-T6 aluminium weldments—II. Applications of model, Acta Metall. Mater. 39 (1991) 2703–2708.

[19] A. Deschamps, Y. Brechet, Influence of predeformation and agEing of an Al–Zn–Mg alloy—II. Modeling of precipitation kinetics and yield stress, Acta Mater. 47 (1998) 293–305.

[20] A. Deschamps, D. Dumont, Y. Bréchet, C. Sigli, B. Dubost, Process modeling of age-hardening aluminum alloys: from microstructure evolution to mechanical and fracture properties, (2001).

[21] M. Nicolas, A. Deschamps, Characterisation and modelling of precipitate evolution in an Al–Zn–Mg alloy during non-isothermal heat treatments, Acta Mater. 51 (2003) 6077–6094.

[22] N. Kamp, A. Sullivan, R. Tomasi, J.D. Robson, Modelling of heterogeneous precipitate distribution evolution during friction stir welding process, Acta Mater. 54 (2006) 2003–2014.

[23] N. Kamp, A. Sullivan, J.D. Robson, Modelling of friction stir welding of 7xxx aluminium alloys, Mater. Sci. Eng. A. 466 (2007) 246–255.

[24] N. Kamp, A.P. Reynolds, J.D. Robson, Modelling of 7050 aluminium alloy friction stir welding, Sci. Technol. Weld. Join. 14 (2013) 589–596.

[25] H.R. Shercliff, M.F. Ashby, A process model for age hardening of aluminium alloys—II. Applications of the model, Acta Metall. Mater. 38 (1990) 1803–1812.

[26] H.B. Schmidt, J.H. Hattel, Thermal modelling of friction stir welding, Scr. Mater. 58 (2008) 332–337.

[27] Y.J. Chao, X. Qi, W. Tang, Heat Transfer in Friction Stir Welding—Experimental and Numerical Studies, J. Manuf. Sci. Eng. 125 (2003) 138–145.

[28] D. Kashchiev, Nucleation - Basic theory with application, 2000.

[29] K.C. Russell, Nucleation in solids: The induction and steady state effects, Adv. Colloid Interface Sci. 13 (1980) 205–318.

[30] Q. Chen, J. Jeppsson, J. Ågren, Analytical treatment of diffusion during precipitate growth in multicomponent systems, Acta Mater. 56 (2008) 1890–1896.

[31] P.S. De, R.S. Mishra, Friction stir welding of precipitation strengthened aluminium alloys: scope and challenges, Sci. Technol. Weld. Join. 16 (2013) 343–347.

[32]   E.O. Hall, The Deformation and Ageing of Mild Steel: III Discussion of Results, Proc. Phys. Soc. Sect. B. 64 (1951) 747.

[33]   N.J. Petch, The orientation relationships between cementite and α-iron, Acta Cryst. 6 (1953) 96–96.

[34]   H.R. Shercliff, M.F. Ashby, A process model for age hardening of aluminium alloys—I. The model, Acta Metall. Mater. 38 (1990) 1789–1802.

[35]   M.F. Ashby, The deformation of plastically non-homogeneous materials, A J. Theor. Exp. Appl. Physcis. 21 (2006) 399–424.

[36]   S.C. Wang, Z. Zhu, M.J. Starink, Estimation of dislocation densities in cold rolled Al-Mg-Cu-Mn alloys by combination of yield strength data, EBSD and strength models, J. Microsc. 217 (2005) 174–178.

[37]   T. Ungár, A. Borbély, The effect of dislocation contrast on x-ray line broadening: A new approach to line profile analysis, Appl. Phys. Lett. 69 (1998) 3173.

[38]   A.J. Kulkarni, K. Krishnamurthy, S.P. Deshmukh, R.S. Mishra, Effect of particle size distribution on strength of precipitation-hardened alloys, J. Mater. Res. 19 (2004) 2765–2773.

[39]   X.M. Li, M.J. Starink, Effect of compositional variations on characteristics of coarse intermetallic particles in overaged 7000 aluminium alloys, Mater. Sci. Technol. 17 (2013) 1324–1328.

[40]   X.M. Li, M.J. Starink, DSC study on phase transitions and their correlation with properties of overaged Al-Zn-Mg-Cu alloys, J. Mater. Eng. Perform. 21 (2012) 977–984.

[41]   T. Ogura, S. Hirosawa, T. Sato, Quantitative characterization of precipitate free zones in Al-Zn-Mg(-Ag) alloys by microchemical analysis and nanoindentation measurement, Sci. Technol. Adv. Mater. 5 (2004) 491–496.

[42]   Frigaard, Grong, O.T. Midling, A process model for friction stir welding of age hardening aluminum alloys, Metall. Mater. Trans. A. 32 (2001) 1189–1200.

[32]   Q. Chen, J. Jeppsson, J. Ågren, Analytical treatment of diffusion during precipitate growth in multicomponent systems, Acta Mater. 56 (2008) 1890–1896.

[33]   P.S. De, R.S. Mishra, Friction stir welding of precipitation strengthened aluminium alloys: scope and challenges, Https://Doi.Org/10.1179/1362171811Y.0000000020. 16 (2013) 343–347.

[34]   E.O. Hall, The Deformation and Ageing of Mild Steel: III Discussion of Results, Proc. Phys. Soc. Sect. B. 64 (1951) 747.

[35] N.J. Petch, The orientation relationships between cementite and α-iron, Acta Cryst. 6 (1953) 96–96.

[36] H.R. Shercliff, M.F. Ashby, A process model for age hardening of aluminium alloys—I. The model, Acta Metall. Mater. 38 (1990) 1789–1802.

[37] M.F. Ashby, The deformation of plastically non-homogeneous materials, A J. Theor. Exp. Appl. Physcis. 21 (2006) 399–424.

[38] S.C. Wang, Z. Zhu, M.J. Starink, Estimation of dislocation densities in cold rolled Al-Mg-Cu-Mn alloys by combination of yield strength data, EBSD and strength models, J. Microsc. 217 (2005) 174–178.

[39] T. Ungár, A. Borbély, The effect of dislocation contrast on x-ray line broadening: A new approach to line profile analysis, Appl. Phys. Lett. 69 (1998) 3173.

[40] A.J. Kulkarni, K. Krishnamurthy, S.P. Deshmukh, R.S. Mishra, Effect of particle size distribution on strength of precipitation-hardened alloys, J. Mater. Res. 19 (2004) 2765–2773.

[41] X.M. Li, M.J. Starink, Effect of compositional variations on characteristics of coarse intermetallic particles in overaged 7000 aluminium alloys, Mater. Sci. Technol. 17 (2013) 1324–1328.

[42] X.M. Li, M.J. Starink, DSC study on phase transitions and their correlation with properties of overaged Al-Zn-Mg-Cu alloys, J. Mater. Eng. Perform. 21 (2012) 977–984.

[43] T. Ogura, S. Hirosawa, T. Sato, Quantitative characterization of precipitate free zones in Al-Zn-Mg(-Ag) alloys by microchemical analysis and nanoindentation measurement, Sci. Technol. Adv. Mater. 5 (2004) 491–496.

CHAPTER 7

CONCLUDING REMARKS AND FUTURE WORK

7.1   Concluding Remarks

Process parameters affect the mechanical properties of the material by altering the microstructure. HEAs derive their strength from phase transformation and grain refinement, whereas precipitation strengthened Al alloys from the precipitation evolution. Thus, the steep temperature gradient and high strain rate generated during the FSW allow tailoring of the microstructure for the desired weld property. Currently, the FSW is performed with the help of empirical knowledge or a trial & error approach, and to avoid these time-consuming, experiment-intensive, and expensive methods, a science-drive approach was developed. The model was based on a simple relationship between the process-microstructure-property. The computational modeling and experiments were designed to understand the effect of process parameters on the microstructural change, thus affecting the final weld property.

In the case of HEAs, high strength in the nugget and HAZ compared to the base material were observed. The process, i.e., FSW, caused the generation of high temperature and high strain rates, which led to microstructural changes - phase transformation and grain refinement, thus affecting the final weld properties.

In Al 2195, a numerical model using the Avrami equation for predicting the strength of the material post heat treatment. Adequate heat treatment may influence the formation of the strengthening precipitates, thus leading to material strengthening. The selection of appropriate process parameters is vital as precipitation strengthening alloys are temperature sensitive; it may lead the material to be over-aged or under-aged, thus affecting the outcome.

In the case of Al 7017, the effect of weld parameters was observed. However, the change

in any parameter like traverse speed causes a change in the thermal profile generated due to which the precipitation strengthened Al alloy significantly influences the final microstructure and weld properties. Also, the impact was observed on the width of the HAZ region. Faster welding speed leads to a lower peak temperature, and less time is spent at the same point, thus allowing less coarsening of precipitates in the HAZ region, resulting in a narrow HAZ region with a better mechanical property.

Super-predictor is a model developed to predict the properties of the weld, starting from the generation of the thermal profile during FSW to predicting the precipitation evolution to finally calculating the final weld properties. High peak temperatures were observed with high rotational speed during the weld, which caused precipitate dissolution, leading to a significant drop in strength compared to weld with lower rotational speed and the base material. Due to the dissolution, a high-volume fraction of solute was present in the matrix, allowing re-precipitation to occur when subjected to PWHT, thus improving the weld properties. The model illustrated that the weld properties depended on the process parameters that influenced and tailored the microstructure. The results from the model were validated via experiments.

7.2 Recommendations for Future Work

FSW is a promising joining technique for alloy systems. The predictive capabilities of computational modeling combined with experimental validations can go a long way in suggesting appropriate process parameters for desired weld properties based on their applications. The current model could help predict the properties of the dissimilar weld as the joining of dissimilar material has many challenges due to the difference in melting temperatures, yield strength, and thermal conductivity. Thus, the model can broaden the applicability of the FSW for more materials.